

Mantle Melting, Melt Transport, and Delivery Beneath a Slow-Spreading Ridge: The Paleo-MAR from 23°15'N to 23°45'N

HENRY J. B. DICK^{1*}, C. JOHAN LISSENBERG² AND JESSICA M. WARREN³

¹DEPARTMENT OF GEOLOGY AND GEOPHYSICS, WOODS HOLE OCEANOGRAPHIC INSTITUTION, WOODS HOLE, MA 02543, USA

²SCHOOL OF EARTH AND OCEAN SCIENCES, CARDIFF UNIVERSITY, CARDIFF CF10 3YE, UK

³DEPARTMENT OF TERRESTRIAL MAGNETISM, CARNEGIE INSTITUTION OF WASHINGTON, WASHINGTON, DC, 20015, USA

RECEIVED JANUARY 20, 2009; ACCEPTED NOVEMBER 24, 2009

Kane Megamullion, an oceanic core complex near the Mid-Atlantic Ridge (MAR) abutting the Kane Transform, exposes nearly the full plutonic foundation of the MARK paleo-ridge segment. This provides the first opportunity for a detailed look at the patterns of mantle melting, melt transport and delivery at a slow-spreading ridge. The Kane lower crust and mantle section is heterogeneous, as a result of focused mantle melt flow to different points beneath the ridge segment in time and space, over an ~300–400 kyr time scale. The association of residual mantle peridotite, dunite and troctolite with a large ~1km+ thick gabbro section at the Adam Dome Magmatic Center in the southern third of the complex probably represents the crust–mantle transition. This provides direct evidence for local melt accumulation in the shallow mantle near the base of the crust as a result of dilation accompanying corner flow beneath the ridge. Dunite and troctolite with high-Mg Cpx represent melt–rock reaction with the mantle, and suggest that this should be taken into account in modeling the evolution of mid-ocean ridge basalt (MORB). Despite early precipitation of high-Mg Cpx, wehrlites similar to those in many ophiolites were not found. Peridotite modes from the main core complex and transform wall define a depletion trend coincident with that for the SW Indian Ridge projecting toward East Pacific Rise mantle exposed at Hess Deep. The average Kane transform peridotite is a lherzolite with 5.2% Cpx, whereas that from the main core complex is a harzburgite with only 3.5%

Cpx. As the area corresponds to a regional bathymetric low, and the crust is apparently thin, it is likely that most residual mantle along the MAR is significantly more depleted. Thus, harzburgitic and lherzolitic ophiolite subtypes cannot be simply interpreted as slow- and fast-spreading ridges respectively. The mantle peridotites are consistent with a transform edge effect caused by juxtaposition of old cold lithosphere against upwelling mantle at the ridge–transform intersection. This effect is far more local, confined to within 10 km of the transform slip zone, and far smaller than previously thought, corresponding to ~8% as opposed to 12.5% melting of a pyrolytic mantle away from the transform. Excluding the transform, the overall degree of melting over 3 Myr indicated by the peridotites is uniform, ranging from ~11.3 to 13.8%. Large variations in composition for a single dredge or ROV dive, however, reflect local melt transport through the shallow mantle. This produced variable extents of melt–rock reaction, dunite formation, and melt impregnation. At least three styles of late mantle metasomatism are present. Small amounts of plagioclase with elevated sodium and titanium and alumina-depletion in pyroxene relative to residual spinel peridotites represent impregnation by a MORB-like melt. Highly variable alumina depletion in pyroxene rims in spinel peridotite probably represents cryptic metasomatism by small volumes of late transient silica-rich melts meandering through the shallow mantle. Direct evidence for such melts is seen in orthopyroxene veins. Finally, a late

*Corresponding author. Telephone: 508-289-2590. E-mail: hdick@whoi.edu

hydrous fluid may be required to explain anomalous pyroxene sodium enrichment in spinel peridotites. The discontinuous thin lower crust exposed at Kane Megamullion contrasts with the >700 km² 1.5 km+ thick Atlantis Bank gabbro massif at the SW Indian Ridge (SWIR), clearly showing more robust magmatism at the latter. However, the SWIR spreading rate is 54% of the MAR rate, the offset of the Atlantis II Fracture Zone is 46% greater and Na₈ of the spatially associated basalts 16% greater—all of which predict precisely the opposite. At the same time, the average compositions of Kane and Atlantis II transform peridotites are nearly identical. This is best explained by a more fertile parent mantle beneath the SWIR and demonstrates that crustal thickness predicted by simply inverting MORB compositions can be significantly in error.

KEY WORDS: *peridotite; mantle; mineral chemistry; oceanic lithosphere; partial melting*

INTRODUCTION

We present the results of a detailed study of the mineralogy and petrology of peridotites, dunites, troctolites and veins representing systematic sampling of the shallow mantle and crust beneath a single slow-spreading magmatic ridge segment. This gives the first detailed picture of the pattern of sub-axial mantle melting, melt transport, and melt delivery beneath a ridge. These rocks are exposed at the Kane Megamullion, a large ~760 km² oceanic core complex in the rift mountains of the Mid-Atlantic Ridge (MAR) south of the Kane Fracture Zone (FZ). This complex was extensively dredged and sampled by ROV during R.V. *Knorr* Cruise 180 Leg 2 in 2004 (Dick *et al.*, 2008), and the transform wall bounding it to the north was systematically sampled by the submersible *Nautilus* on the 1992 Kanaut expedition (Auzende *et al.*, 1993, 1994). Data for the transform wall are largely from Ghose *et al.* (1996) and Ghose (1997), whereas we present new data for the main core complex to the south.

We show that the mantle underwent a relatively constant overall moderate degree of melting both in time and space at the ridge segment scale. Local variability at the outcrop scale is often large, but reflects melt–rock reaction, hybridization, and solution channeling to produce dunite during melt transport through the shallow mantle and crust–mantle transition. These effects are particularly apparent in an area of focused melt flow in the southern third of the paleo-ridge segment at ~3 Ma (Dick *et al.*, 2008). There, in addition to primitive interbedded olivine-gabbros and cumulate troctolites, a large suite of dunites, olivine-rich troctolites and mantle veins occur, equivalent to the crust–mantle transition zone seen in ophiolites. Adjacent to the Kane FZ, where the transform wall was extensively sampled by submersible (Auzende *et al.*, 1992, 1994), the mantle is relatively undepleted (Ghose *et al.*, 1996; Ghose, 1997). This provides evidence for

a transform edge effect, as previously proposed from a few widely spaced samples (Michael & Bonatti, 1985; Ghose *et al.*, 1996). Our data, however, show that despite the large Kane Transform offset (~150 km), the effect is limited to within 10 km of the plate boundary, and not over ~160 km as previously inferred. The mantle beneath the paleo-segment is depleted harzburgite not lherzolite, despite its position far from a hotspot along one of the deepest sections of the MAR. This suggests that most shallow mantle beneath slow-spreading ridge segments is highly depleted, as in the Pacific, casting into doubt the classification of ophiolites as representing fast- or slow-spreading crust on the basis of peridotite modal compositions. It also argues for similar extents of melting beneath slow and fast ridges, which helps explain the uniformity of mid-ocean ridge basalt (MORB) major element compositions, and why to a first order their trace element and isotopic compositions reflect that of the source, and not the melting process.

GEOLOGICAL AND TECTONIC SETTING

Plate tectonic setting

The Kane Megamullion formed by a long-lived detachment fault that unroofed gabbro and serpentized mantle peridotite at the western wall of the MAR rift valley at its eastern intersection with the Kane Fracture Zone. The complex lies between 23°15'N and 23°45'N, and 45°13'W to 45°26'W, 30–35 km west of the modern rift valley (Fig. 1). It represents accretion of lower crust and mantle from ~3.3 to 2.1 Ma (Williams, 2007). The complex extends ~40 km south of the fracture zone to the ~23°15'N non-transform axial discontinuity. This discontinuity represents the paleo and modern spreading segment end and is marked by a bathymetric depression and the occurrence of serpentized peridotite with pillow basalt on the rift valley wall, rather than gabbros and diabase as found to the north (Mével *et al.*, 1991). The segment north of the discontinuity (MARK area or Mid-Atlantic Ridge Kane) corresponds to the Kane Megamullion paleo-ridge. It has apparently normal seismic structure with slightly thin 4–5 km thick crust and attenuated gravity, whereas the segment to the south has crustal thickness of 6–7 km and more normal gravity (Purdy & Detrick, 1986; Morris & Detrick, 1991). No seismic evidence exists for a currently active magma chamber (Detrick *et al.*, 1990). Like many core complexes, Kane Megamullion formed during strongly asymmetric spreading, 17.9 mm/year to the west and 7.9 mm/year to the east (Williams *et al.*, 2006).

Physiography

The Kane Megamullion is distinguished from the surrounding rough, ridge-parallel, lineated volcanic terrain

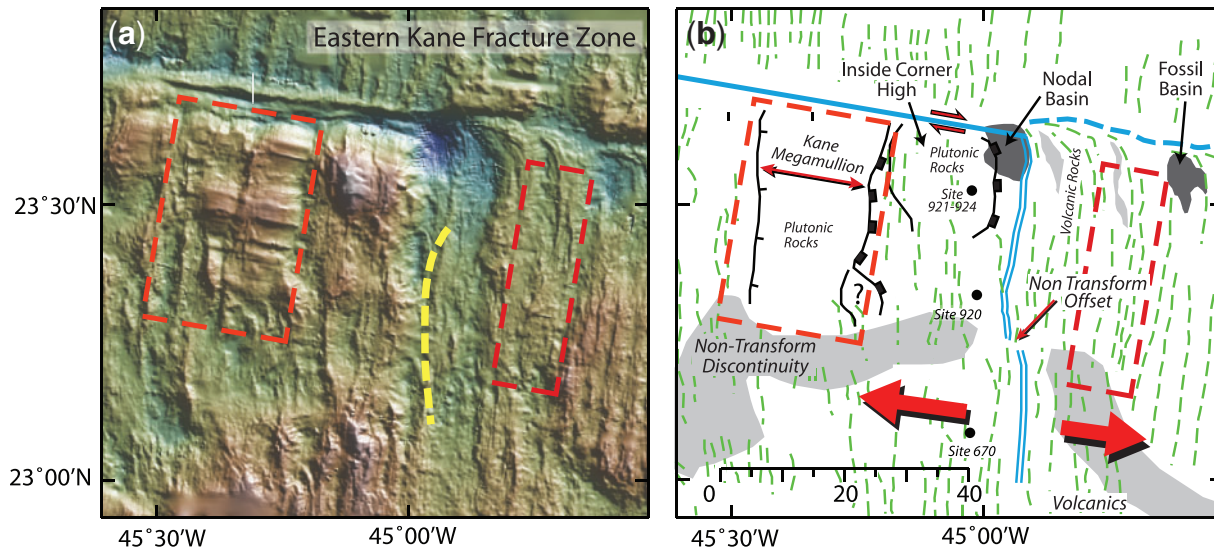


Fig. 1. (a) Shaded relief bathymetric map from GeoMapAp, showing the location of the Kane Megamullion and the eastern ridge–transform intersection of the Mid-Atlantic Ridge with the Kane Fracture Zone (MARK area). Yellow dashed line corresponds to the central magnetic anomaly area of the Kane Megamullion boxed in red on left side of the map with crust of the same age boxed on the right side. (b) Tectonic interpretation of the Kane Megamullion modified from Dick *et al.* (2008) and references therein. Green dashed lines are ridge-parallel volcanic lineaments, Heavy tabbed lines are detachment fault zone terminations, lightly tabbed lines are detachment breakaway zones. ●, ocean drilling sites. Active transform fault zone indicated by continuous blue line and its inactive trace by the dashed blue line. The ridge axis is indicated by a double blue line. Non-transform discontinuity trace is from Cannat *et al.* (1995).

by its relatively smooth surface and spreading-parallel corrugations or ‘mullions’ with amplitudes up to several hundred meters (Fig. 2). These features are typical of Atlantic and Indian Ocean core complexes (Tucholke *et al.*, 1998, 2008; Ohara *et al.*, 2001; Searle *et al.*, 2003; Okino *et al.*, 2004; Cannat *et al.*, 2006). The main core complex consists of a series of four smooth and two irregular domes or ‘turtlebacks’ (Fig. 2): Mt. Ararat and Babel Dome in the north, Abel and Cain Domes in central region, and Adam and Eve Domes to the south. These paired domes are separated by a long NNE–SSW high-angle normal fault that may have localized off-axis eruption of basalt, but exposes massive peridotite and gabbro beneath the detachment fault surface in the southern two-thirds of the complex (Fig. 2). The transform wall is the northern flank of the core complex, and where uneroded by landslips, the detachment surface is continuous, curving smoothly down to merge into the transform floor (see Dick *et al.*, 2008, Fig. 4). Lineations on the uneroded surface on the transform wall are horizontal, and it is evident that the detachment fault merges with the transform fault, representing a continuous curvilinear plate boundary. Thus, the rocks forming the core complex and the transform wall represent one body, produced by corner flow at the ridge–transform intersection. The transform wall then represents a fossil plate boundary, and not a simple cross-section of the ocean crust (Dick *et al.*, 2008). The primary stratigraphic relationships exposed on the transform wall represent lateral intrusion of gabbro into mantle peridotite emplaced

in the transform domain at the ridge–transform intersection (see Dick *et al.*, 2008, fig. 13b).

Map distribution of lithologies: a heterogeneous lower crust and mantle

The distribution of lithologies (diabase, gabbro and peridotite) over Kane Megamullion provides direct evidence for large-scale lateral heterogeneity of the lower crust and mantle beneath the paleo-ridge (Dick *et al.*, 2008). This is consistent with a large-offset (6 km) multichannel seismic experiment imaging the upper 0.5–1.7 km of the crust (Canales *et al.*, 2008). This heterogeneity appears to be caused by focused melt flow through the mantle to different points beneath the segment in time and space on a ~300–400 kyr time scale. This contrasts with previous models for focused melt flow principally toward the mid-point of a segment (e.g. Whitehead *et al.*, 1984; Kuo & Forsyth, 1988; Dick, 1989; Lin *et al.*, 1990), or intruded randomly beneath the ridge to create a sort of ‘plum-pudding’ mix of lower crust and mantle lithologies (e.g. Cannat, 1993; Tartarotti *et al.*, 1995a).

There are three principal lithological assemblages: (1) hanging-wall debris rafted onto the detachment surface; (2) a detachment fault zone assemblage; (3) basement rocks. Each of these is interpreted differently to reassemble the crustal architecture at the point of accretion. Only rocks from the headwalls of large landslips and high-angle normal faults cutting below the detachment surface are taken as unambiguously indicative of basement

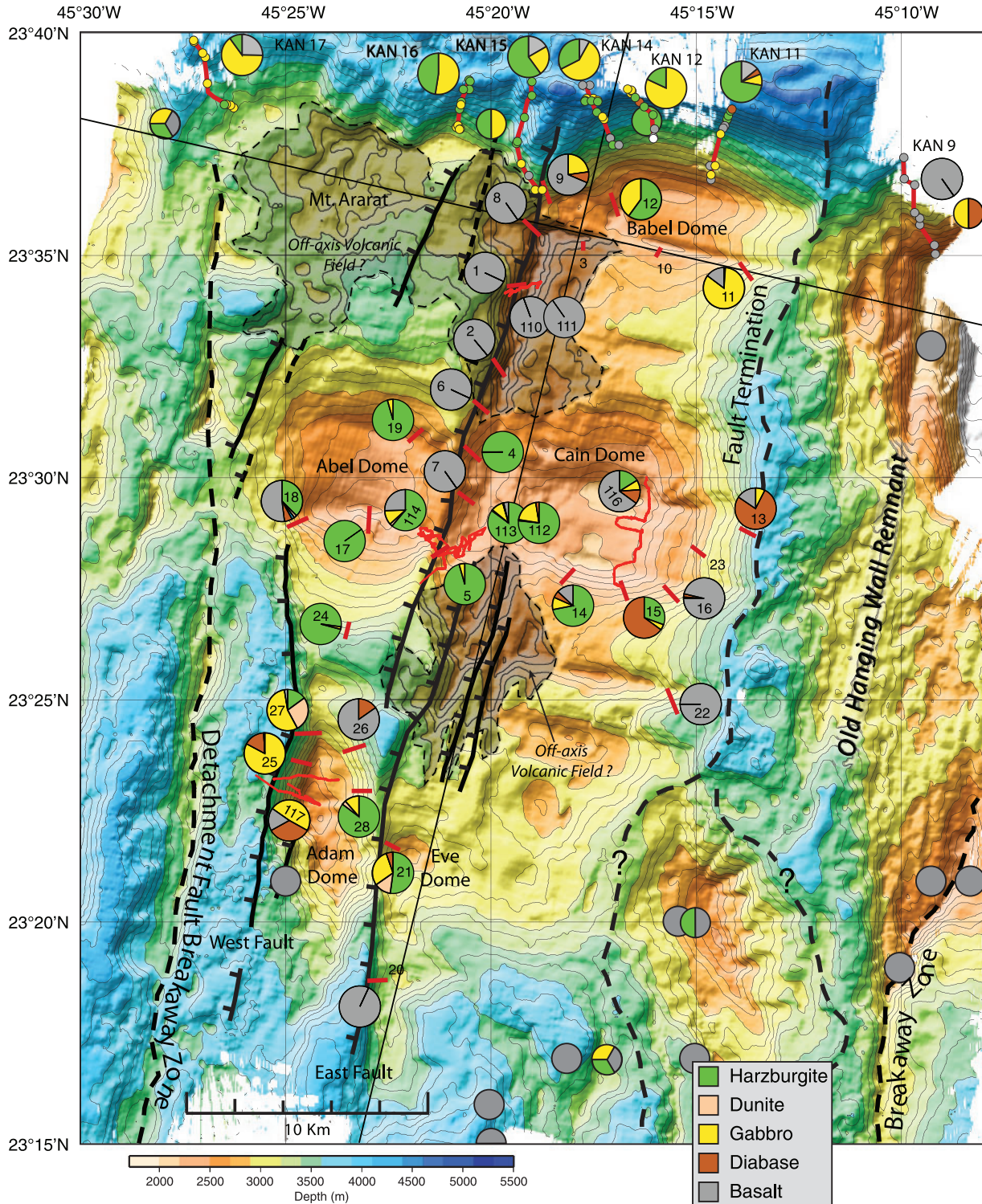


Fig. 2. Shaded-relief bathymetric map (illuminated from the SE) and simplified tectonic interpretation of the Kane Megamullion based on SeaBeam bathymetry from *Knorr* Cruise 180-2. Contour interval is 100 m. Larger pie diagrams show lithological proportions by weight in dredge and dive collections from the *Knorr* and *Kanaut* expeditions; smaller pie diagrams indicate lithologies reported in the literature where proportions are not available (I. Ghose, unpublished data, 1997). Tracks of *Jason II* dives 110–117 and *Nautille* dives KAN 9–17 are shown in red, as are dredge locations. Small colored circles show lithology at *Nautille* sample locations. Dredge, *Jason*, and *Nautille* dive numbers are labeled. Shaded regions indicate areas of possible off-axis volcanism. Modified from Dick *et al.* (2008).

stratigraphy. The detachment zone assemblage represents a mélange of footwall and hanging-wall rocks often in talc–tremolite–serpentine schist. This zone also localized intrusion of gabbroic veins and later diabase. The hanging-wall debris consists of: (1) weathered but otherwise unaltered and undeformed pillow basalt rubble; (2) diabase, commonly altered in the greenschist facies, scattered ubiquitously over the detachment surface. These rocks allow reconstruction of the hanging-wall stratigraphy in addition to that of the footwall. For example, even though dike rocks are largely absent in the basement assemblage in the central Cain and Abel region, abundant diabase dredged from the overlying detachment surface and sampled in the detachment fault zone testifies to a former dike complex, whereas the scarcity of gabbro in all three assemblages indicates the absence of a gabbroic layer (Dick *et al.*, 2008).

Except for late intrusive sills and dikes, the detachment zone assemblage generally shows significant deformation, with high-temperature granulite or upper amphibolite-facies crystal-plastic mylonite peridotite and gabbro overprinted by cataclastic deformation and extensive greenschist- or lower-temperature-facies alteration. Diabase has typically undergone cataclastic deformation, but little or no crystal-plastic deformation. Talc–serpentine schist is extensively exposed on the detachment fault surface, even over areas where the basement consists solely of gabbro or diabase, as has also been found at other core complexes (Dick *et al.*, 2001; Ildefonse *et al.*, 2007). Thus where these schists overlie massive gabbro, this probably represents talc and serpentine intrusion along the active detachment fault from adjacent areas where the fault cut hydrating mantle rocks.

Gabbros from the transform wall and dredged from Babel Dome are largely olivine gabbro and minor oxide gabbro. The associated peridotites from basement exposed in landlips are granular harzburgite and minor lherzolite (Ghose, 1997; Dick *et al.*, 2008). Ignoring ultramafic schists, the contact between gabbro and peridotites on the wall beneath Babel Dome appears deeper than beneath Mt. Ararat, probably representing a change from relatively weak to strong magmatic activity at around 2.8 Ma (Dick *et al.*, 2008).

In the central region, the basement assemblage consists of ~87% granular harzburgite and minor lherzolite, 1% dunite and 12% gabbro. The gabbros are generally highly altered, but where identifiable, 54% are oxide gabbro and 46% are olivine gabbro. The large majority are clearly intrusive veins. The hanging-wall assemblage contains abundant pillow basalt and diabase, but little gabbro.

In the southern region, ~11% of the basement rocks are dunite, 18% harzburgite and 19% diabase, and over half are gabbro. At Adam Dome inliers of the dike–gabbro transition and the crust–mantle transition are found on

West Fault, exposing a basement plutonic sequence for more than 1 km below the detachment fault.

Thus at the time represented by the position of East Fault (~3 Ma), there were magmatic centers in the north and south respectively, with a large intervening section in the center of the segment where the crust consisted of pillow lavas and sheeted dikes directly overlying the mantle intruded by minor gabbro (Dick *et al.*, 2008). In this central region there is little evidence for shallow mantle melt transport in the form of dunites or primitive troctolite. To the south, around Adam and Eve Domes, the abundant dunite associated with mantle harzburgite, primitive troctolite and olivine gabbro all show that large amounts of primitive melt were transported through the shallow mantle and delivered to the crust there. The Canales *et al.* (2008) seismic data suggest that the eastern portion of Cain Dome is underlain by a large gabbro body, as a result of either expansion of the Babel Dome magmatic center to the south or formation of an entirely new center. Their data further suggest that the irregular terrain east of Adam Dome represents a transition to weak magmatism and mixed gabbro–peridotite basement, even as magmatism was resurgent beneath Cain Dome to the north consistent with dredge results at Eve Dome.

PETROGRAPHY

Methods

One hundred and twenty-five peridotites, veins and associated dunites, troctolites and olivine gabbros were selected for petrographic analysis. Of these, 99 samples representing 121 lithologies had sufficient relict primary mineral for further analysis. These included 56 spinel harzburgites, 14 plagioclase harzburgites, four spinel lherzolites and three plagioclase lherzolites. Fifteen peridotites had late igneous veins, ranging from troctolite to oxide gabbro with inverted pigeonite, and four had early mantle veins, including an olivine websterite, two orthopyroxenites and spinel–olivine gabbro. In addition, there are 16 dunites, and four troctolites and troctolitic gabbros. Peridotite textural analysis is limited to pyroxene and spinel because of intense olivine alteration, which is preserved in only 27 of the samples and 12 of the 27 analyzed by Ghose (1997). Thirty-one peridotites were point counted on 21 × 31 thin sections at 1 mm point spacing (Table 1). Throughout this study, we compare our data with those for 17 Atlantic and Indian Ocean transforms. Some of these data are unpublished, but the majority were presented by Dick (1989).

Mantle lithologies

Shown in Fig. 3 are proportions of ultramafic rocks described by us in thin section and by Ghose (1997) compared with those point counted for the Atlantic and Indian Ocean transforms (Dick *et al.*, 1984). At transforms

Table 1: *Peridotite modal analyses*

Sample	Lat. (N)	Long. (W)	Lithology	OI	Opx	Cpx	Sp	Pl	Points	Notes
<i>Knorr Cruise 180 Leg 2, Main Core Complex</i>										
2-5-1	23-471	45-358	Harzburgite	83.8	14.4	1.1	0.7	0.0	2511	
2-5-2	23-471	45-358	Harzburgite	84.0	13.3	2.1	0.5	0.0	2420	
2-5-3	23-471	45-358	Lherzolite	80.7	11.1	7.9	0.2	0.0	2407	
2-5-9a	23-471	45-358	Lherzolite	64.4	30.4	4.3	0.8	0.0	2031	Contact with dunite
2-5-29	23-471	45-358	Harzburgite	78.3	21.0	0.3	0.3	0.1	2266	
2-12-5	23-607	45-286	Harzburgite	77.7	16.7	4.8	0.8	0.0	2367	
2-12-6	23-607	45-286	PI harzburgite	76.8	14.3	7.9	0.2	0.8	2518	
2-14-28	23-461	45-306	Harzburgite	76.1	19.2	4.6	0.1	0.0	2483	
2-14-37	23-461	45-306	Harzburgite	80.8	13.9	4.8	0.6	0.0	2714	
2-14-66	23-461	45-306	Harzburgite	78.6	18.8	2.0	0.6	0.0	2363	Metagabbro vein?
2-15-26	23-455	45-279	Harzburgite	81.7	16.7	1.1	0.4	0.0	2060	
2-17-17	23-480	45-384	Harzburgite	73.0	23.7	3.0	0.4	0.0	2445	
2-18-36	23-482	45-417	Harzburgite	73.6	21.6	4.5	0.3	0.0	1457	
2-19-20	23-519	45-362	Harzburgite	70.5	23.6	5.5	0.5	0.0	2420	
2-21-1	23-364	45-377	Harzburgite	71.2	25.5	2.9	0.4	0.0	2483	Gabbro vein
2-21-4	23-364	45-377	Harzburgite	75.9	21.5	2.3	0.3	0.0	2378	
2-21-8	23-364	45-377	Harzburgite	83.2	14.0	2.4	0.4	0.0	2564	Oxide gabbro vein
2-21-9a	23-364	45-377	PI harzburgite	80.6	13.6	4.7	0.1	1.0	2545	Olivine gabbro vein
2-28-16	23-383	45-382	PI harzburgite	76.4	20.0	2.9	0.3	0.4	2450	Gabbro vein
2-28-17	23-383	45-382	PI lherzolite	74.8	13.5	8.0	0.9	2.9	2327	Gabbro vein
2-28-34	23-383	45-382	Harzburgite	75.1	22.0	2.2	0.7	0.0	2549	
Jas112-1	23-466	45-359	Harzburgite	77.6	18.1	4.0	0.3	0.0	2526	
Jas112-10	23-468	45-355	PI harzburgite	87.1	12.0	0.4	0.1	0.5	2179	2 mm prehnite vein
Jas112-38	23-472	45-356	Harzburgite	84.4	13.5	1.3	0.6	0.2	2720	
Jas112-44	23-474	45-354	Harzburgite	82.5	14.0	2.7	0.6	0.2	2566	Metagabbro vein
Jas112-63	23-473	45-350	Lherzolite	68.8	24.3	6.4	0.5	0.0	2460	
Jas112-71	23-474	45-350	Harzburgite	81.6	14.9	3.0	0.4	0.0	2526	
Jas112-84	23-477	45-348	Harzburgite	71.8	23.5	4.1	0.6	0.0	2440	
Jas112-116	23-471	45-350	PI harzburgite	73.8	21.5	3.9	0.6	0.2	2420	
Jas113-2	23-471	45-359	Harzburgite	81.8	17.1	0.6	0.5	0.0	1781	Gabbro vein
Jas113-40	23-476	45-360	Harzburgite	82.8	14.2	2.7	0.4	0.0	2252	
			Average	77.7	18.1	3.5	0.5	0.2	2375	
<i>Kanaut Expedition transform wall peridotites from Ghose (1997)</i>										
D2-2-2	23-633	45-332	Harzburgite	61.8	32.8	4.7	0.7	—	—	
D2-3-6	23-633	45-332	Harzburgite	78.4	17.0	4.7	0.9	—	—	
Kan-3-1	23-627	44-962	Harzburgite	77.5	21.1	1.1	0.3	—	—	
Kan-14-6	23-641	45-293	Harzburgite	74.1	22.1	3.7	0.2	—	—	
Kan-15-6	23-625	45-324	Harzburgite	69.4	25.6	4.5	0.5	—	—	
Kan-16-1	23-648	45-343	Harzburgite	71.0	24.2	3.9	0.9	—	—	
D1-1B-1	23-625	45-267	Lherzolite	69.6	24.0	5.0	1.3	—	—	
Kan-14-8	23-640	45-294	Lherzolite	76.9	16.4	6.0	0.8	—	—	
Kan-15-3	23-641	45-319	Lherzolite	76.7	16.1	6.3	0.9	—	—	
Kan-19-2	23-742	45-592	Lherzolite	69.0	18.4	11.7	0.9	—	—	
			Average	72.4	21.8	5.2	0.7			

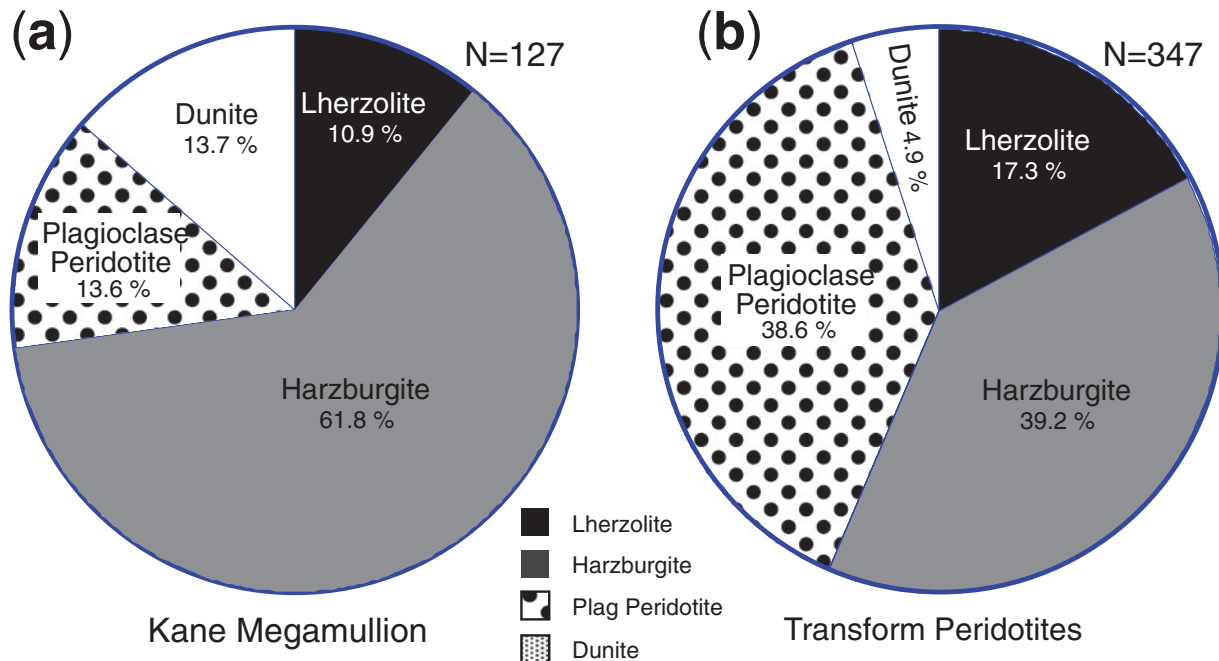


Fig. 3. Pie diagram showing the proportions of peridotites studied in thin section from (a) the Kane Megamullion, and (b) 17 Indian and Atlantic Ocean transform faults (Dick, 1989). Dunites are over-represented in the Kane dataset, which was otherwise chosen to be representative of the entire sample suite.

plagioclase peridotite and harzburgite are the dominant lithologies, whereas dunite is the least abundant. Lherzolite is more abundant in the transform peridotites compared with the sub-axial mantle at the Kane Megamullion. In both groups, however, dunite was over-sampled for thin section study, although the other lithologies are proportionally representative of what was collected. The actual amount of dunite relative to peridotite in the Kane dredge samples is 4.6% by weight (10.6% by number), whereas the transform suites contain 2.3% by weight (Dick, 1989). No dunite has been reported from the transform wall flanking the Kane Megamullion. A scarcity of dunites is characteristic of transform faults, as also observed by Brunelli *et al.* (2006) for the Vema Fracture Zone, where dunite, as a fraction of the peridotites, constituted <1% of 33 peridotite dredge hauls.

Internal to the Kane Megamullion, the main core complex peridotites appear more depleted than those from the transform wall, with an average of 3.5 vol. % diopside (Fig. 4a), compared with an average of 5.8 vol. % in the flanking transform wall peridotites (Ghose, 1997). The average Cpx content for the Atlantic and Indian Ocean transform suites, which include transforms near mantle hotspots, is 3.9 vol. % (Fig. 4b). Modal compositions for the main core complex define a rough trend in the pyroxene–olivine ternary similar to SW Indian Ridge (SWIR) peridotites (Fig. 4c), consistent with the residues of variable degrees of partial melting (e.g. Dick *et al.*, 1984). When

averaged by dive or dredge, this trend is accentuated, and lies along that for the SWIR (Fig. 4d) at the low-Cpx end corresponding to relatively high degrees of mantle melting.

Spinel harzburgite and lherzolite

Plagioclase-free spinel harzburgites and lherzolites are typical abyssal peridotites, generally heavily serpentinized with subsequent argillation of relict olivine as a result of seafloor weathering. Hydrothermal alteration is unusually intense, with many samples partially or completely altered to talc–serpentine or talc–tremolite schist. Significant chlorite-, tremolite-, talc-, or amphibole-bearing veins occur in 19 samples; however, the majority contain at least some talc and tremolite, and more rarely aluminous amphibole. Texturally, the population is bimodal (Figs 5–7), with the larger proportion of our samples showing relatively intense crystal-plastic deformation, grading to porphyroclastic 2 or higher with a peak at deformation grade 3 (protomylonite), often completely obscuring earlier weak porphyroclastic or ‘protogranular’ mantle fabrics. The second peak at 0.5 (protogranular) largely represents granular peridotites from landslip headwalls and faults cutting several hundred meters beneath the detachment surface. The overall intense hydrothermal alteration, cataclasis, and crystal-plastic deformation reflect proximity to the detachment fault surface. Deformation initially localized in fresh peridotite, forming mylonites similar to those reported by Jaroslow *et al.* (1996), suggesting that

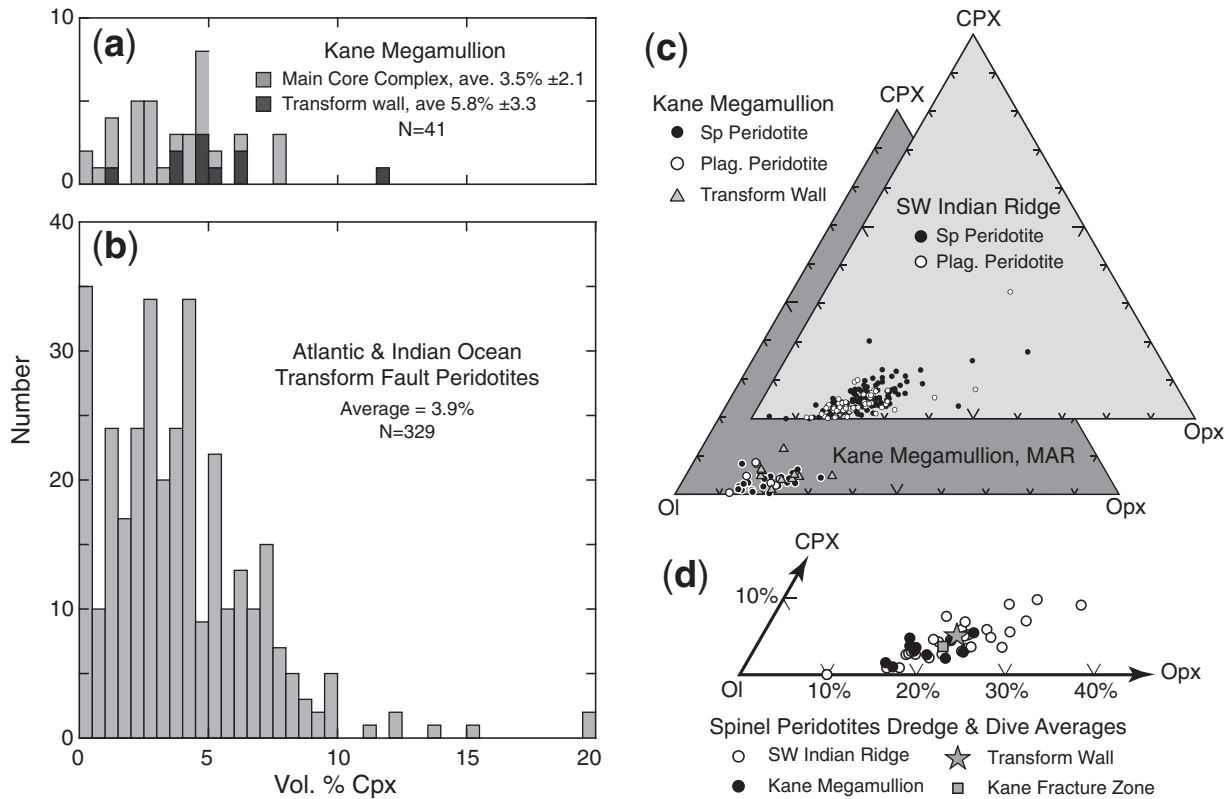


Fig. 4. Volume per cent modal pyroxene in (a) Kane Megamullion peridotites and (b) 17 Atlantic and Indian Ocean transform fault peridotite suites. (c) Mineral modes for SWIR transform peridotites from Dick *et al.* (1989) and for Kane Megamullion peridotites (this study). (d) Kane Megamullion and SWIR mineral modes averaged by dredge or dive. ‘Transform wall’ represents the average mode of peridotites from the flank of the Kane Megamullion from Ghose (1997), and the Kane Fracture Zone average includes 21 additional analyses of older samples.

strain localization began at >600°C and then continued down through greenschist-facies brittle alteration to ambient seafloor temperatures.

Protogranular harzburgites and lherzolites are similar to those in many ophiolites (Fig. 6), with an average pyroxene grain size of ~4 mm. Pyroxene is characterized by smooth deeply embayed grain boundaries and often complex geometries (Fig. 6a–c), in contrast to the generally equant, rounded, and often kinked or stretched pyroxene in porphyroclastic peridotites (Fig. 6d–f). The term ‘protogranular’ originally referred to peridotite xenoliths that had escaped deformation since the olivine–spinel transition. This is unrealistic for mantle emplaced at a ridge, and these textures probably reflect static equilibration at the end of mantle upwelling (e.g. Ceuleneer & Cannat, 1997). Clinopyroxene, enstatite, and spinel are not always randomly distributed, but frequently occur in clusters (Fig. 6f), suggesting breakdown of a higher temperature pyroxene with excess spinel produced by incongruent melting of the pyroxene (e.g. Dickey, 1976). Chromian spinel is generally holly-leaf textured (Fig. 6g), although vermiform and euhedral to subhedral spinel is found in a few samples. In some cases, lineated spinel trains occur that probably

crystallized from migrating melt (Fig. 6h). Although protogranular and porphyroclastic textures are often treated as successive, in many of our samples textural elements of either appear to overprint the other. Thus, we associate protogranular texture with textural modification as a result of reaction with melt, whereas porphyroclastic textures appear to reflect dislocation creep at relatively high strain rates.

The more deformed samples range from well-foliated porphyroclastic (grade 2) to ultramyylonite (grade 5). These samples are characterized by rolled pyroxene augen (Fig. 7a), often intensely kinked, or elongate stretched grains defining a foliation (Fig. 7b) and ribbon structured olivine in the protomylonites (Fig. 7c). With increasing intensity of deformation, there is sharp decrease in grain size as a result of dynamic recrystallization (Fig. 7d). Protomylonitic textures may preserve some elements of protogranular texture, whereas these disappear in the foliated mylonites, with only rolled or stretched pyroxenes present in a fine-grained mass of recrystallized olivine (Fig. 7e). In ultramyylonites (Fig. 7f), most pyroxene augen have disappeared and the rock may appear unfoliated in hand sample despite the intense deformation.

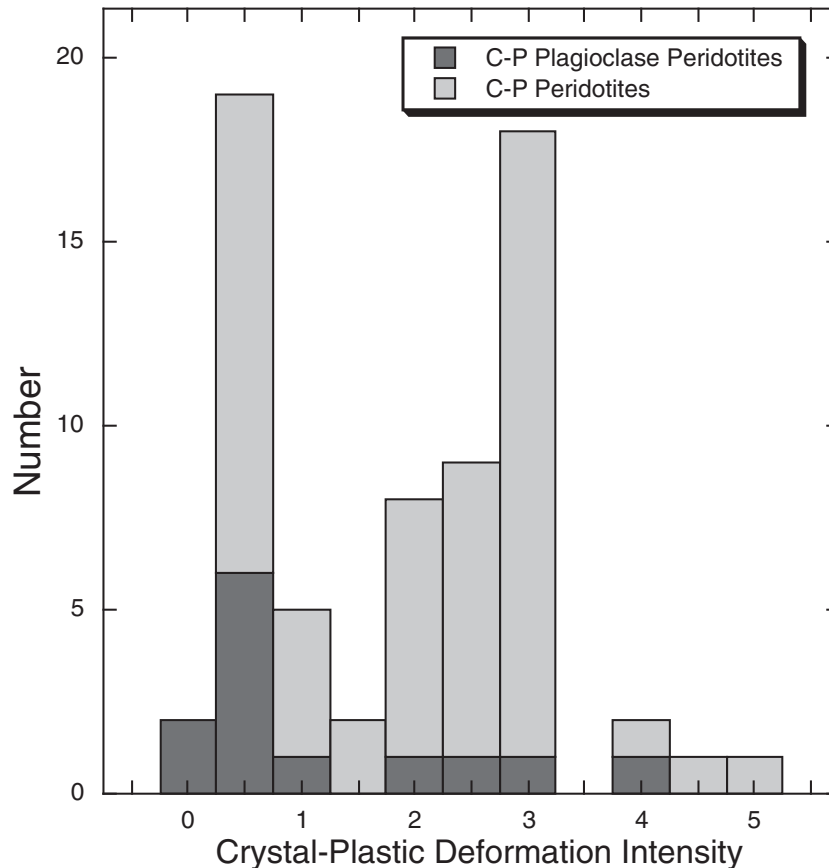


Fig. 5. Crystal-plastic deformation intensities plotted for spinel and plagioclase peridotites from the Kane Megamullion based on shipboard sample descriptions. Scale is an arbitrary classification: 0, undeformed protogranular; 1, porphyroclastic, no foliation; 2, porphyroclastic, clear foliation; 3, protomylonite; 4, mylonites; 5, ultramylonite.

Curiously, spinel in some mylonites appears to be concentrated in pressure shadows around pyroxene augen, or may even be euhedral (Fig. 7a at upper right of large Opx augen). Crystal-plastic deformation appears to have continued down from high temperatures until the appearance of massive talc (Fig. 7g).

Thirteen of 104 dredges from 17 Atlantic and Indian Ocean transforms have similar mylonite peridotites, while around 5% of all abyssal peridotites are mylonites (Dick, 1989). Where recovered, mylonite generally constitutes nearly all the peridotites in a dredge (Dick, 1989), suggesting that thick shear zones (tens of meters) are common on transform walls. Brunelli *et al.* (2006) similarly reported peridotite mylonites in five of 33 Vema Transform dredges, constituting more than 80% of the peridotite in four samples. Massive peridotite mylonites crop out at St. Paul's Rocks at the crest of a transverse ridge flanking the St. Paul's FZ on the MAR. The mylonites are oriented perpendicular to the ridge, but dip 60–70°E across the 150 m wide island (Melson *et al.*, 1972), representing a >65 m thick shear zone. Peridotite mylonites are a fairly common

feature of transform walls, consistent with the occurrence of detachment fault surfaces there. The significantly reduced grain size of olivine in mylonites has been demonstrated to promote shear localization and their presence on transform walls suggests the importance of ductile deformation mechanisms for detachment faults (Warren & Hirth, 2006).

Plagioclase peridotites

Fourteen per cent of the Kane Megamullion peridotites contain accessory plagioclase (Fig. 3). Because of intense alteration, however, this is indicated largely by its characteristic prehnite–chlorite pseudomorphs. These can be difficult to recognize in highly altered samples, and are often found only because of the presence of high spinel TiO₂ (>0.15 wt %), a characteristic indicator of plagioclase-bearing peridotites (Dick & Bullen, 1984; Dick, 1989; Cannat *et al.*, 1990; Lagabrielle & Cannat, 1990; Seyler & Bonatti, 1997; Tartarotti *et al.*, 2002), leading to re-inspection of the thin section. These pseudomorphs are mineralogically and texturally distinct from serpentine

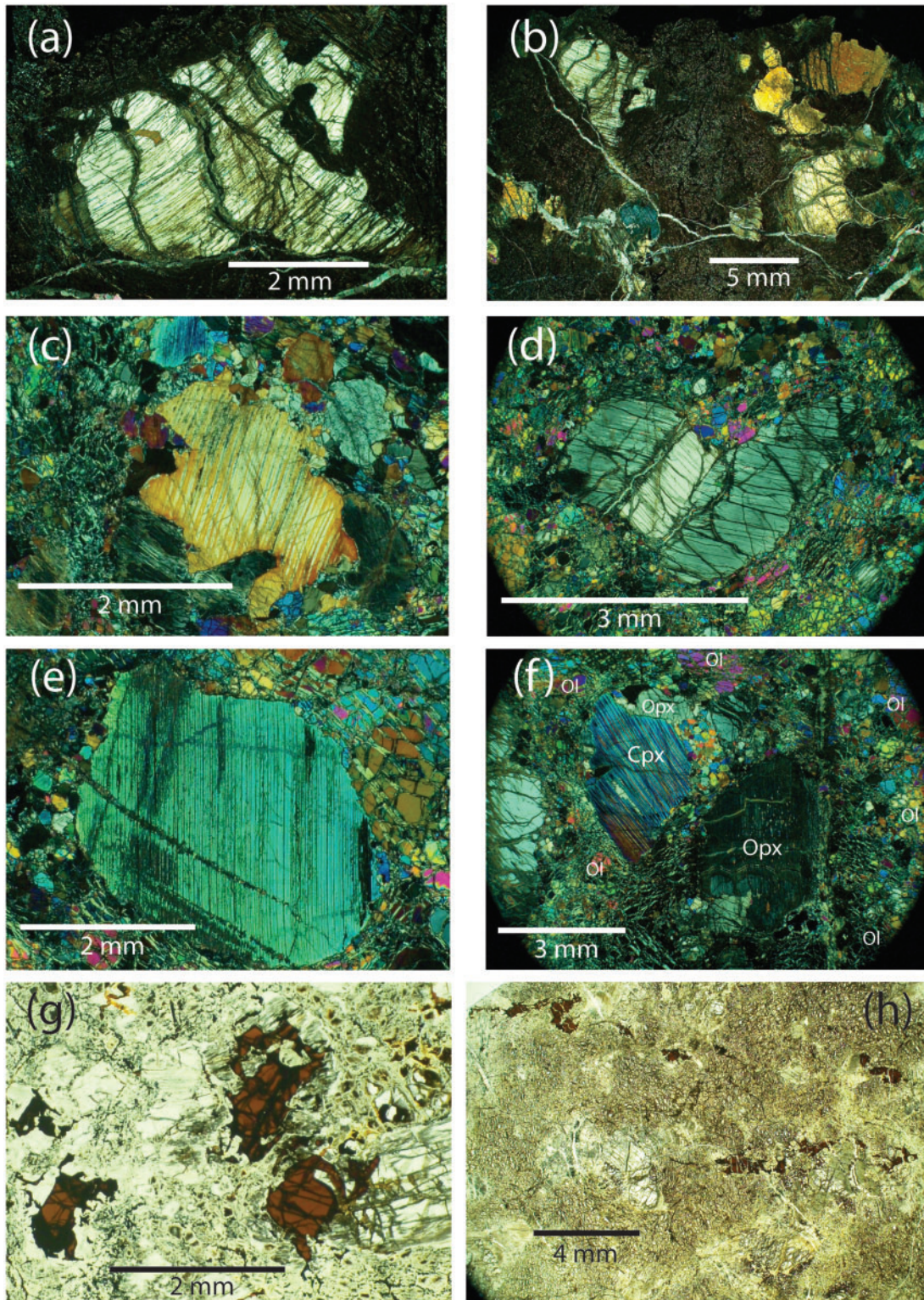


Fig. 6. Photomicrographs of Kane Megamullion peridotites exhibiting protogranular to porphyroclastic textures. (a) Kn180-2-18-36 protogranular enstatite. (b) Kn180-2-18-36 protogranular pyroxene texture in matrix of serpentinized and argillitized olivine. (c) Jas112-84 protogranular clinopyroxene preserved in porphyroclastic grade 1 peridotite. (d) Jas112-84 kinked enstatite porphyroclast in partially serpentinized olivine matrix. (e) Jas112-84 clinopyroxene augen in recrystallized olivine matrix in porphyroclastic peridotite. (f) Jas112-84 porphyroclastic clinopyroxene-orthopyroxene cluster with intervening pyroxene neoblasts in a partially serpentinized olivine matrix. (g) Jas112-63 holly-leaf spinel in serpentine matrix after olivine and orthopyroxene. (h) Kn180-2-5-9 holly-leaf spinel trails in partially serpentinized porphyroclastic peridotite.

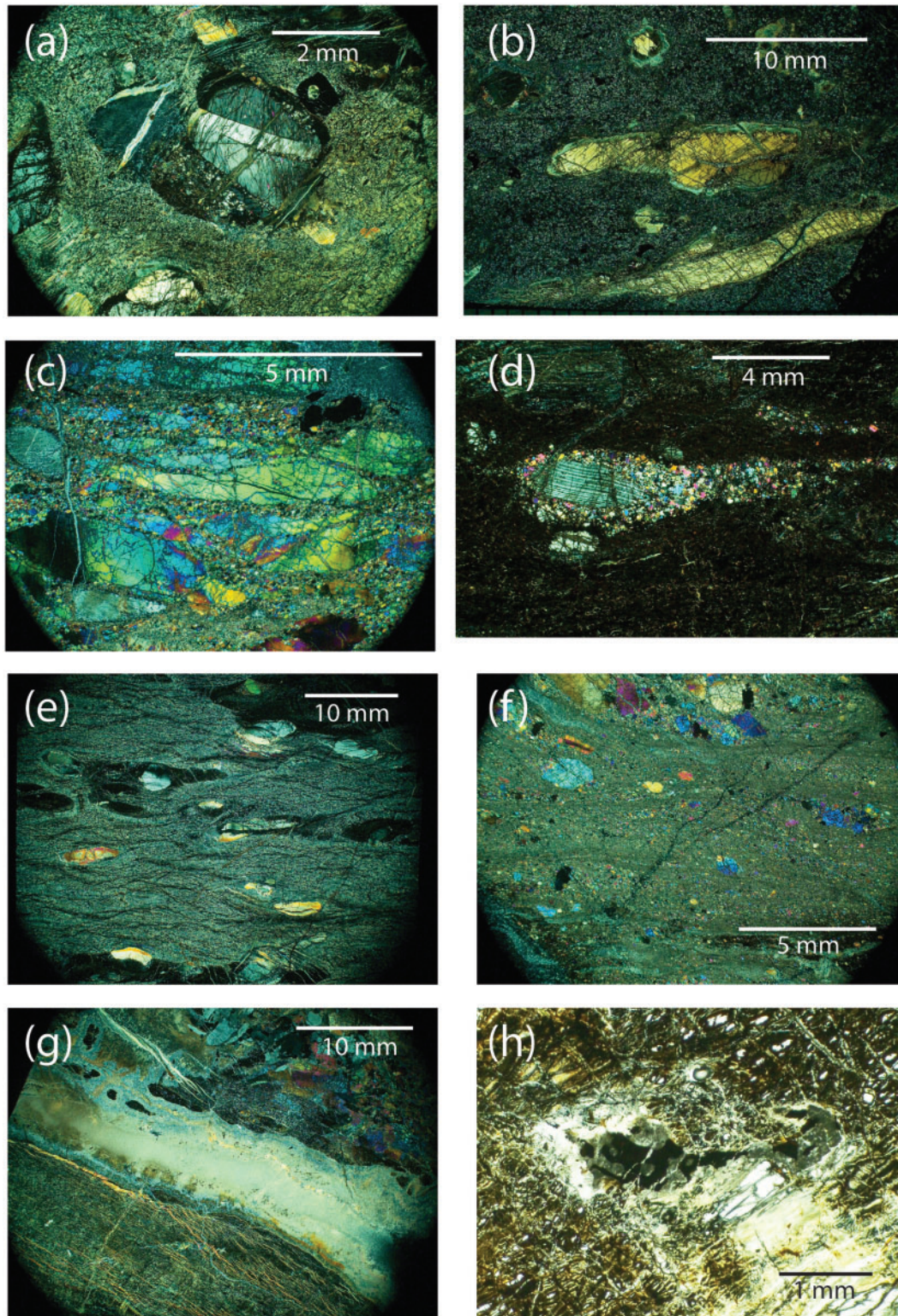


Fig. 7. Photomicrographs of protomylonite to ultramylonite Kane Megmullion peridotites. (a) Kn180-2-19-30 extreme kinking in an enstatite porphyroclast in a peridotite protomylonite. (Note euhedral spinel at upper right corner of the porphyroclast with a round silicate inclusion.) (b) Jas112-38 stretched enstatite augen in a grade 4 peridotite mylonites. (c) Kn180-2-17-18 ribbon structured olivine bands in a protomylonite. (d) Kn180-2-19-31 clinopyroxene augen rimmed by neoblasts in a matrix of partially serpentinized and argillitized olivine in a peridotite mylonite. (e) Kn180-2-17-9 partially serpentinized peridotite mylonite with relict pyroxene augen. (f) Jas113-12 ultramylonite zone in spinel peridotite. (g) Jas113-71 talc band separating 100% partially serpentinized and argillitized peridotite mylonite from grade 2 porphyroclastic peridotite with fresh relict olivine. (h) Kn180-2-28-16 plagioclase-spinel symplectite adjacent to partially pseudomorphed enstatite grain in an olivine matrix. Plagioclase is pseudomorphed by grey high-relief hydrogrossular of prehnite, whereas clear white mineral corona on left side of the symplectite is a mixture of serpentine, talc and tremolite.

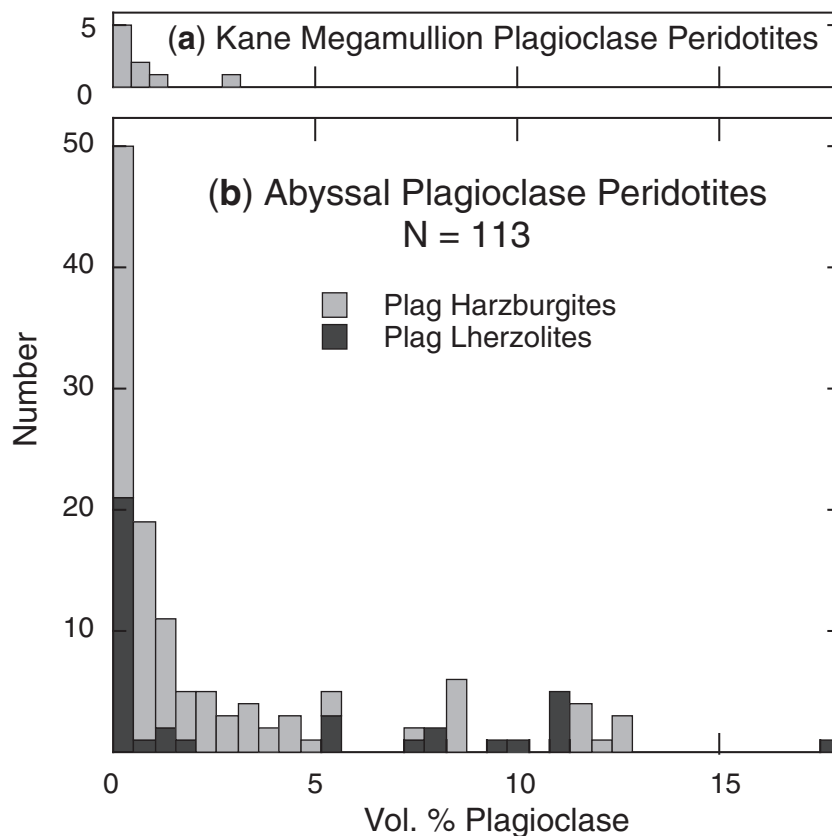


Fig. 8. Histogram of volume per cent modal plagioclase in (a) Kane Megamullion plagioclase peridotites and (b) abyssal plagioclase peridotites.

pseudomorphs of olivine and pyroxene. They have a unique interstitial or blebby appearance, and often form sub-triangular masses at olivine triple junctions, giving the distinct impression that plagioclase crystallized late from trapped or transient melt at shallow depth, generally post-high-temperature porphyroclastic deformation. Plagioclase is present only in small amounts, generally <1 vol. % (Fig. 8, Table 1), and occurs isolated in ground-mass olivine, but is commonly first recognized adjacent to pyroxene or as coronas around or as symplectitic intergrowths with spinel (e.g. Fig. 7h). Except for the plagioclase and anomalous Cpx abundance in a few samples (Fig. 4c), there is little that is different texturally from plagioclase-free spinel peridotites. Plagioclase peridotites appear in all three peridotite-bearing dredges from Adam and Eve Domes, but in only four of the remaining 14 peridotite-bearing dredges from the main core complex.

Mafic veins

Mafic veins are fairly abundant in the Kane Megamullion peridotites. Although many have relict minerals, they are often highly altered, consisting only of prehnite and chlorite after plagioclase, and talc, serpentine, chlorite or

amphibole after olivine and pyroxene. These veins are similar to others reported in abyssal peridotites (Constantin *et al.*, 1995; Tartarotti *et al.*, 1995b; Cannat *et al.*, 1997; Morishita *et al.*, 2004), most notably from near 23°N. They span the range of abyssal gabbro compositions from troctolite through olivine gabbro, gabbro, gabbro, pigeonitic oxide gabbro to oxide gabbro, lacking only trondhjemite. This sequence matches those at the major oceanic gabbro complexes drilled at Hole 735B at Atlantis Bank, Site 921, at the MARK inside-corner high, and Hole 1309D at the Atlantis Massif, consistent with a differentiation series crystallized from MORB. A single spinel-bearing olivine gabbro vein has mantle-like pyroxene compositions containing Cpx and Opx with Mg-number 91.9 and 90.7 respectively, and spinel with Cr-number of 48. It is similar to gabbro veins from Hess Deep, interpreted as representing MORB crystallized during high-temperature reaction with mantle wall-rocks (Dick & Natland, 1994). As in other abyssal peridotite studies, the gabbroic veins appear to have intruded largely after the ductile deformation associated with mantle upwelling. Locally they show evidence of crystal-plastic deformation and cataclasis, believed to be associated with

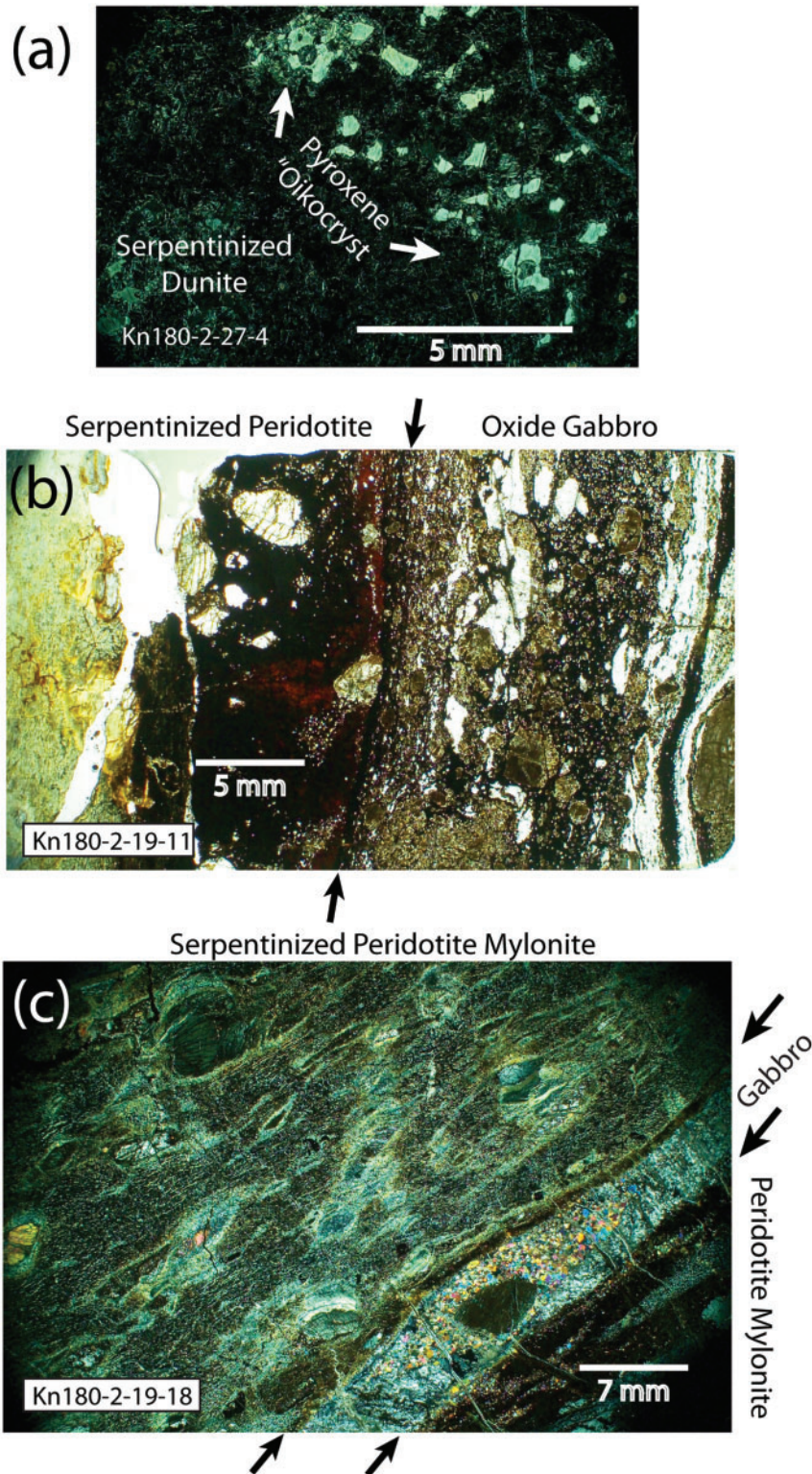


Fig. 9. (a) Photomicrograph of a clinopyroxene (pseudomorphed) bastite oikocryst in poikilitic dunite sample Kn180-2-27-4. The white blebs all have uniform extinction and cleavage, demonstrating that they originally formed a single clinopyroxene grain. Groundmass is entirely serpentinized and argillitized olivine. (b) Oxide gabbro vein ($An_{38.3}$, Cpx Mg-number 70.0) cutting serpentinized porphyroclastic peridotite in sample Kn180-2-19-11 (Opx Mg-number core 82.4, rim 73.0). Arrows point to contact between the peridotite (stained dark red near the contact) and the gabbro. Gabbro shows intense grade 3 mylonite crystal-plastic deformation, whereas the peridotite is a grade 1.5 porphyroclastic peridotite. (c) Gabbro vein (An_{41} , Cpx Mg-number 73.7) intruding spinel harzburgite (Sp Cr-number 30.0, Cpx Mg-number 91.1, Opx Mg-number 90.9) in sample Kn180-2-19-18. Both gabbro and peridotite are crystal-plastic deformation grade 3 mylonites.

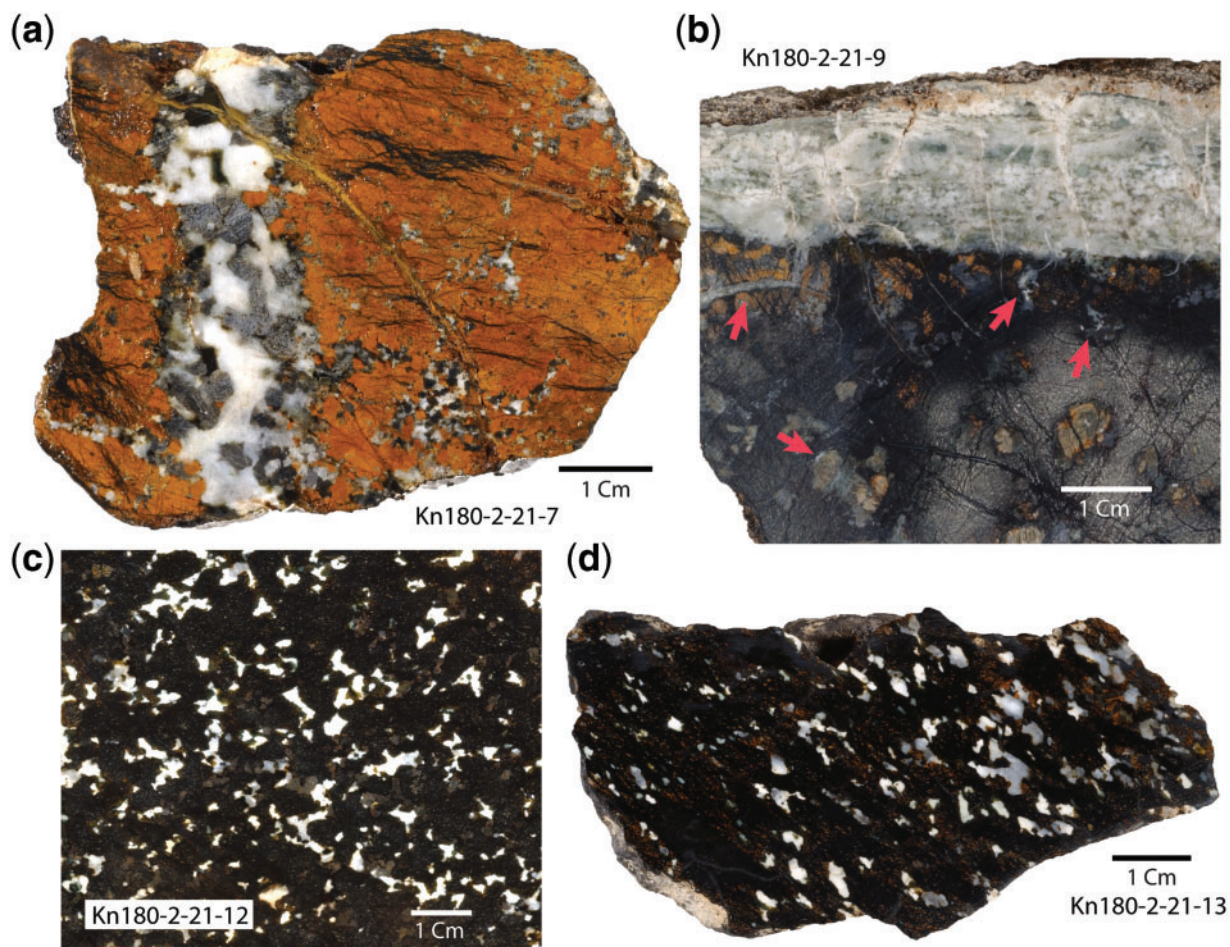


Fig. 10. Kane Megamullion dunitites, gabbro veins and troctolites. (a) Kn180-2-21-7 dunite crosscut by olivine gabbro vein (Fo_{82.3}, An_{60.5}, Cpx Mg-number 83.3, Sp Cr-number 58.0), with apophyses leading into the dunite, which is irregularly impregnated with clinopyroxene and plagioclase. Olivine in dunite is virtually 100% argillitized to orange–brown clay. (b) Kn180-2-21-9 partially serpentinized plagioclase peridotite crosscut by a crystal-plastically deformed troctolite vein. (Note apophyses extending from the main vein into the peridotite and patches of white prehnite–chlorite after plagioclase indicated by red arrows.) (c) Kn180-2-21-12 olivine-rich troctolite interpreted as disaggregated dunite (Fo_{84.9}) impregnated by plagioclase (An_{66–72.9}) and granular clinopyroxene (Mg-number 87.6). (d) Kn180-2-21-13 foliated olivine-rich troctolite (Fo_{86.1}, An_{74.2}, Cpx Mg-number 87.2).

the detachment faulting that often localized on the veins rather than the enclosing peridotites (Fig. 9b). Less often the veins were deformed with the peridotite (Fig. 9c). This is similar to the preferential deformation of gabbro veins in the MAR 14–16°N Ocean Drilling Program (ODP) Leg 209 peridotites (Kelemen *et al.*, 2004).

Gabbro veins are not uniformly distributed across the Kane Megamullion. Primitive varieties are largely limited to the crust–mantle transition zone suite around Adam and Eve Domes, whereas more evolved oxide gabbro and olivine gabbro predominate at Cain and Abel Domes to the north. In general, chilled margins are uncommon, and in many cases the actual contacts with the peridotites are sutured (e.g. Fig. 10a), with the vein and host minerals interlocking across the contact. Host peridotites do not

always have plagioclase present, but where present it is interstitial and appears related to the vein (Fig. 10a and b). This indicates that the peridotites were at or very close to the melt temperature, as otherwise impregnation would have been prohibited by formation of chilled margins.

Ultramafic veins

In addition to the gabbroic veins, an olivine websterite, an orthopyroxenite, and a plagioclase orthopyroxenite were found. The olivine websterite has mineral compositions very similar to the typical depleted Kane Megamullion spinel peridotite (Fo_{90.5}, spinel Cr-number 33.7, Cpx Na₂O 0.10 wt %), and the orthopyroxenites have similarly high-magnesium pyroxene with relatively low alumina contents, particularly on their rims. The orthopyroxenite

plagioclase is some of the most calcic found at Kane Megamullion (An₉₅₋₆). Figure 1 in the online supplementary data shows plagioclase orthopyroxenite Jas112-64 from Cain Dome in contact with weathered harzburgite and cross-cut by a sheared oxide gabbro vein intruded at high temperature (no chill zone), along a fault that offset the peridotite-pyroxenite contact. This demonstrates a) a high-temperature origin for the pyroxenite, b) that it predates intrusion of the oxide gabbros, c) that intrusion of the oxide gabbros occurred under anhydrous conditions near the brittle-ductile transition.

Dunites

Dunite occurs in two parageneses at the Kane Megamullion: first as isolated samples from massive mantle outcrops where the East Fault exposes the basement beneath Cain Dome, and in a dredge from the south side of Abel Dome (Dive 113 and Dredges 5 and 18). Nine additional dredges and dives recovering peridotite from Cain and Abel Domes failed to recover dunite, and it amounts to only 1.2 vol. % of the peridotites from there. These dunites crosscut harzburgite in some samples, and often contain accessory or small segregations of spinel. The contacts are usually sharp, with the abrupt disappearance of pyroxene. Such dunites, though volumetrically small, occur widely in ophiolites and in abyssal peridotite dredges. They are generally interpreted as products of melt–rock reaction during focused melt flow as the phase field of olivine expands and that of pyroxene contracts in an ascending melt (e.g. Dick, 1977; Kelemen *et al.*, 1997; Quick, 1981b; Suhr, 1999). The second dunite paragenesis is in close association with harzburgite and massive gabbro and troctolite at Adam and Eve Domes in the southern third of the Kane Megamullion. This suite is considerably more complex, and appears to represent an exceptional *in situ* exposure of the crust–mantle transition zone, and we therefore describe it in detail below.

Adam Dome Magmatic Complex

At the Adam Dome Magmatic Complex gabbros intercalated with sheeted dikes were sampled in massive outcrops on the face of West Fault by two Jason Dive 117 traverses and Dredges 25 and 27 (see Dick *et al.*, 2005, fig. 8). Primitive troctolite, olivine gabbro and oxide gabbro were found in nearly equal proportion (Lissenberg & Dick, 2006). Although we lack whole-rock data, these rocks from Hole 735B, added in equal proportions, have a bulk composition similar to primitive MORB (Mg-number 68.5). Such proportions then, including some dunite, are roughly those expected for *in situ* differentiation of a parental melt. Post-cumulus melt–rock reaction progressively replaced olivine with Cpx and calcic plagioclase with more sodic plagioclase, buffering melt compositions and progressively reacting troctolite to olivine gabbro

(Lissenberg & Dick, 2008). Some gabbros then underwent crystal-plastic deformation not seen in the dikes, indicating that the section was intruded and subsequently recrystallized at depth prior to emplacement into the zone of dike injection (Dick *et al.*, 2008). Dredge 27 at the northern flank of Adam Dome recovered a suite of five troctolites, 36 olivine gabbros, and 21 oxide gabbros similar to the main magmatic complex. Twenty of these have crystal-plastic deformation ranging up to ultramylonite. The dredge, however, also recovered 15 dunites, 22 poikilitic dunites, two plagioclase dunites, and 10 plagioclase-harzburgites and metaperidotites, one with a dunite–harzburgite contact. Consequently, we believe that the dredge crossed the distal end of the complex near the detachment fault surface, sampling both the base of the gabbro section and underlying rocks from the crust–mantle transition zone.

The Dredge 27 dunites range from pure olivine with accessory chrome spinel, to poikilitic dunite with 1–4% Cpx oikocrysts and 0–10% plagioclase. Fourteen of the dunites and two plagioclase harzburgites have veins ranging from troctolite to gabbro. As a result of intense alteration, little primary mineralogy is left; however, textural interpretation can be made from plagioclase and Cpx pseudomorphs. Cpx occurs as ~1 cm oikocrysts, as either a series of isolated blebs at olivine triple junctions with uniform extinction (Fig. 9a), or as fully connected sponge-like crystals enclosing or partially enclosing numerous round olivines. Plagioclase is interstitial to olivine, often occurring as sub-triangular patches mimicking triple junctions. Poikilitic dunite is characterized by Cpx oikocrysts, although plagioclase is usually more abundant and sometimes occurs by itself. The delicate Cpx oikocrysts suggest little deformation, although in the one case with relict plagioclase the latter has deformation twins. Fine-grained ~0.1–0.4 mm equant anhedral to euhedral spinel is ubiquitous at 0.5–2 vol. %, contrasting sharply with the generally coarser 0.1–2.5 mm holly-leaf and vermicular spinel in the harzburgites and lherzolites. One sample also contains minor ophitic brown amphibole enclosing olivine instead of Cpx (Kn180-2-27-33). The poikilitic dunites were originally described as wehrlitic dunites in hand sample (Dick *et al.*, 2008), but in nine thin sections, all but one, with a single Cpx oikocryst, contained previously undetected plagioclase pseudomorphs.

The troctolites are texturally heterogeneous, ranging from fine- to coarse-grained. Olivine is interstitial to plagioclase in some and the reverse in others. Four samples have near cotectic proportions of equigranular plagioclase and olivine (~60:40), including a vein in a poikilitic dunite with branches extending into and locally impregnating it, which indicates direct cumulate crystallization from a melt. One olivine-rich troctolite which has a sutured contact with a 2 cm olivine gabbro vein

(Kn180-2-27-37), however, is texturally and compositionally distinct. It consists of 10–15% plagioclase pseudomorphs in bleb-like interstitial arrays at olivine triple junctions, ~3% fine-grained equant spinel and <1% fine-grained equant Cpx. The olivine-rich troctolite is clearly texturally transitional to the poikilitic dunites and appears to have formed by impregnation of dunite.

Dredge 28 on the back-tilted detachment fault surface on the east side of Adam Dome recovered abundant granular harzburgite and two dunites. Both dunites are in contact with peridotite, and one has a few medium-grained patches of plagioclase and clinopyroxene. A chrome-spinel olivine-gabbro vein occurs in one dunite. Numerous other olivine-rich (20–35%) gabbro and equigranular oxide gabbro veins occur in the peridotites, with four tabular oxide gabbro mylonite fragments appearing to be broken-out veins. Both plagioclase-bearing and plagioclase-free harzburgite and lherzolite occur. The olivine-rich gabbro has sutured contacts with the peridotite where vein and matrix minerals interlock. This and the absence of chill zones suggest melt–rock reaction, and thus the olivine-rich gabbros are probably high-temperature veins associated with melt impregnation in the plagioclase peridotites. The oxide gabbros, with sharp contacts produced by brittle fracturing, however, appear to represent later intrusions when the host peridotite was cooler.

Dredge 21, where East Fault cuts Eve Dome, recovered dunite, olivine-rich troctolite, and harzburgite cut by numerous veins ranging from troctolite to oxide gabbro. Eve dome is small compared with Adam Dome to the west, and seismic data suggest that the basement east of Adam Dome consists of a mixture of small gabbro bodies intruded into partially serpentinized mantle, rather than the large body found at Adam Dome (Canales *et al.*, 2008). Dredge 21, then, may represent the underpinnings of the Adam Dome Magmatic Complex, brought to the surface by continued detachment faulting as local magmatic accretion waned.

Little olivine is left in the Eve Dome dunites, and interpretation is again based on spinel textures, plagioclase pseudomorphs and some relict Cpx. The dunites, and most olivine-rich troctolites, have the same small equant 0.1–1.5 mm anhedral to subhedral or euhedral chromian spinel (mostly 0.1–4 mm) as in the Dredge 27 samples. The dunite is very irregularly impregnated by interstitial plagioclase and small amounts (up to 5%) of fine granular Cpx. The plagioclase pseudomorphs often have dentate contacts with the olivine pseudomorphs, suggesting dissolution–reprecipitation where olivine reacted with the impregnating melt. The olivine-rich troctolites, in turn, appear to be largely partially to fully disaggregated dunite, with much less plagioclase (~20%) than expected for direct cotectic crystallization. They consist of often

idiomorphic olivine, with flat faces partially enclosed by interstitial plagioclase (Fig. 10c). Fine-grained granular Cpx appears to have co-precipitated with the plagioclase. Experiments show that this olivine texture can be produced by reaction between melt and a disaggregating dunite or peridotite (Boudier, 1991; Van Den Bleeken *et al.*, 2009). Similar olivine-rich troctolites have been described from the Oman crust–mantle transition zone (Boudier & Nicolas, 1995). One troctolite is strongly foliated (Fig. 10d) with little evidence of crystal-plastic deformation, indicating mineral alignment by crystal mush flow.

Gabbroic veins in the harzburgite and dunite are highly altered, and include troctolites with sutured contacts with interlocking vein and matrix mineralogies. Plagioclase and Cpx often impregnate harzburgite and dunite adjacent to veins, which locally branch into the peridotite (Fig. 10a and b). These veins again appear to be cogenetic with peridotite and dunite impregnation, as they are in the Oman transition zone. Oxide gabbro veins also occur, but like Dredge 28, they appear to be later than the troctolites.

MINERALOGY

Analytical procedures

Major elements were analyzed *in situ* on polished thin sections using a JEOL JXA-733 Superprobe at MIT, operated at 15 kV accelerating potential with a 10 nA beam current. Analyses were calibrated using silicate minerals and Cr-spinel. Olivine, spinel, and plagioclase were analyzed with a 10 µm beam. Counting times were typically 40 s on peak and background. Six points were analyzed per grain with random points on olivine, where grain boundaries are indistinct because of alteration, and as core–rim traverses in spinel and plagioclase. Because of mutual exsolution, pyroxene bulk compositions were determined using contiguous 10-spot traverses on cores and rims. Data reduction used modified matrix correction factors (Bence & Albee, 1968; Albee & Ray, 1970). Analyses were discarded if average totals were outside 98.5–101.5 wt %, or if point totals were not within the expected 2σ analytical standard deviation. Based on repeat basalt glass analyses, elements occurring at >10 wt % are reproducible within 2%, elements at <10 wt % are reproducible within 5%, and elements at <1 wt % level are reproducible within 30% (Gaetani & Grove, 1998). Tables 2–6 give representative data, and the full dataset is given in Electronic Appendix 1 (available for downloading at <http://www.petrology.oxfordjournals.org>).

Olivine

Olivine in the peridotites has a large range of composition (Fo 78.6–92.4) compared with typical residual plagioclase-free abyssal peridotites (Fo 89.5–91.5). In general, plagioclase peridotites tend to have iron-rich olivine compared with plagioclase-free peridotites (Fig. 11),

Table 2: Olivine compositions

Sample	Lithology	SiO ₂	TiO ₂	Al ₂ O ₃	Cr ₂ O ₃	FeO	MnO	MgO	CaO	NiO	Total	Fo	Notes
<i>Knorr Cruise 180 Leg 2, Main Core Complex</i>													
Dr5-29	Harzburgite	41.1	0.00	0.03	0.05	8.43	0.13	50.7	0.07	0.37	100.8	91.5	Alteration vein
Dr5-31	Olivine websterite	40.4	0.00	0.00	0.00	9.26	0.15	49.7	0.02	0.41	99.9	90.5	Vein in harzburgite
Dr14-37	Harzburgite	40.6	0.01	0.00	0.01	8.98	0.13	50.3	0.04	0.34	100.4	90.9	
Dr14-66	Harzburgite	40.9	0.00	0.00	0.02	9.25	0.15	49.4	0.02	0.33	100.0	90.5	Metagabbro veins
Dr14-70	Lherzolite	39.2	0.01	0.00	0.02	16.66	0.23	43.3	0.02	0.33	99.9	82.3	
Dr17-18	Harzburgite	40.4	0.00	0.00	0.01	8.88	0.10	49.5	0.02	0.37	99.3	90.9	
Dr21-4	Harzburgite	40.8	0.01	0.00	0.01	9.18	0.12	50.0	0.06	0.37	100.5	90.7	
Dr21-7b	Olivine gabbro	38.9	0.02	0.02	0.01	16.73	0.24	43.2	0.03	0.18	99.4	82.2	Vein in Pl-Cpx Dunite
Dr21-9a	Pl harzburgite	40.3	0.01	0.00	0.02	9.56	0.17	49.0	0.05	0.28	99.3	90.1	Troctolite vein
Dr21-12HD	Olivine-rich troctolite	39.5	0.03	0.01	0.01	14.36	0.20	45.4	0.07	0.23	99.7	84.9	
Dr21-12JL	Olivine-rich troctolite	39.4	0.00	0.00	0.00	14.46	0.20	45.6	0.05	0.22	99.9	84.9	
Dr21-13	Olivine-rich troctolite	40.0	0.00	0.00	0.00	13.26	0.19	46.2	0.03	0.20	100.0	86.1	
Dr21-14	Olivine-rich troctolite	40.0	0.00	0.00	0.00	12.33	0.16	47.4	0.02	0.16	100.1	87.3	
Dr27-37b	Olivine gabbro	40.1	0.01	0.01	0.00	10.95	0.15	48.3	0.05	0.28	99.8	88.7	Vein in Ol-rich troctolite
Dr27-38b	Troctolite	39.9	0.00	0.00	0.00	11.24	0.17	47.9	0.07	0.31	99.6	88.4	Chlorite vein
Jas112-1	Harzburgite	40.6	0.00	0.02	0.00	9.12	0.12	49.8	0.05	0.37	100.1	90.7	Chlorite vein
Jas 112-44	Harzburgite	40.6	0.01	0.00	0.01	9.27	0.13	49.6	0.06	0.38	100.0	90.5	Chl-Am vein
Jas 112-49	Harzburgite	41.1	0.00	0.00	0.00	9.35	0.12	49.4	0.03	0.38	100.4	90.4	
Jas112-63	Lherzolite	40.6	0.00	0.00	0.00	8.95	0.14	49.3	0.06	0.37	99.5	90.8	Tc vein
Jas112-71	Harzburgite	40.9	0.00	0.00	0.00	8.92	0.12	49.4	0.04	0.36	99.8	90.8	Tc-Chl vein
Jas112-84	Harzburgite	40.8	0.00	0.00	0.00	9.12	0.14	49.6	0.05	0.36	100.0	90.6	
Jas113-38	Dunite	40.2	0.00	0.00	0.03	10.12	0.16	48.5	0.02	0.37	99.4	89.5	Tc-Tr schist
Jas 113-55a	Harzburgite	39.6	0.03	0.01	0.03	14.73	0.22	44.9	0.05	0.37	100.0	84.5	Oxide gabbbronorite vein
Jas113-57b	Pl harzburgite	38.6	0.01	0.00	0.01	19.69	0.31	40.7	0.06	0.28	99.6	78.6	Oxide pigeonite gabbro vein
Jas113-59a	Pl harzburgite	39.4	0.02	0.00	0.03	17.19	0.25	42.9	0.07	0.30	100.1	81.6	Gabbbronorite vein
Jas113-71	Harzburgite	40.1	0.00	0.00	0.00	10.89	0.13	47.9	0.03	0.37	99.4	88.7	Tc-Serp-Ap schist
Jas114-19a	Harzburgite	41.0	0.00	0.01	0.00	9.21	0.14	50.3	0.02	0.38	101.0	90.7	Gabbro vein
Jas 114-20	Harzburgite	40.9	0.00	0.00	0.00	8.82	0.14	50.0	0.01	0.36	100.2	91.0	
<i>Kanaut Expedition transform wall peridotites from Ghose (1997)</i>													
D1-1B-1	Peridotite	40.7	0.01	0.00	0.00	9.86	0.14	49.1	0.01	0.39	100.2	89.9	Porphyroclastic
D2-2-2	Peridotite	40.4	0.01	0.00	0.00	9.46	0.13	48.7	0.05	0.37	99.2	90.2	Porphyroclastic
D2-3-1	Peridotite	40.0	0.00	0.20	0.03	9.28	0.13	49.4	0.01	0.38	99.4	90.5	Mylonite
D2-3-4a	Peridotite	40.3	0.01	0.01	0.02	11.71	0.17	47.5	0.03	0.33	100.1	87.9	Mylonite
D2-3-5a	Peridotite	40.9	0.01	0.00	0.00	9.50	0.14	50.7	0.02	0.34	101.6	90.5	Mylonite
D2-3-10	Peridotite	39.8	0.01	0.00	0.01	14.58	0.23	45.1	0.03	0.33	101.6	84.6	Mylonite
Kan12-9	Peridotite	40.5	0.00	0.00	0.01	9.36	0.16	49.4	0.06	0.37	99.8	90.4	Mylonite
Kan14-6	Peridotite	40.9	0.00	0.00	0.00	9.39	0.12	49.2	0.07	0.38	100.0	90.3	
Kan14-8	Peridotite	41.1	0.00	0.00	0.01	8.80	0.12	50.0	0.03	0.39	100.5	91.0	
Kan15-3	Peridotite	40.4	0.01	0.00	0.03	9.44	0.17	49.8	0.08	0.38	100.3	90.4	
Kan16-5	Peridotite	39.2	0.01	0.00	0.00	14.23	0.20	45.4	0.01	0.31	99.4	85.0	
Kan16-7	Peridotite	39.7	0.01	0.00	0.01	13.79	0.17	44.8	0.01	0.31	98.8	85.3	

Table 3: Representative orthopyroxene compositions

Sample	Lithology	SiO ₂	TiO ₂	Al ₂ O ₃	Cr ₂ O ₃	FeO	MnO	MgO	CaO	Na ₂ O	Total	Mg-no.	En	Fs	Wo	Notes
<i>Knorr Cruise 180 Leg 2 Main Core Complex</i>																
Dr5-31	Olivine websterite	54.4	0.02	3.61	0.74	5.86	0.11	32.4	2.25	0.00	99.4	90.8	86.8	8.8	4.4	Vein in harzburgite
Dr14-37	Harzburgite	55.1	0.05	3.73	0.78	5.86	0.14	32.3	1.81	0.12	99.9	90.8	87.5	8.9	3.5	
Dr14-66	Harzburgite	54.8	0.06	4.04	0.90	5.82	0.14	31.7	1.99	0.05	99.5	90.7	87.1	9.0	3.9	Metagabbro veins
Dr15-26	Harzburgite	54.3	0.02	4.07	0.90	5.72	0.09	32.3	2.09	0.02	99.5	91.0	87.2	8.7	4.1	
Dr21-4	Harzburgite	55.5	0.01	3.69	0.85	5.93	0.10	32.7	1.92	0.02	100.8	90.8	87.4	8.9	3.7	
Dr21-8a	Harzburgite	55.6	0.02	3.86	0.81	6.03	0.15	32.6	1.70	0.02	100.8	90.6	87.6	9.1	3.3	Oxide gabbro vein
Dr21-9a	Pl harzburgite	55.9	0.02	2.55	0.86	6.19	0.16	33.0	1.93	0.02	100.7	90.5	87.2	9.2	3.7	Troctolite vein
Dr27-2c	Pl harzburgite	55.7	0.15	2.69	0.80	6.17	0.13	32.9	1.82	0.06	100.5	90.5	87.3	9.2	3.5	Dunite & metagabbro veins
Dr28-9a	Pl harzburgite	56.1	0.15	2.16	0.70	6.59	0.14	32.6	1.90	0.06	100.4	89.8	86.5	9.8	3.7	Olivine gabbro vein
Dr28-13b	Sp-Ol gabbro	55.6	0.08	2.33	0.70	6.06	0.13	33.2	1.72	0.01	99.8	90.7	87.7	9.0	3.3	Vein in harzburgite
Dr28-16	Pl harzburgite	56.4	0.08	2.16	0.71	6.87	0.14	33.2	1.27	0.04	100.8	89.6	87.4	10.2	2.4	Gabbro vein
Jas 112-49	Harzburgite	55.2	0.03	3.51	0.71	6.07	0.14	32.1	1.47	0.03	99.3	90.4	87.8	9.3	2.9	
Jas112-64	Pl orthopyroxenite	55.2	0.07	3.66	0.63	6.20	0.14	32.2	2.19	0.00	100.2	90.2	86.4	9.3	4.2	
Jas 112-65	Orthopyroxenite	55.7	0.07	2.71	0.63	6.29	0.14	33.1	1.32	0.00	100.0	90.4	88.1	9.4	2.5	
Jas 112-84	Harzburgite	54.9	0.05	3.89	0.79	6.08	0.10	32.8	1.95	0.02	100.6	90.6	87.2	9.1	3.7	
Jas 113-59a	Pl harzburgite	53.8	0.10	3.19	0.74	11.59	0.22	28.9	1.58	0.04	100.2	81.7	79.1	17.8	3.1	Gabbro vein
Jas113-59b	Gabbro	52.7	0.46	1.51	0.01	18.39	0.41	23.7	2.21	0.04	99.4	69.7	66.6	28.9	4.5	Vein in harzburgite

Table 4: Representative clinopyroxene compositions

Sample	Lithology	SiO ₂	TiO ₂	Al ₂ O ₃	Cr ₂ O ₃	FeO	MnO	MgO	CaO	Na ₂ O	Total	Mg-no.	En	Fs	Wo	Notes
<i>Knorr Cruise 180 Leg 2 Main Core Complex</i>																
Dr19-11b	Oxide gabbro	50.9	1.03	2.78	0.05	11.84	0.30	15.4	17.0	0.45	99.8	70.0	44.9	19.4	35.7	Vein in harzburgite
Dr19-18a	Gabbro	52.4	0.69	2.42	0.06	9.38	0.28	14.7	19.7	0.48	100.1	73.7	42.9	15.4	41.7	Vein in harzburgite
Dr21-7b	Ol gabbro	51.8	0.66	2.99	0.30	5.85	0.16	17.1	20.2	0.38	99.4	83.9	48.9	9.4	41.6	Vein in Pl-Cpx dunite
Dr27-37b	Ol gabbro	50.2	0.79	4.07	1.24	3.34	0.19	18.1	20.2	0.44	98.5	90.6	52.5	5.4	42.1	Vein in Ol-rich troctolite
Dr28-13b	Sp-Ol gabbro	52.1	0.19	3.87	1.43	2.83	0.10	18.0	20.7	0.50	99.7	91.9	52.2	4.6	43.2	Vein in harzburgite
Dr21-12	Troctolite	50.0	1.49	4.21	1.24	4.11	0.13	15.9	21.4	0.53	99.0	87.3	47.2	6.9	45.9	
Dr27-37a	Troctolite	51.9	0.75	3.52	1.39	2.92	0.11	16.8	22.2	0.52	100.1	91.1	48.8	4.8	46.4	
Dr21-9b	Troctolite	51.5	0.38	4.04	1.53	2.67	0.11	16.9	22.2	0.63	100.0	91.9	49.2	4.4	46.4	Vein in Pl-harzburgite
Dr27-3	Poikilitic dunite	52.2	0.40	3.44	1.40	2.89	0.11	18.6	20.5	0.46	99.9	92.0	53.1	4.6	42.2	
Dr5-31	Ol websterite	51.4	0.08	4.68	1.23	3.29	0.07	19.5	19.0	0.10	99.4	91.6	55.6	5.2	39.1	Vein in harzburgite
Dr27-2c	Pl harzburgite	52.1	0.54	4.58	1.37	2.59	0.08	16.4	22.2	0.74	100.6	91.9	48.6	4.3	47.1	Dunite & metagabbro veins
Dr28-16	Pl harzburgite	53.4	0.23	2.43	1.30	2.66	0.07	17.5	22.8	0.42	100.8	92.2	49.5	4.2	46.3	Gabbro vein
Dr28-9a	Pl harzburgite	50.6	0.44	4.43	1.03	3.37	0.10	17.1	20.6	0.43	98.2	90.0	50.6	5.6	43.8	Ol gabbro vein
Jas 113-59a	Pl harzburgite	51.2	0.13	4.51	1.36	4.92	0.14	16.3	21.4	0.34	100.3	85.7	47.3	8.0	44.7	Gabbro vein
Dr21-9a	Pl harzburgite	52.4	0.25	4.05	1.47	3.51	0.12	18.7	19.7	0.41	100.6	90.5	53.6	5.6	40.8	Troctolite vein
Dr14-37	Harzburgite	52.5	0.09	3.62	1.25	2.08	0.07	17.7	21.4	0.81	99.6	93.8	51.7	3.4	44.9	
Dr14-66	Harzburgite	52.2	0.13	4.26	1.17	2.40	0.10	17.4	22.4	0.23	100.4	92.9	49.9	3.8	46.3	Metagabbro vein
Dr15-26	Harzburgite	51.4	0.07	4.86	1.30	2.73	0.05	18.6	20.5	0.11	99.6	92.5	53.3	4.4	42.4	
Dr21-4	Harzburgite	52.1	0.07	4.94	1.36	3.31	0.07	19.3	19.7	0.13	101.0	91.4	54.4	5.2	40.4	
Dr21-8a	Harzburgite	51.5	0.08	5.14	1.29	2.70	0.11	17.2	21.6	0.26	99.9	91.9	50.2	4.4	45.3	Oxide gabbro vein
Jas 112-49	Harzburgite	51.4	0.10	5.03	1.36	3.23	0.10	18.8	19.5	0.11	99.6	91.4	54.1	5.2	40.7	
Jas 112-84	Harzburgite	50.4	0.15	5.77	1.56	2.75	0.07	16.8	22.5	0.08	100.1	91.6	48.7	4.5	46.8	

Table 5: Representative spinel compositions

Sample	Lithology	SiO ₂	TiO ₂	Al ₂ O ₃	Cr ₂ O ₃	Fe ₂ O ₃	FeO	MnO	MgO	CaO	NiO	Total	Mg-no.	Cr-no.	Fe3-no.	Notes
Dr5-31	Olivine websterite	0.02	0.09	39.0	29.6	1.39	14.1	0.18	15.6	0.01	0.21	100.2	66.5	33.7	1.5	Vein in harzburgite
Dr14-37	Harzburgite	0.05	0.05	39.7	28.2	2.85	12.5	0.21	16.7	0.00	0.24	100.5	70.5	32.3	3.0	
Dr14-66	Harzburgite	0.06	0.05	40.1	28.2	1.82	12.9	0.18	16.4	0.00	0.22	100.1	69.4	32.1	1.9	Metagabbro veins
Dr15-26	Harzburgite	0.06	0.05	40.7	27.7	1.69	12.6	0.14	16.7	0.00	0.18	99.8	70.2	31.3	1.8	
Dr18-42	Dunite	0.03	0.21	29.4	34.5	5.33	16.8	0.20	12.7	0.02	0.21	99.6	57.3	44.1	6.1	
Dr21-4	Harzburgite	0.02	0.05	41.0	28.8	0.80	12.2	0.12	17.0	0.00	0.18	100.3	71.3	31.8	0.8	
Dr21-7b	Olivine gabbro	0.01	3.51	16.4	33.7	12.28	25.5	0.36	7.5	0.00	0.12	99.6	34.3	58.0	16.7	Vein in Pl-dunite with Ol-gabbro vein
Dr21-8a	Harzburgite	0.03	0.04	40.6	28.5	1.12	13.1	0.16	16.4	0.00	0.20	100.2	69.0	32.0	1.2	Oxide gabbroironite vein
Dr21-9a	Pl harzburgite	0.06	0.42	26.0	42.3	2.45	16.1	0.29	13.2	0.00	0.12	101.2	59.4	50.7	2.8	Troctolite vein
Dr21-9b	Troctolite vein	0.00	0.31	27.7	40.7	2.56	16.1	0.31	13.3	0.01	0.10	101.3	59.6	48.2	2.9	Vein in Pl-harzburgite
Dr21-11	Pl dunite	0.00	0.68	27.5	34.6	6.56	16.0	0.23	13.2	0.00	0.13	99.0	59.5	45.8	7.6	
Dr21-12	Troctolite	0.04	3.03	19.8	35.3	9.03	22.0	0.32	10.0	0.00	0.18	99.8	44.7	54.4	11.7	
Dr27-2c	Pl harzburgite	0.00	0.68	28.3	39.4	2.59	15.5	0.18	14.1	0.00	0.14	101.0	62.0	48.2	2.9	Dunite & metagabbro veins
Dr27-3	Poikilitic dunite	0.03	0.81	24.76	41.20	3.69	17.0	0.26	12.7	0.01	0.16	100.9	57.1	52.8	4.31	
Dr27-4	Poikilitic dunite	0.01	1.09	24.6	41.0	3.44	16.8	0.28	12.9	0.00	0.09	100.4	57.9	52.8	4.0	
Dr27-37a	Troctolite	0.00	1.86	23.5	40.0	3.58	19.4	0.31	11.5	0.03	0.14	100.5	51.3	51.0	4.3	Ol-gabbro vein
Dr27-37b	Olivine gabbro	0.00	2.21	22.8	41.5	2.68	19.5	0.29	11.7	0.00	0.11	101.0	51.7	53.2	3.2	Vein in Ol-rich troctolite
Dr27-38b	Troctolite	0.02	0.73	25.8	37.6	5.79	18.3	0.27	11.9	0.02	0.17	100.6	53.7	49.4	6.8	Vein in poikilitic dunite
Dr28-9a	Pl harzburgite	0.01	0.32	25.9	40.8	2.19	18.6	0.28	11.4	0.00	0.03	99.8	52.2	51.4	2.6	Ol gabbro vein
Dr28-13b	Sp-Ol gabbroironite	0.02	0.34	27.6	40.2	1.24	18.4	0.28	11.6	0.00	0.17	99.9	53.0	48.7	1.4	Vein in harzburgite
Dr28-16	Pl harzburgite	0.01	0.40	24.3	43.9	1.49	18.9	0.27	11.2	0.00	0.08	100.8	51.4	54.8	1.7	Gabbro vein
Jas112-49	Harzburgite	0.11	0.05	43.4	25.9	0.55	12.6	0.16	16.9	0.01	0.19	100.2	70.5	28.6	0.6	
Jas112-84	Harzburgite	0.03	0.02	41.0	26.6	2.26	11.7	0.14	17.1	0.00	0.23	99.2	72.1	30.3	2.4	
Jas113-41	Dunite	0.04	0.08	36.8	29.7	3.18	14.4	0.17	15.1	0.00	0.18	99.8	65.2	35.1	3.5	
Jas113-59a	Pl harzburgite	0.06	0.83	25.3	31.7	10.17	24.7	0.34	7.5	0.01	0.18	101.2	35.2	45.6	12.2	Gabbroironite vein

accounting for some of this variability. The large composition range, however, is also due to intrusion of the gabbroic veins, which resulted in or accompanied impregnation by plagioclase and Cpx crystallized from trapped or transient melt. This effect, as elsewhere (e.g. Tartarotti *et al.*, 1995b), is generally limited to within a few centimeters of a vein. In one sample, Fo₈₄ olivine occurs in a plagioclase-impregnated peridotite 1 cm from a gabbro vein (Fig. 11a). In another, olivine 1 cm from a vein shows substantial iron enrichment but no other evidence supporting melt impregnation, which, given the rapid diffusion of iron and magnesium in olivine at high temperature (e.g. Gaetani & Watson, 2000), suggests solid-state diffusion and re-equilibration between the vein and mantle matrix.

There is also considerable variability in olivine nickel content, with plagioclase peridotites tending to slightly lower nickel contents than spinel peridotites, and troctolites and olivine gabbro to significantly less (Fig. 12). There are two spinel peridotite peaks: Fo 90.5–91.0 for the main core complex (Fig. 11a), and a peak at Fo 90.0–90.5 for

the transform wall (Fig. 11b). Despite large local variability, however, no correlation between olivine composition and mineral mode is observed within dredge hauls or at a given locality.

Enstatite

Enstatite in the peridotites also has a large composition range partly as a result of melt impregnation and interaction with gabbroic veins. There is also highly variable alumina zoning, with rims depleted with respect to their cores. This effect is greatest in some plagioclase peridotites and near a gabbro vein (Fig. 13a). Little significant Mg–Fe zonation was observed (Fig. 13b). Plagioclase peridotites generally have lower Mg-number and alumina than spinel peridotites (Fig. 14d). The effect of veins on enstatite composition in the peridotites, as for olivine and the MARK mantle veins (Tartarotti *et al.*, 1995b; Cannat *et al.*, 1997), is also limited to within 1–2 cm. The most extreme chemical reaction between veins and peridotite

Table 6: *Plagioclase compositions*

Sample	Lithology	SiO ₂	Al ₂ O ₃	FeO	MgO	CaO	Na ₂ O	K ₂ O	Total	An	Ab	Or	Notes
<i>Knorr Cruise 180 Leg 2, Main Core Complex</i>													
Jas113-57a	Oxide pigeonite gabbro	47.5	34.4	0.07	0.01	16.81	1.93	0.00	100.7	82.8	17.2	0.0	Vein in Pl-harzburgite
Dr19-11b	Oxide gabbro	58.5	26.6	0.19	0.02	7.95	7.06	0.06	100.4	38.3	61.4	0.4	Vein in harzburgite
Dr19-12b	Gabbro	57.2	28.0	0.14	0.06	9.32	6.00	0.06	100.7	46.0	53.6	0.3	Vein in harzburgite
Jas113-59b	Gabbro	45.3	35.6	0.07	0.01	18.62	1.00	0.01	100.7	91.1	8.8	0.1	Vein in Pl-harzburgite
Dr28-13b	Sp-Ol gabbro	46.9	34.2	0.07	0.01	17.57	1.60	0.00	100.4	85.8	14.1	0.0	Vein in Pl-harzburgite & dunite
Dr19-18a	Gabbro	57.7	26.7	0.13	0.04	8.66	6.81	0.08	100.1	41.0	58.5	0.4	Vein in harzburgite
Dr19-10b	Olivine gabbro	55.7	29.0	0.11	0.02	10.48	5.56	0.02	100.9	51.0	48.9	0.1	Vein in harzburgite
Dr21-7b	Olivine gabbro	53.1	30.2	0.22	0.07	12.37	4.45	0.02	100.4	60.5	39.4	0.1	Vein in Pl-Cpx-dunite
Dr27-37b	Olivine gabbro	51.7	31.0	0.05	0.03	13.85	3.75	0.03	100.4	67.0	32.8	0.2	Vein in troctolite
Dr28-9b	Olivine gabbro	51.4	31.9	0.12	0.03	13.87	3.62	0.01	100.9	67.9	32.1	0.0	Vein in Pl-harzburgite
Dr21-12JL	Troctolitic gabbro	49.4	32.3	0.22	0.07	15.03	3.07	0.03	100.1	72.9	27.0	0.1	Thin section 1
Dr21-12HD	Troctolite	51.5	31.1	0.27	0.07	13.39	3.80	0.03	100.1	66.0	33.9	0.1	Thin section 2
Dr21-9b	Troctolite	44.3	35.5	0.07	0.08	18.95	0.51	0.02	99.4	95.3	4.6	0.1	Vein in Pl-harzburgite
Dr21-13	Troctolite	49.5	32.6	0.23	0.03	14.95	2.86	0.03	100.2	74.2	25.6	0.2	
Dr21-14	Troctolite	48.6	33.3	0.21	0.10	16.08	2.52	0.02	100.8	77.8	22.1	0.1	
Dr27-37a	Troctolite	51.2	31.1	0.09	0.04	14.09	3.67	0.02	100.2	67.9	32.0	0.1	Ol-gabbro vein
Dr27-38b	Troctolite	48.9	33.9	0.17	0.05	16.14	2.39	0.01	101.6	78.8	21.1	0.0	Vein in poikilitic dunite
Dr27-3	Poikilitic dunite	49.7	32.6	0.12	0.05	14.82	2.86	0.00	100.1	74.1	25.9	0.0	
Jas112-64	Pl orthopyroxenite	44.6	36.5	0.08	0.02	19.21	0.48	0.02	100.9	95.6	4.3	0.1	Vein in peridotite with Oxide-gabbro vein
Dr21-9a	Pl harzburgite	45.6	31.3	0.19	0.05	20.20	1.01	0.01	98.4	91.1	8.8	0.1	Troctolite vein
<i>Kanaut Expedition transform wall peridotites from Ghose (1997)</i>													
D23-10	Pl peridotite	48.6	33.1	0.14	0.00	15.80	2.58	0.01	100.1	77.1	22.8	0.1	Mylonite
D23-10	Pl peridotite	51.2	30.7	0.20	0.70	13.35	3.67	0.02	99.8	66.7	33.2	0.1	Mylonite
D23-10	Pl peridotite	49.6	31.6	0.21	0.01	14.44	3.40	0.02	99.2	70.0	29.8	0.1	Mylonite
Kan16-5	Pl peridotite	54.2	29.5	0.37	0.08	11.33	4.99	0.04	100.5	55.5	44.2	0.2	
Kan16-5	Pl peridotite	55.1	28.8	0.50	0.02	11.17	5.23	0.04	100.9	54.0	45.8	0.2	
Kan16-5	Pl peridotite	54.1	28.9	0.42	0.07	10.96	5.08	0.04	99.6	54.3	45.5	0.2	
Kan16-5	Pl peridotite	57.1	28.1	0.08	0.02	9.21	6.06	0.01	100.6	45.6	54.3	0.1	
Kan16-5	Pl peridotite	57.2	26.2	0.11	0.02	7.75	5.00	3.22	99.4	37.6	43.9	18.6	
Kan16-5	Pl peridotite	56.2	27.7	0.16	0.03	9.50	6.07	0.14	99.8	46.0	53.2	0.8	
Kan16-5	Pl peridotite	52.2	28.7	1.89	0.83	11.05	4.56	0.00	99.2	57.2	42.8	0.0	
Kan16-5	Pl peridotite	55.6	27.3	0.18	0.40	9.73	6.03	0.07	99.3	46.9	52.6	0.4	
Kan16-5	Pl peridotite	55.5	27.9	0.20	0.02	10.01	6.19	0.02	99.8	47.1	52.7	0.1	
Kan16-5	Pl peridotite	53.4	28.4	0.42	0.77	10.76	5.10	0.03	98.9	53.7	46.1	0.2	

matrix was for the oxide gabbro veins from Cain and Abel Domes. Enstatite 0.5 cm from an oxide gabbro vein in Kn180-2-19-11 is strongly zoned from Mg-number 82.4 in the core to 73.0 on the rim. Enstatite 1 cm from an oxide pigeonite gabbro vein in Jas113-57 has an Mg-number of 89.0 in the core and 87.2 at the rim, whereas enstatite 1 cm from a gabbro vein in Jas113-59 is unzoned with core and rim Mg-numbers of 81.6 and 81.7.

Enstatite in most Kane Megamullion spinel peridotites lies within the transform peridotite field, which shows a

systematic overall decrease in alumina with increasing Mg-number and decreasing modal Cpx, consistent with increasing degree of partial melting (e.g. Dick & Fisher, 1984) (Fig. 14). Within the main core complex or in the transform wall suites, however, there is again no systematic correlation of alumina with Mg-number or with modal Cpx, although transform wall peridotites have systematically lower enstatite Mg-number, higher alumina and modal Cpx than in the main core complex (Figs 14b and 15b).

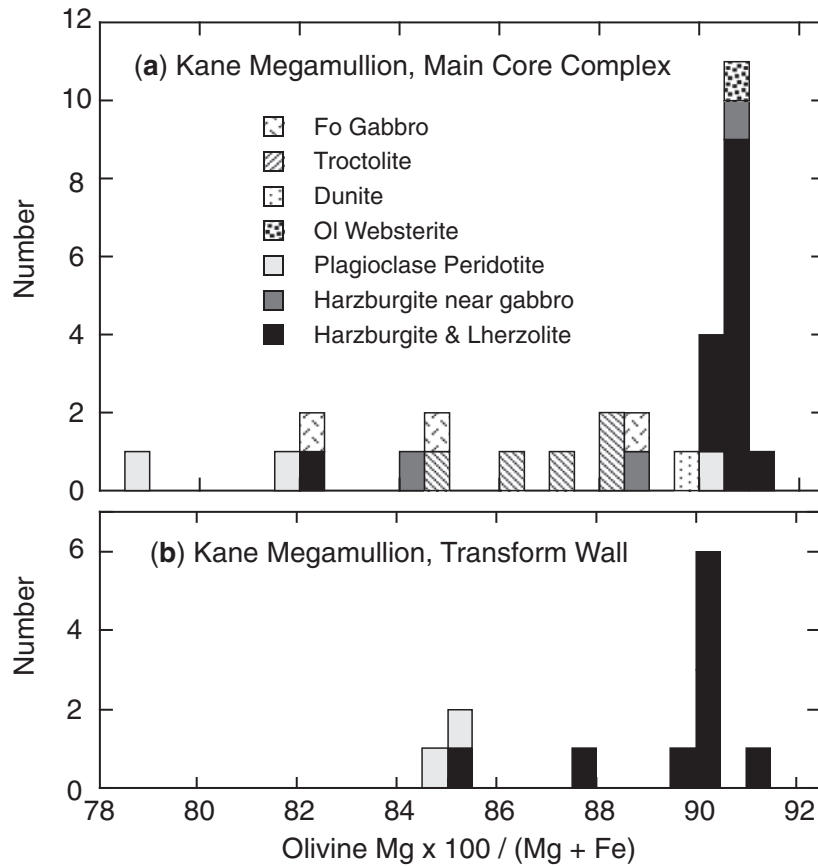


Fig. 11. Histograms comparing (a) olivine compositions from the Kane Megamullion main core complex area south of the transform wall with (b) those for peridotites from the transform wall. Transform wall data from Ghose (1997).

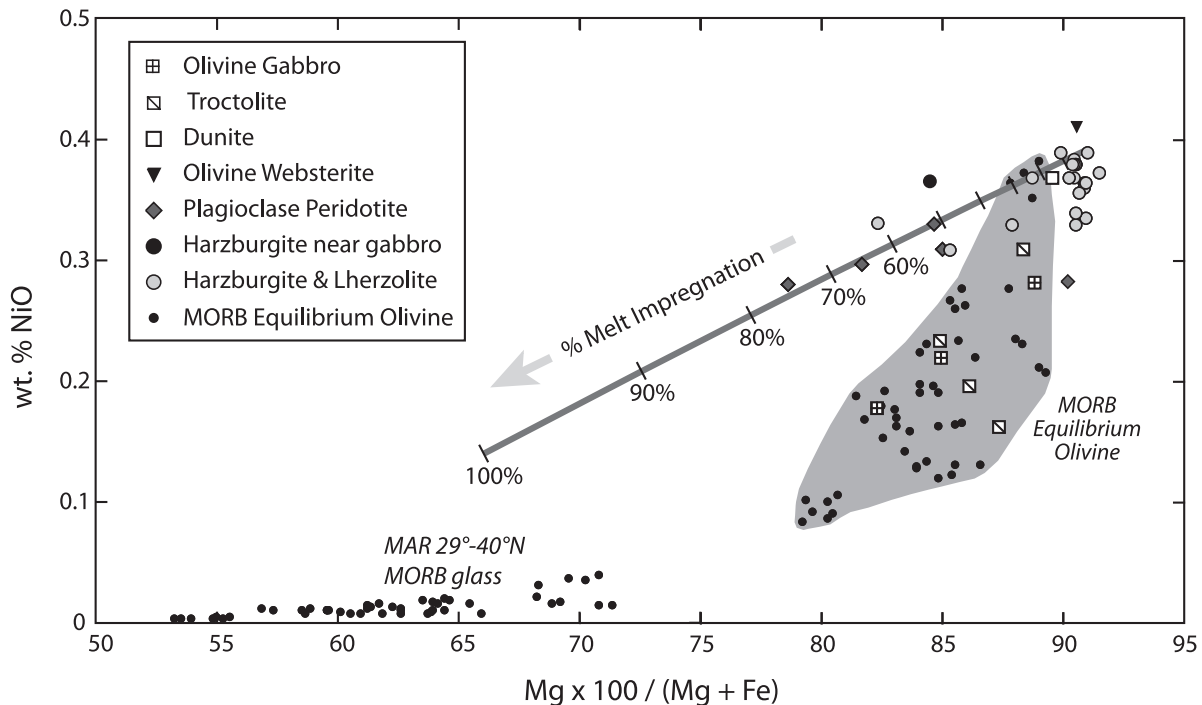


Fig. 12. Plot of nickel content vs Mg-number for olivine from Kane Megamullion peridotite, dunite, troctolite and olivine-gabbro. Also plotted are compositions of MAR 29–40°N MORB glasses from Schilling *et al.* (1983) and their calculated equilibrium olivine compositions using the method of Roeder & Emslie (1970) and a Mg–Fe partition coefficient of 0.3. Binary mixing line is calculated for impregnation of depleted Bouvet FZ peridotite (Fo = 90:3) (Dick, 1989) with nickel-rich olivine (0.39 wt %) by a primitive central North Atlantic MORB (24% normative olivine, Mg-number 67, 265 ppm Ni). Olivine nickel content estimated by mass balance. Ticks represent 10% melt impregnation increments.

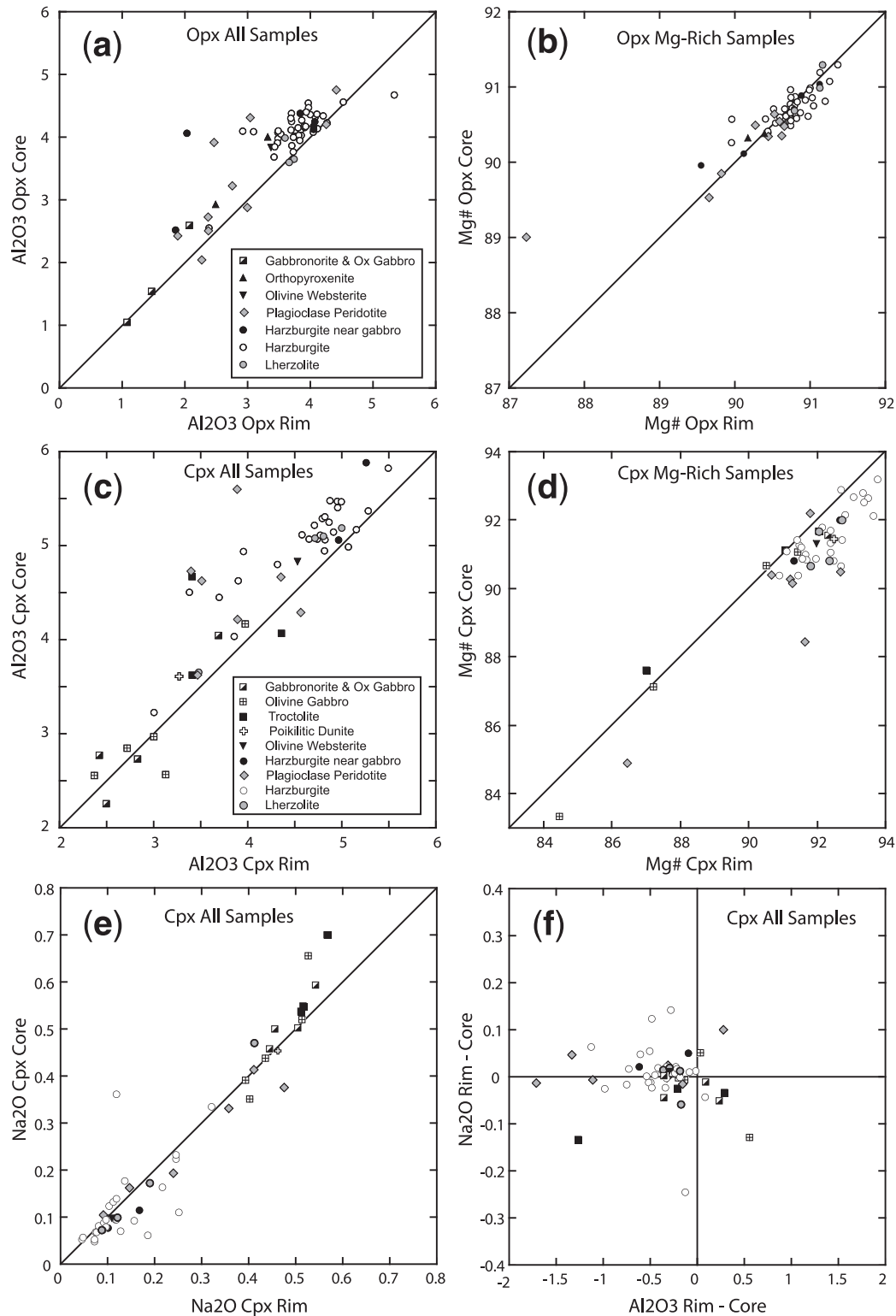


Fig. 13. Plots of core and rim compositions for Kane Megamullion pyroxenes. Each core and rim analyses consists of 10 contiguous 15 μm spots aligned perpendicular to exsolution lamellae, which were then averaged to estimate the initial bulk grain composition. (a, b) Orthopyroxene alumina and magnesium number; (c-e) clinopyroxene alumina, magnesium number, and sodium; (f) difference between rim and core sodium and alumina contents.

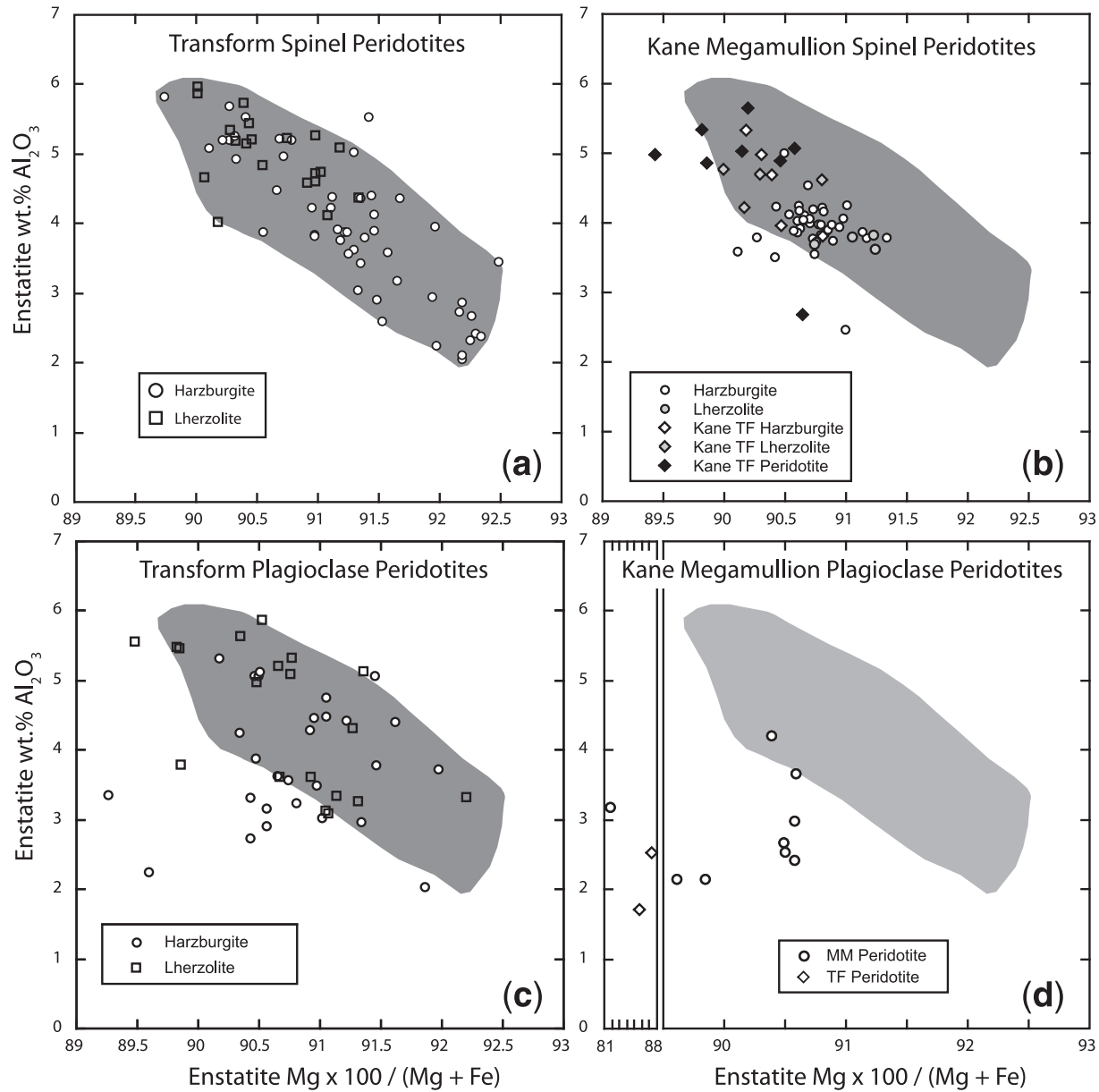


Fig. 14. Enstatite alumina content (wt %) vs Mg-number for spinel and plagioclase peridotite suites from 17 Indian and Atlantic Ocean transforms (a, c) compared with those from the Kane Megamullion (b, d).

Clinopyroxene

Cpx in the peridotites ranges from ~3 to 7 wt % alumina, and has Mg-number 89.0–93.8 (Fig. 15a), with two outliers at ~Mg-number 85. Spinel peridotite Cpx on average is more magnesian than in plagioclase peridotite, although there is considerable overlap in range. A weak correlation exists between decreasing modal Cpx and increasing Mg-number (Fig. 15a), consistent with variable extents of mantle melting. Excluding plagioclase peridotite, there is also a negative correlation of alumina with Mg-number and a weak one for chrome (Fig. 16b), even though chrome is more compatible than alumina. This probably

reflects coupled Al–Cr substitution, causing both to decrease with progressive melting. We note that the Cr content of the transform wall spinel peridotites falls off this correlation. This is matched by elevated titanium and sodium contents relative to residual spinel peridotites from the main core complex (Fig. 16c and d). This could be due to a transform edge effect causing melting to cease at higher pressure than beneath the ridge. This would, for example, favor retention of the jadeite molecule in pyroxene. Cpx titanium is uniformly low in the main core complex spinel peridotites (<0.2 wt %), consistent with its incompatibility and their depleted character. Although

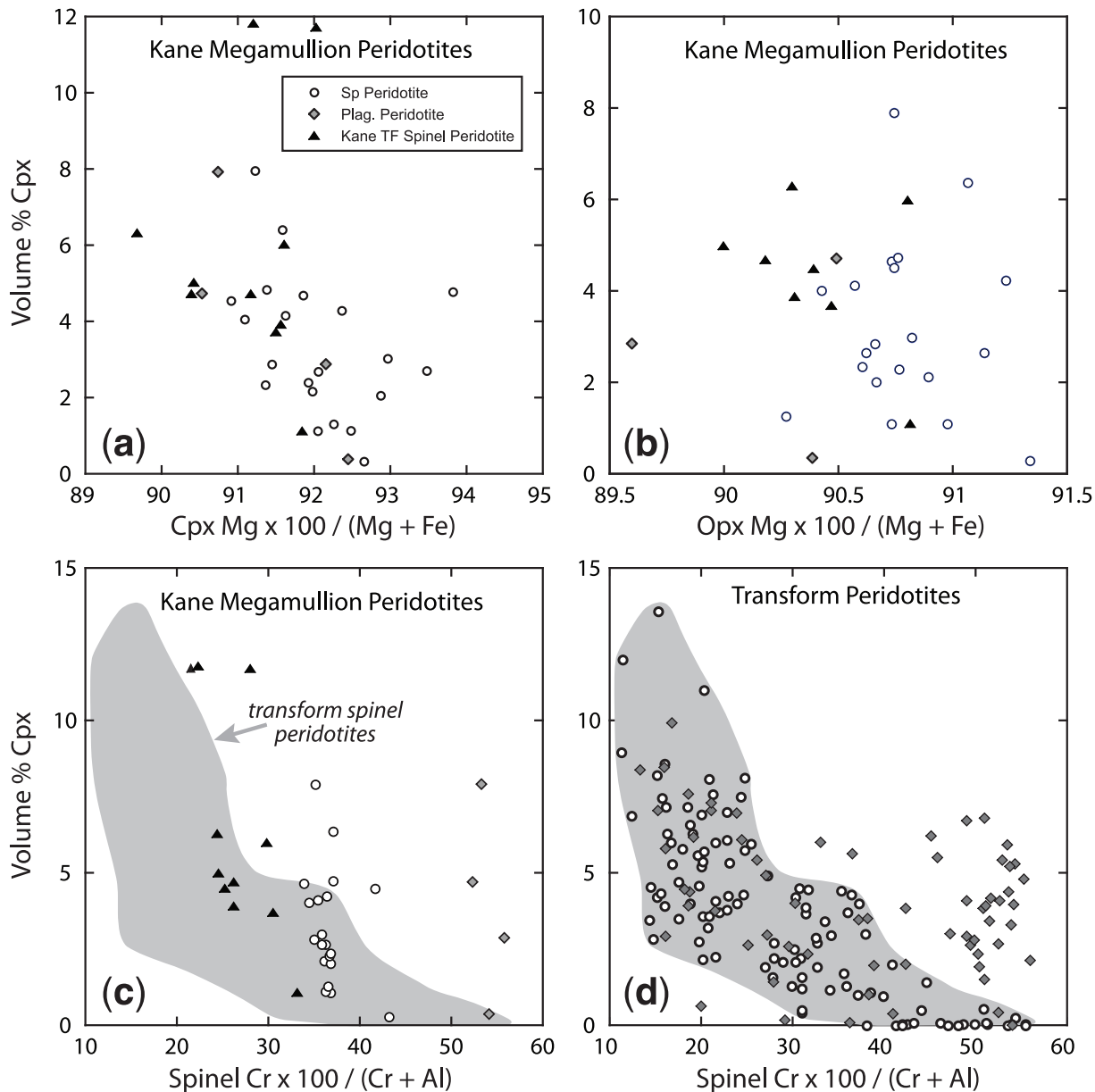


Fig. 15. (a) Modal clinopyroxene content vs Cpx Mg-number and (b) Opx Mg-number for Kane Megamullion peridotites. (c) Modal clinopyroxene content vs spinel Cr-number compared to the field for transform peridotites, and (d) modal clinopyroxene content vs spinel Cr-number for 17 Atlantic and Indian Ocean transform peridotite suites.

this is also generally true for sodium, 12 of 56 spinel peridotites show excess Cpx sodium up to 0.8 wt % (Fig. 16d). In contrast, plagioclase peridotite Cpx has consistently high sodium and titanium, generally greater than 0.15 wt %. However, sodium and titanium correlate poorly in both plagioclase and spinel peridotites. The alumina content of Cpx in plagioclase peridotite, as for enstatite, is significantly lower at given Mg-number than in spinel peridotite (Fig. 16b), despite their generally higher incompatible element concentrations.

Cpx is generally strongly zoned in the peridotites, with aluminous cores and magnesian rims, with the effect strongest in two plagioclase peridotites (Fig. 13c, d). Typically the rim has 0.5 wt % less alumina, and 0.7 mol % higher Mg-number than the core. Whereas the former might be understood as a function of decreasing solubility of Ca-Tschermaks molecule with decreasing pressure and temperature, it is more difficult to understand why diopside rims (and to a lesser extent enstatite) should have higher Mg-number than the cores. This could be due to

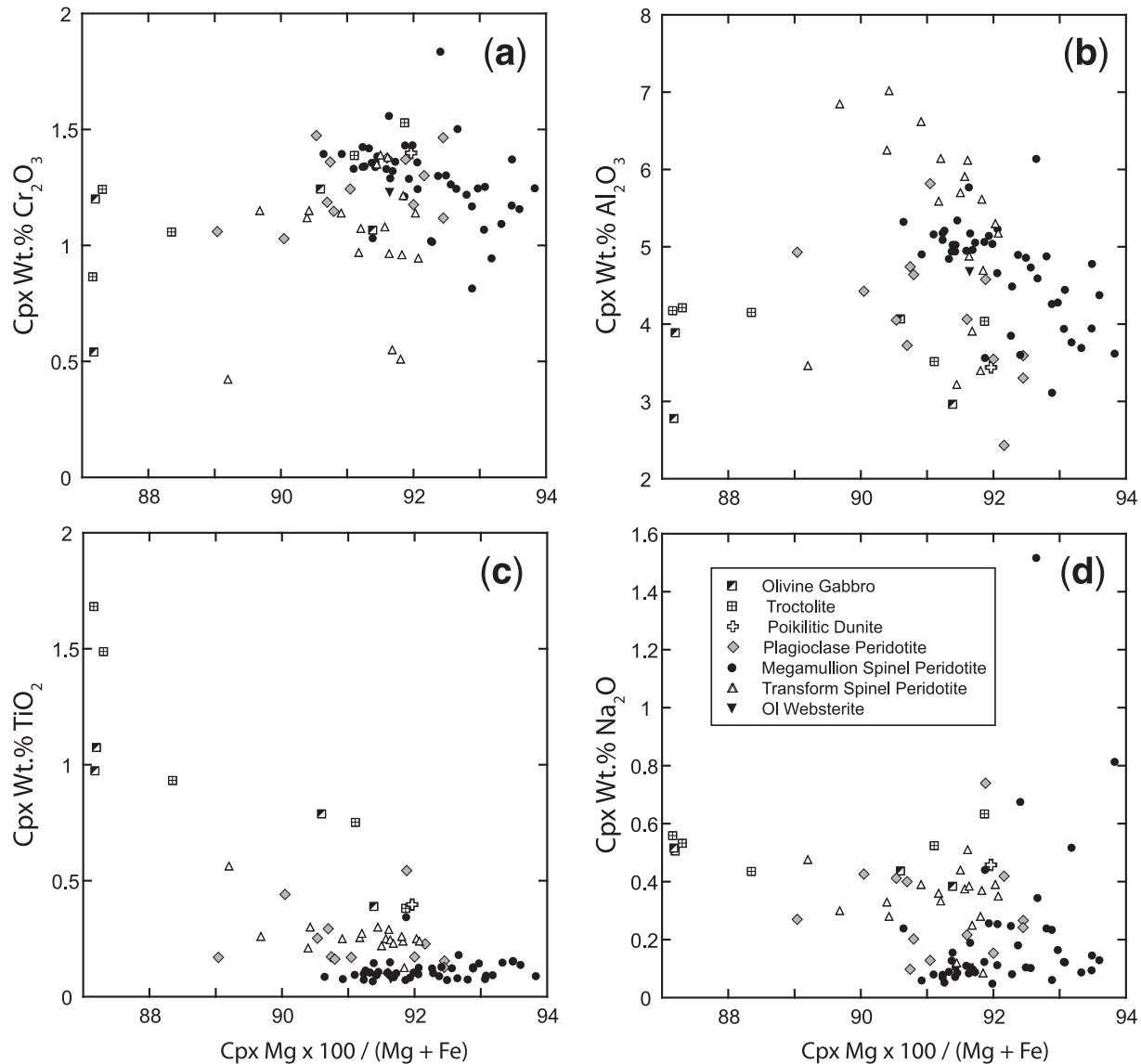


Fig. 16. Clinopyroxene Chrome (a), aluminium (b), titanium (c) and sodium (d) oxides vs Mg-number for the Kane Megamullion sample suite.

mechanical recrystallization during detachment faulting, causing spinel–olivine re-equilibration to unusually low temperatures where Fe partitions more strongly into spinel. Spinel in Fig. 17 is shifted to iron-rich compositions relative to the usual spinel trend for spinel peridotites: about 5 mol %, large compared with the Cpx shift. Typical spinel peridotites contain 0.25–0.5% spinel: not enough for re-equilibration to significantly affect the olivine composition, but enough to affect the small amount of diopside. Spinel often clusters with pyroxene, and thus mechanical recrystallization in a shear zone may produce zoning in Cpx where Fe–Mg diffusion is relatively slow, which is absent in olivine where diffusion is rapid (Gaetani & Watson, 2000). The reverse Cpx Mg–Fe

zoning may also be due to melt impregnation. Low Cpx alumina is strongly associated with melt-impregnated plagioclase peridotites. In this case, silica substituting for alumina in diopside may also cause chrome to decrease as a result of coupled substitution. Because the alumina would go into plagioclase, this would lead to more spinel richer in Cr, which would cause a greater loss of Fe than Mg, as both effects would lead to partitioning of more iron into the spinel.

Clinopyroxene compositions in the gabbroic veins, dunites, and related troctolites resemble those in the plagioclase peridotites, though extending to lower Mg-numbers and higher sodium and titanium (Mg-number 70–92, Na₂O 0.38–0.63 wt %, TiO₂ 0.19–1.7 wt %). They

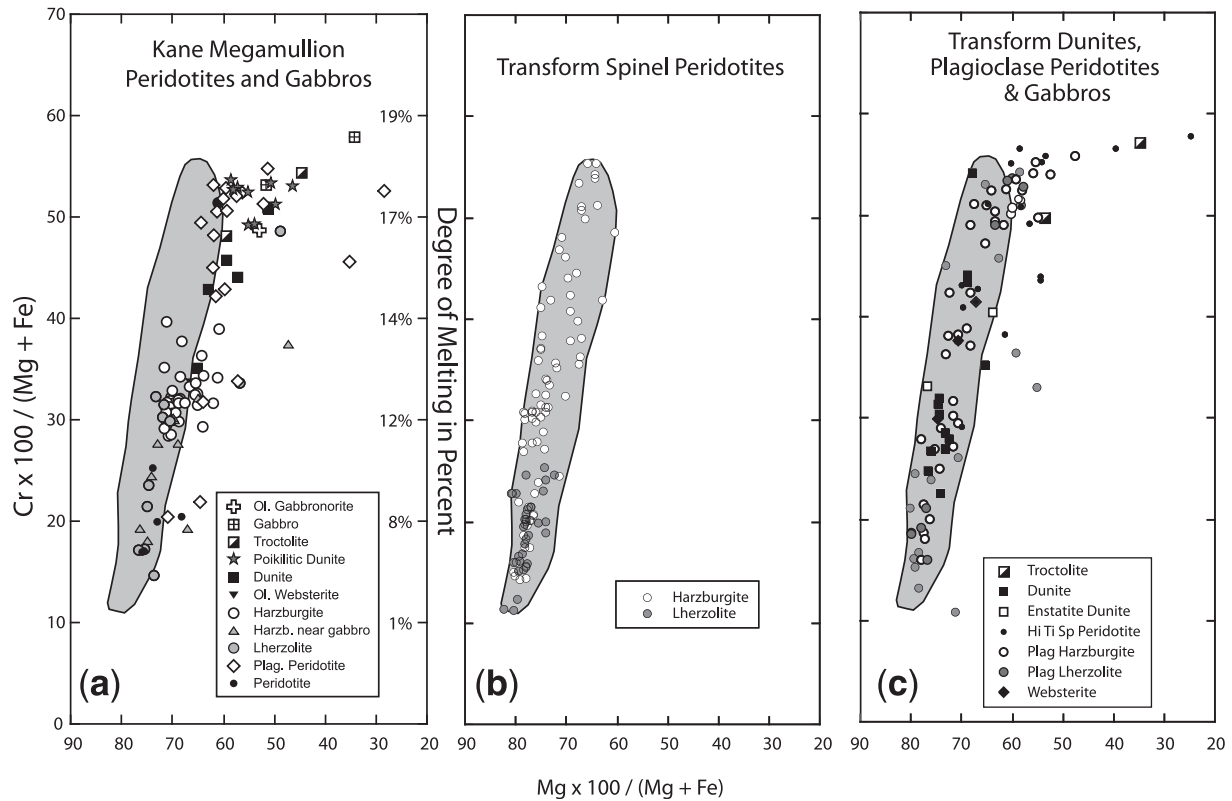


Fig. 17. Chromite–hercynite–spinel–magnesiochromite face of Steven's (1944) spinel compositional prism for the Kane Megamullion and Indian and Atlantic Ocean transform fault peridotite–dunite–gabbro suites. It should be noted that the y -axis (R^{3+} cations) is twice the length of the x -axis (R^{2+} cations) to keep the molecular proportions spatially correct in the projection. Grey field is for 17 Atlantic and Indian Ocean transform spinel peridotites.

span much of the range seen in MARK Hole 921 and Atlantis Bank Hole 735B (Fig. 18), although many have higher Mg-numbers, and fill the gap between oceanic gabbro complexes and mantle pyroxene (Table 4). More primitive varieties occur largely at Adam and Eve Domes, whereas more evolved varieties are characteristic of Cain and Abel Domes. Relict Cpx in poikilitic dunite Kn180-2-27-3 exhibits similar chemical characteristics to that in plagioclase peridotites, troctolites and olivine gabbros, with Mg-number of 92.0, substantial alumina depletion, and enrichment in Na_2O and TiO_2 relative to the spinel peridotites (Fig. 16).

Plagioclase

Relict plagioclase is preserved in one peridotite from the main core complex near a troctolitic vein. Its composition varies irregularly across a single grain from $\text{An}_{84.6}$ to $\text{An}_{98.3}$. Plagioclase analyzed in two transform peridotites by Ghose (1997) is considerably more sodic, varying from $\text{An}_{66.7}$ to $\text{An}_{77.1}$ in one sample, and from $\text{An}_{37.6}$ to $\text{An}_{57.2}$ in the other. This extreme variability suggests that the plagioclase is altered from its igneous composition.

Plagioclase in the troctolites, gabbros and poikilitic dunites generally overlaps the end of the trend for abyssal

gabbros, but extends to more calcic compositions (Fig. 18). In Adam and Eve Dome gabbros some plagioclase has anomalously high anorthite contents: possibly as a result of hydrothermal alteration. Plagioclase in the Cain Dome gabbro veins also lies well above the abyssal gabbro trend at relatively low Cpx Mg-number. Although this may reflect crystallization from a more refractory parent melt (e.g. Meyer *et al.*, 1989), the feldspar is turbid and filled with inclusions, suggesting that it is altered, consistent with the presence of abundant talc and amphibole. The two Abel Dome gabbro veins lie on the abyssal gabbro trend at relatively low anorthite and Cpx Mg-number, whereas one olivine gabbro vein lies off the trend at anomalously low anorthite. Thus, whereas the bulk of the dunite, troctolite and gabbro data extends the abyssal gabbro trend to more primitive compositions, the broad scatter in the data in Fig. 18 probably reflects hydrothermal alteration at widely varying P – T and fluid compositions, consistent with the often intense and highly varied alteration assemblages.

Spinel

Cr-spinel in the peridotites extends across nearly the full abyssal range for Cr-number [$\text{Cr}/(\text{Cr} + \text{Al})$] from a low

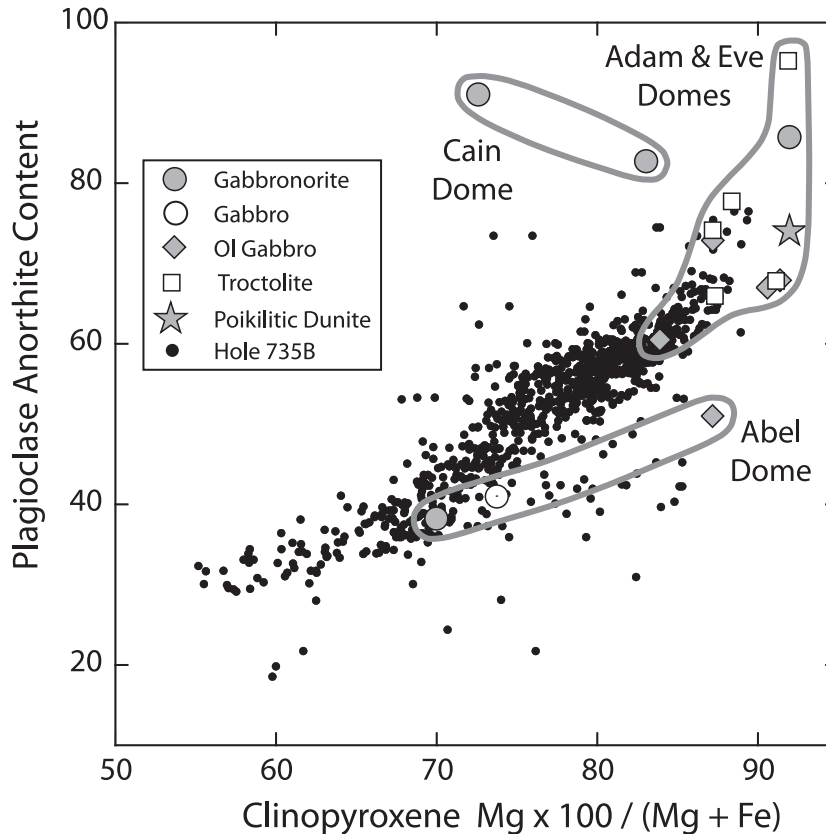


Fig. 18. Plagioclase anorthite content vs clinopyroxene Mg-number for Kane Megamullion gabbros, including Cain Dome Dive 113 and Abel Dome Dredge 19 mantle veins, and Adam Dome Dredges 27 and 28 and Eve Dome Dredge 21 transition zone gabbros. Plotted for comparison are the compositions of plagioclase and clinopyroxene from Hole 735B at Atlantis Bank on the SWIR from Dick *et al.* (2002). The Hole 735B and MARK Site 921 gabbros are chemically and petrographically similar, but the database for the former site is much larger.

of 14.7 in a transform wall lherzolite to a high of 51.5 in a Cain Dome harzburgite. This forms an array in a $\text{Mg}/(\text{Mg} + \text{Fe})\text{-Cr}/(\text{Cr} + \text{Al})$ diagram parallel to that for the transform peridotites (Fig. 17). Although the two arrays overlap, with most Kane spinels lying within the transform field, overall, the Kane array is systematically offset toward more iron-rich compositions (Fig. 17). The large variation in residual abyssal peridotite spinel Cr-number is generally interpreted as reflecting variations in bulk peridotite composition, reflecting mantle melting that progressively depleted relatively incompatible aluminium and enriched relatively compatible chromium. Cpx preferentially contributes to the melt during mantle melting, and, consistent with this, spinel Cr-number crudely increases with decreasing modal Cpx (Fig. 15c and d). Based on the correlation of spinel Cr-number to Cpx heavy rare earth element (HREE) abundances, Hellebrand *et al.* (2001) demonstrated that the range of melting for abyssal peridotites extends from $\sim 2\%$ to $\sim 18\%$, assuming a uniform mantle source composition. The tight abyssal spinel trend (e.g. Fig. 17b) reflects equilibration of chrome spinel with

the limited olivine variation produced over a large range in melting ($\sim \text{Fo } 89.5\text{--}91.5$ for the 17 transform suites in Fig. 17b). Increasing spinel Mg-number along this trend is mostly due to the effect of Cr on Fe–Mg partitioning between olivine and spinel, such that Cr-rich spinel is more Fe-rich than Al-rich spinel in equilibrium with the same olivine composition (Irvine, 1965, 1967).

A shift in spinel composition to the right in Fig. 19 can be due either to equilibrium with more iron-rich olivine or to equilibration to lower temperature (Irvine, 1965, 1967). The tight Mg-number–Cr-number transform peridotite trend in Fig. 17b therefore must reflect a uniform equilibration closure temperature. The systematic shift and spread of the Kane spinels in Fig. 17a, however, does not reflect more iron-rich olivine as forsterite contents are typical of abyssal peridotites, and there is no systematic difference in olivine or enstatite Mg-number for most spinel peridotites plotting to the right of the transform array (Fig. 19). Plagioclase peridotites and spinel peridotites that re-equilibrated with adjacent gabbro veins are exceptions. Noting the tendency of mylonites to plot to the right of the

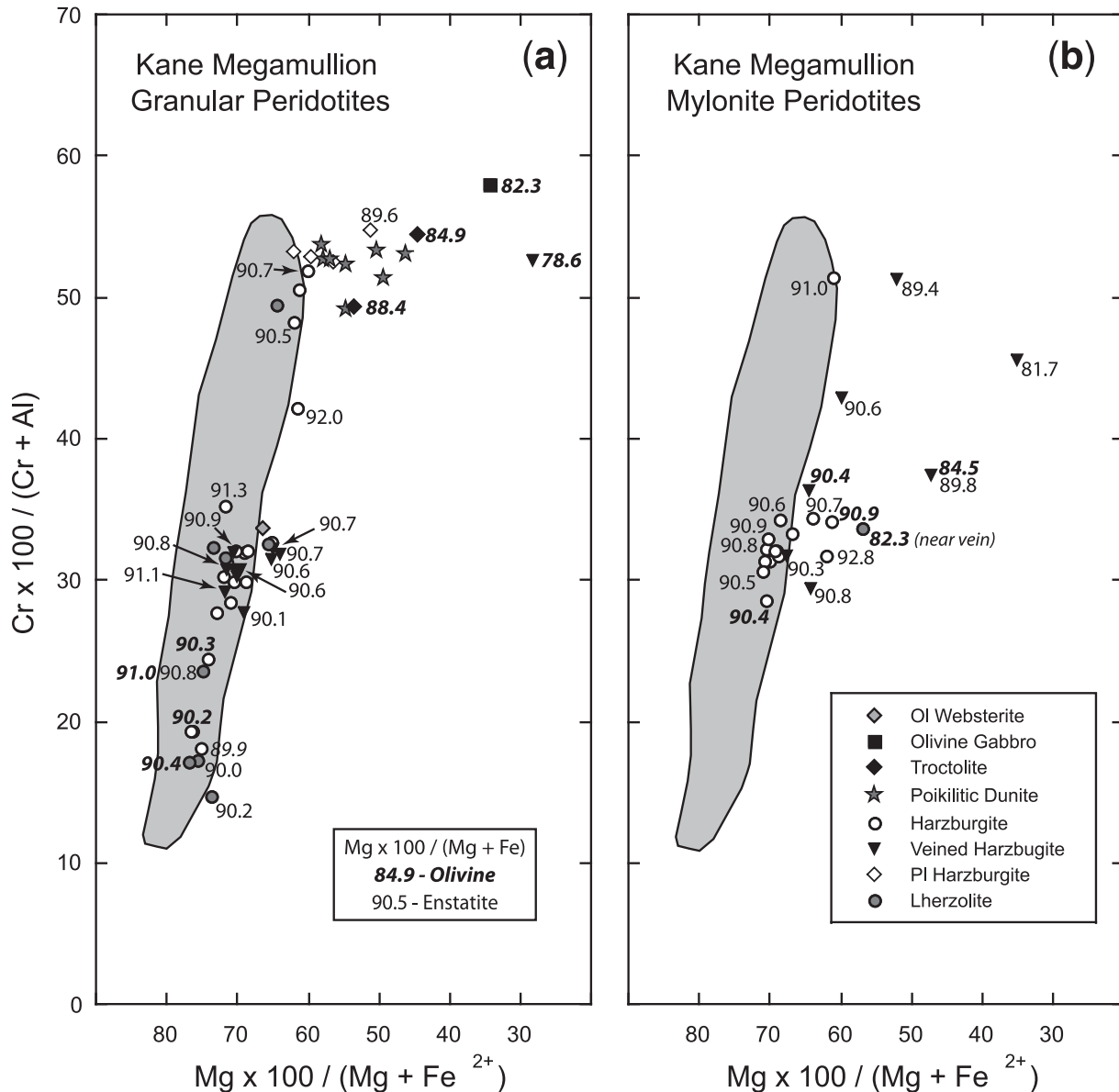


Fig. 19. Kane Megamullion chromian spinel compositions plotted separately for granular (a) and mylonitic (b) peridotite sub-types to illustrate the influence of deformation on spinel composition as well as highlighting the influence of spinel equilibrium with iron-rich olivine in the dunites, troctolites and plagioclase peridotites. Spinel analyses annotated with Mg-number of coexisting enstatite and olivine (italics).

transform array (Fig. 19b), we suggest that the shift to more iron-rich spinel compositions is in part due to re-equilibration to lower temperatures as a result of mechanically induced recrystallization, consistent with the large number of Kane samples from or close to the detachment fault zone. Re-equilibration, however, has in theory only a small effect on spinel Cr-number (Irvine, 1965, 1967). Thus, the primary factor determining spinel Cr-number is peridotite bulk composition, and therefore often interpreted as the extent of mantle melting.

The spread of a large data population in an x - y plot can be deceptive and it is useful to look at the variation in

Cr-number in simple histogram plots where population densities are clearer and outliers less important (Fig. 20). For the transform data the spinel peridotites are heavily skewed with a major peak at \sim Cr-number 22 with a very short tail ending at Cr-number 11. This peak corresponds to \sim 9% melting for the Hellebrand *et al.* (2001) model, consistent with the sample bias to the ultraslow-spreading SW Indian and American–Antarctic Ridges and a strong transform edge effect where mantle melting is believed to be inhibited by conductive heat loss caused by the slow mantle upwelling and the influence of the adjoining old cold plate (Reid & Jackson, 1981; White *et al.*, 1992).

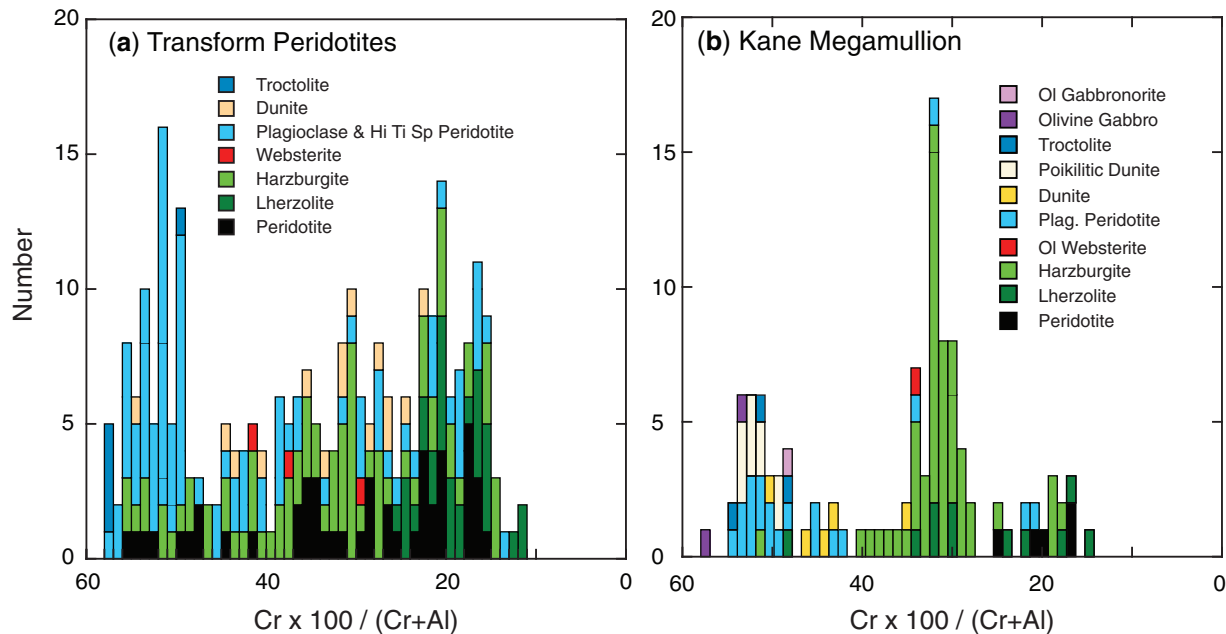


Fig. 20. (a) Histogram of spinel Cr-number for 17 Atlantic and Indian Ocean transform suites, and (b) for Kane Megamullion peridotite–dunite–gabbro suites.

Plagioclase peridotites, however are strongly skewed to a different peak at ~ 53 . Chromian spinel in textural equilibrium with MORB has a similar peak distribution (Sigurdsson & Schilling, 1976; Dick & Bryan, 1978), consistent with the concept that the plagioclase-peridotites have partially equilibrated with MORB (e.g. Dick & Bullen, 1984; Tartarotti *et al.*, 2002). The distribution of the Kane spinel peridotites is different, with a major peak at Cr-number 32 corresponding to the main core complex, and a second minor peak at Cr-number 20 corresponding to the transform wall. Notably, the Kane plagioclase peridotites have the same Cr-number peak as those in the transform suite, consistent with their spinel composition also being related to that of MORB.

Dunites in the transform suite have a broad range of spinel compositions, with most lying at intermediate Cr-number (Fig. 20a). The transform suite does not include poikilitic dunites, and troctolites are rare. Transform dunites also typically crosscut peridotite and do not have a strong association with gabbro; they are largely interpreted as melt transport channels in which MORB aggregates (e.g. Dick & Natland, 1994, 1996; Kelemen *et al.*, 1995). The relatively high spinel alumina content is probably due to a bias towards melts in the channels that were not yet fully aggregated MORB, as progressive melting would add the most Cr-rich fractional melt increments at the top of the melting column. By contrast, Kane dunite spinels are relatively Cr-rich, and plot significantly to the right of the transform spinel peridotite array in Fig. 17, together with those in the gabbros and

troctolites. These rocks all crystallized from or partially equilibrated with a basaltic melt, and thus define an Fe–Mg fractionation trend extending to the right in Fig. 17 consistent with decreasing forsterite content, and coexisting plagioclase and Cpx compositions (Fig. 18) reflecting crystallization from an aggregate MORB in the lower crust possibly at its base.

The strongest indicator of the influence of a MORB-like liquid on peridotite and related rocks is high spinel TiO_2 , which is generally uniformly very low in residual peridotites ($<0.15\%$). This is consistent with its incompatibility, and the extreme depletion of the peridotites. By contrast, spinel in plagioclase peridotites and dunites is generally enriched in TiO_2 , inconsistent with a simple residual origin (Dick & Bullen, 1984). Hence, peridotites with $>0.15\%$ spinel TiO_2 typically have a hybrid origin; usually involving impregnation or cryptic metasomatism by trapped or transient MORB-like melts. Notably, the entire Kane spinel population above Cr-number 40 has elevated TiO_2 , and these samples were all arguably affected by interaction with MORB-like melts (Fig. 21).

DISCUSSION

What do abyssal peridotites represent?

Abyssal peridotites are tectonically emplaced to the seafloor at the base of rift valley walls and ridge–transform intersections and then uplifted into rift-mountains and onto transform walls. These rocks represent the very top of the sub-axial mantle-melting column and the residue of

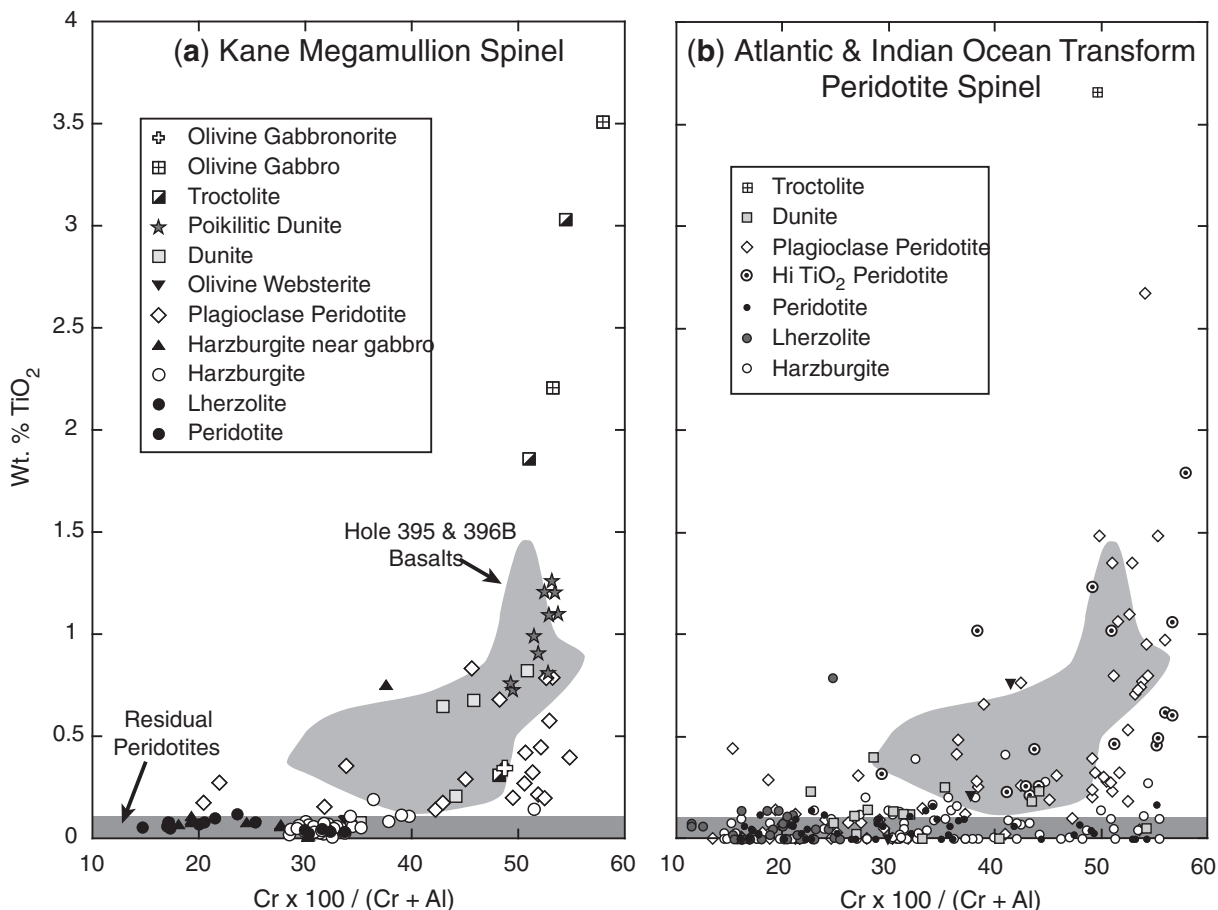


Fig. 21. Plots of wt % TiO₂ vs Cr-number in spinel from (a) Kane Megamullion and (b) 17 Atlantic and Indian Ocean peridotite–dunite–gabbro suites. Shaded Field for Hole 395 and 396B basalt spinels cored in the MAR rift mountains to the east and west of the MAR at 24°N shown for comparison (Dick & Bryan, 1978; Graham *et al.*, 1979). Grey band at the bottom of the plot highlights residual peridotites with <0.15 wt % TiO₂.

the highest degree of melting beneath a ridge. Secondary faults, such as the outward-facing West Fault, and transform-parallel high-angle normal faults may cut deeper into the section, but rarely more than a few hundred meters (e.g. Francheteau *et al.*, 1976). Peridotites can be sampled in the head walls of large landslips beneath the fault damage zones, but rarely more than several hundred meters. Most abyssal peridotite samples are from debris flows and talus ramps where key stratigraphic relations are not preserved. Abyssal peridotites in general, therefore, do not allow investigation of vertical composition gradients, even on the kilometer scale, as in ophiolites (e.g. Suen *et al.*, 1979; Girardeau & Nicolas, 1981; Lippard *et al.*, 1986; Suhr & Batanova, 1998; Godard *et al.*, 2000; Takazawa *et al.*, 2003). They also cannot yield the average degree of mantle depletion, which must be integrated over the full three-dimensional mantle-melting column, and is probably much less than would be inferred from our samples (e.g. Asimow & Langmuir, 2003). Rather, our data address the baseline upper limit of melting, and lateral

variations caused by focused melt transport through the mantle.

Mantle modal variations and melt production beneath ridges

Dick *et al.* (1984) found systematic correlations between basalt composition and peridotite mineral modes and mineral compositions from the Atlantic and Indian Oceans and the Caribbean Sea indicating increasing degrees of mantle depletion near hotspots. When re-expressed with basalt Na₂ as a variable, the correlation is essentially the same (Niu *et al.*, 1997). Unlike Klein & Langmuir (1987), Dick *et al.* (1984) did not postulate a correlation with crustal thickness, as the variations in basalt and peridotite chemistry can be due to variable initial mantle composition as much as melt production, consistent with a recent reconsideration of the global correlation of MORB and ridge depth by Niu & O’Hara (2008). The Dick *et al.* (1984) correlations are also evident only for peridotites averaged by dredge and locality. Similarly, correlations

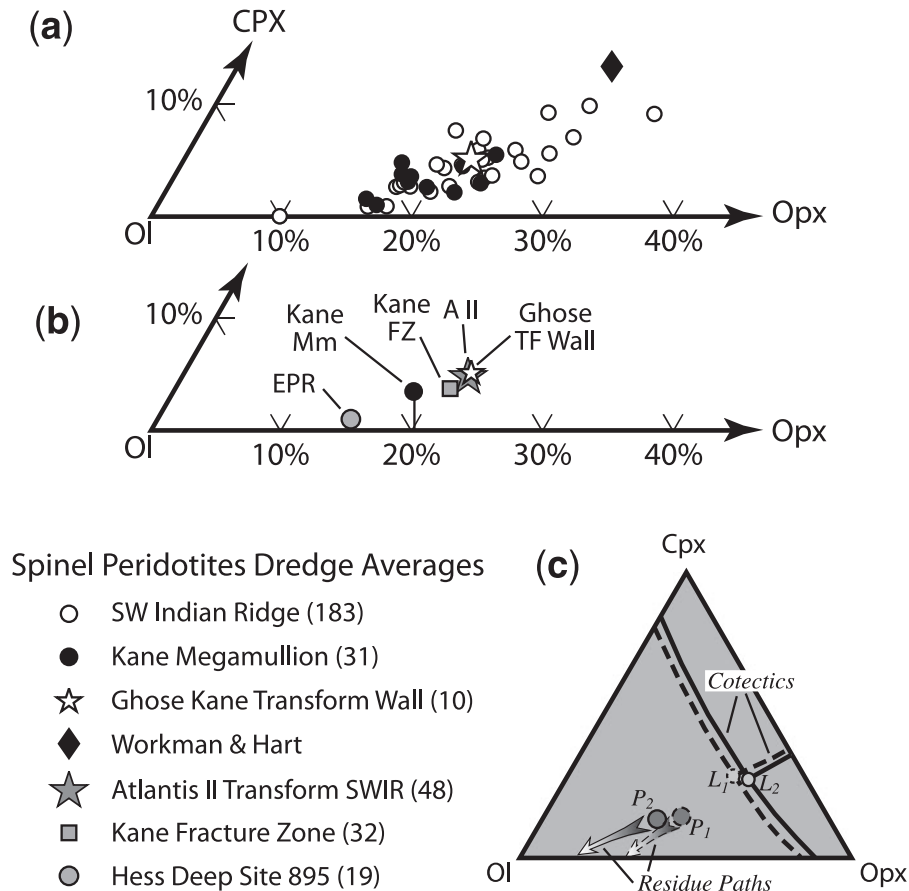


Fig. 22. (a) SWIR and Kane Megamullion peridotite mineral modes averaged by dredge or station in the olivine corner of the Ol–Opx–Cpx ternary. All *Nautila* dive samples from the transform wall flanking the megamullion from Ghose (1997) are averaged together. Diamond shows the hypothetical composition of DMM from Workman & Hart (2004). (b) Average modal peridotite compositions for Hess Deep Site 895 EPR (Dick & Natland, 1996), Kane Megamullion (not including transform wall), Kane Fracture Zone (including data for 22 additional older fracture zone samples), the Atlantis II Transform on the SWIR, and for the Ghose (1997) data for the transform wall flanking the Kane Megamullion. (c) Hypothetical melting paths for two different parent compositions and corresponding residual melting paths. Number of samples in averages given in parentheses in legend.

between peridotite mineral mode and mineral composition for single dredges or dives are weak at best, which is also true for the Kane Megamullion peridotites. Thus, outcrop- and local-scale mineral and modal variability reflects factors other than simple variation in degree of melting, such as metamorphic differentiation during melting, variable melt channeling, melt–rock reaction, cryptic metasomatism, and impregnation by trapped or transient melts. Dredge and dive averages, however, show that peridotites from the main core complex are more depleted than those from the flanking transform wall. This is probably due to variations in extent of melting in response to the transform edge effect, rather than in initial mantle composition. We note that Dick *et al.* (1984) mostly compared transform peridotites with zero-age basalts from the adjacent ridge, otherwise the differences between sub-axial and transform peridotites, as at Kane, would probably have obscured their correlation.

The Kane Megamullion and SWIR modal ternary trends are indistinguishable (Fig. 22a), projecting directly towards average Hess Deep, East Pacific Rise (EPR) peridotite (Fig. 22b). This argues for melting of similar or related mantle source compositions (e.g. Fig. 22c). The degree of peridotite depletion, however, integrates the entire melting history, and not just that of the last ridge event, and thus the modern mantle source may vary in fertility along or between ridges. The trends project to lower modal Cpx than the hypothetical average depleted mantle of Workman & Hart (2004), however, which may indicate greater global source variability than inferred from the Kane and SWIR peridotites.

In this light, we note that the average composition of the Kane FZ peridotites is slightly more depleted than for the Atlantis II FZ (Fig. 22b), despite the fact that the Atlantis Bank Core Complex at the latter exposes a >700 km² gabbro massif that is at least 1.5 km thick (Dick *et al.*,

2000), whereas gabbroic layer 3 is missing over significant portions of the Kane Megamullion (Dick *et al.*, 2008). This indicates that despite the slower SWIR spreading rate and longer Atlantis II Transform, which should result in lower melt production, more melt and thicker crust was produced at the paleo-SWIR. This is also opposite to crustal thickness predicted from Na_8 in spatially associated basalts of $\sim 4\text{--}5$ km for the MAR at 23°N ($\text{Na}_8 \sim 2.67\text{--}2.93$; Reynolds & Langmuir, 1997) and ~ 3 km for the SWIR at 57°E ($\text{Na}_8 \sim 3.2\text{--}3.3$; Robinson *et al.*, 2001). The best explanation for this is that the parent mantle composition at the SWIR was more fertile than beneath the MAR. This seriously undermines the essential premise of a relatively uniform parent mantle composition for predicting crustal thickness by simple inversion of MORB compositions along ocean ridges.

Uniform mantle melting and the transform edge effect

There is a systematic difference between the average peridotite from the flanking transform wall and sub-axial peridotites from the main Kane core complex. This includes lower olivine and pyroxene Mg-number, higher modal Cpx, and more aluminous pyroxene and spinel. All this is consistent with conductive cooling terminating mantle melting deeper near the transform as a result of the influence of the old cold lithospheric plate on the upwelling mantle (Detrick & Purdy, 1980; Detrick *et al.*, 1993). This is best shown by the regional variation in Cr-spinel composition across the Kane Megamullion (Fig. 23). There is a strong bimodality, with residual low-Ti spinel peridotites clustering at the low Cr-number end of the spinel array, defining a baseline for mantle melting across the region. More Ti-rich spinels, showing the influence of a MORB-like melt, spread upwards above this baseline and are capped between Cr-number 50 and 60, consistent with the upper limit of Cr-spinel for primitive MORB. Thus the largest spread in spinel compositions is where the baseline is lowest, and smallest where it is highest.

The Kanaut samples (Auzende *et al.*, 1992, 1994) flank the length of the Kane Megamullion (Fig. 2), corresponding to 1.2 Myr of accretion; and are likely representative of the transform domain. The main core complex sample is also representative, although of a larger region. Projecting the data along a north–south line, the baseline shows a pronounced edge effect within 10 km of the transform (Fig. 23a). Previous studies, using widely spaced samples along the MAR, extended the transform edge effect southward as far as the $22^\circ 10'\text{N}$ MAR axial discontinuity—a distance of ~ 160 km (Ghose *et al.*, 1996). However, our data show that mantle depletion decreases south of the $23^\circ 15'\text{N}$ axial discontinuity. It now seems that, except for the transform wall, the earlier studies were looking at a regional gradient in mantle composition and/or melting rather than the transform edge effect.

The magnitude of the transform edge effect is probably smaller than previously inferred. Hellebrand *et al.* (2001) found the minimum difference in melting to be 10% using the most fertile and depleted peridotites, an assumed pyroxene source composition, and calibrating changes in spinel Cr-number to models for evolving Cpx HREE concentrations. However, this probably overestimates the effect, as at outcrop scale the apparent degree of melting depends on the extent to which adiabatically decompressing melt is focused to one area or another, whereas a fertile peridotite can represent pooling of trapped late melt. To this is added any initial mantle heterogeneity. In the final analysis, every mantle peridotite is a hybrid that started with an initial composition that depended on earlier mantle melting and hybridization events. It rose through the mantle undergoing adiabatic melting and experiencing a variable melt flux passing through it depending on its position in the mantle-melting column. On reaching the lithosphere, where melt mass decreases, it may be in a zone of melt transport, and undergo extensive melt–rock reaction, and stripping of pyroxene or be in an area where melt is trapped. In estimating the regional variation in melting, what is sought is the difference arising from changes in thermal structure and mantle composition. Thus, it is the average residual peridotite composition that best reflects this. Screening to eliminate peridotites with spinel $\text{TiO}_2 > 0.15$ wt %, we find an average Cr-number of 31.7 for 46 residual spinel peridotites from the main core complex and a Cr-number of 20.2 for 16 spinel peridotites from the transform wall, corresponding to a difference of 4.5% melting (12.5% for the main core complex versus 8% for the transform wall).

Excluding the transform, there is a very uniform degree of melting, as average Cr-number along the baseline varies between 28 and 35, corresponding to 11.3–13.8% melting, which also implies a fairly uniform source composition (Fig. 23b). Although this contrasts to the 5–14.5% variation found over 20 Myr along the Vema FZ (Bonatti *et al.*, 2003), over a 3 Myr interval the Vema data show periods of similar uniformity.

Can spreading rate be determined from mantle petrography?

It has long been maintained that ophiolites with harzburgitic mantle sections represent fast-spreading environments, whereas those that are lherzolithic represent slow-spreading environments (Boudier & Nicolas, 1985; Nicolas, 1986, 1989). Such a simple classification scheme is questionable for many ophiolites with complex parageneses such as the Trinity ophiolite where the overlying cumulates and underlying mantle peridotites are not petrogenetically related (see Ceuleneer & Le Sueur, 2008). It is also questionable as abundant harzburgite is found at slow-spreading ridge transforms, where the ocean crust and shallow mantle are related (Dick, 1989). In fact, the most depleted abyssal peridotites are from the MAR from 2°N

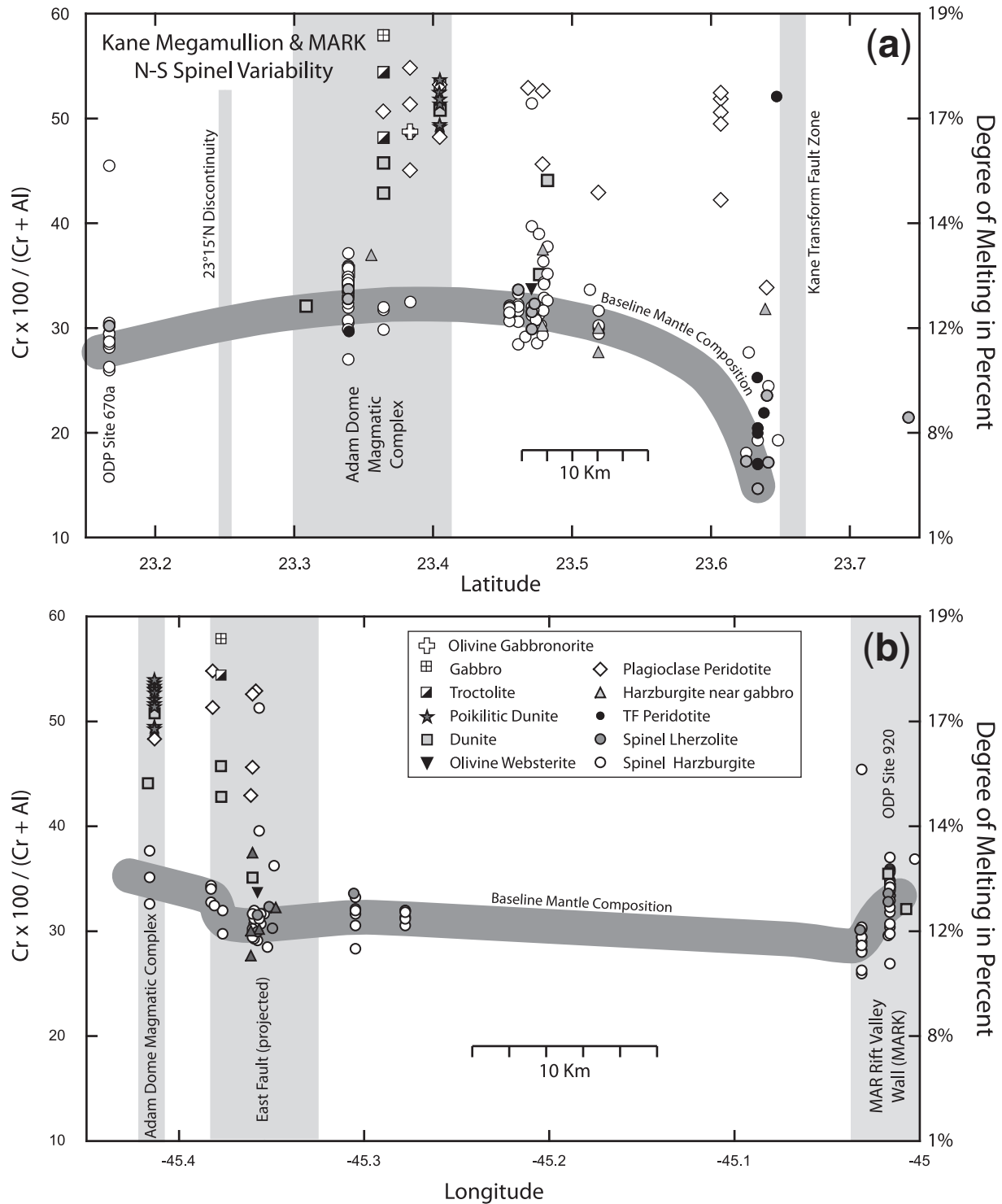


Fig. 23. Latitudinal (a) and longitudinal (b) plots showing the composition of spinels in the MARK and Kane Megamullion peridotite-dunite-gabbro suites. Data for Kane Megamullion from this paper and from Ghose (1997). Data for ODP Hole 920 from the ODP Leg 153 Scientific Results Volume (Burgath *et al.*, 1997; Kempton *et al.*, 1997; Niida, 1997; Ross & Elthon, 1997) and data for Hole 670A from Komor *et al.* (1990). Longitudinal plot excludes data from south of the 23°15'N discontinuity and from the transform wall to look at variations only within the MARK paleo-ridge segment. Wide grey curve indicates an eyeball fit of the baseline for mantle melting to the average composition of residual spinel peridotites. Degree of melting calculated using the formulation of Hellebrand *et al.* (2001) for melting of a pyrolytic mantle.

to 3°N and 14°N and 15°N (Bonatti *et al.*, 1992; Godard *et al.*, 2008) situated well away from any known hotspot. Whereas Hess Deep, EPR spinel peridotites typically have only ~1% Cpx (Dick & Natland, 1996), transform fault peridotites near hotspots at slow- and ultraslow-spreading ridges are equally depleted (Dick *et al.*, 1984). Now, as a result of the transform edge effect, it also appears that fracture zone peridotites provide an underestimate of the degree of melting at slow-spreading ridges. MARK itself is the iconic end-member for N-MORB (Bryan *et al.*, 1981), a bathymetric low point for the ridge, and represents a well-defined minimum for the extent of mantle melting on the MAR from 0° to 70°N (Casey, 1997). The low Cpx content of the sub-axial mantle at the Kane Megamullion thus suggests that much of the MAR mantle must be close to Cpx free. Consequently, the classification of ophiolites into slow and fast spreading based on mantle petrology alone must be regarded as generally invalid; some ophiolites so attributed to fast- or slow-spreading ridge environments are probably misclassified.

Abysal peridotites and the uniform major element composition of MORB

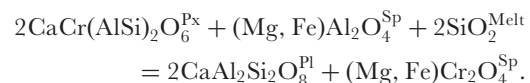
Whereas much attention is focused on the seemingly large local and regional trace element variability, the major element composition of MORB is remarkably uniform with a smaller variance today than when this was first famously observed by Engel and coworkers (Engel & Engel, 1964a, 1964b; Engel *et al.*, 1965). Dick & Fisher (1984) showed that diopside-out limits melting of abyssal peridotites; if most abyssal mantle has melted close to this point, which the Kane data suggest, this can explain the major element uniformity. In near-fractional melting (e.g. Johnson & Dick, 1992), where melt coalesces and migrates out of the mantle faster than the mantle upwells, the major element composition integrates contributions from the entire melting column. The opposite is true for incompatible trace elements, which are generally stripped from the mantle at the base of the column, and effectively diluted by melt contributions only higher up. Thus, a melt's trace element composition is largely determined by heterogeneities entering the base of the column. With a relatively constant end-point for melting, however, except at the very slowest spreading rates (see Standish *et al.*, 2008), parent MORB major element composition largely varies with mantle bulk composition along a ridge, whereas regional gradients in mantle isotopic and trace element composition are best seen when MORB is locally averaged to eliminate the signal of local mantle heterogeneity.

Plagioclase peridotites—evidence for trapped MORB melt in the shallow mantle

Plagioclase, stable in peridotite at pressures less than 8 kbar (Green & Hibberson, 1970), is a common accessory

mineral in abyssal peridotite. Plagioclase peridotite pyroxene geobarometry for the 870 km offset Romanche Transform indicates pressures equivalent to 3–4 kbar (Tartarotti *et al.*, 2002), but it is likely that south of the smaller Kane Transform offset, plagioclase might represent shallower crystallization depths. There are several possible origins: exsolution from pyroxene, reaction of enstatite, diopside and spinel to form olivine plus plagioclase (Hamlyn & Bonatti, 1980) and crystallization from trapped melt (Church & Stevens, 1971; Menzies, 1973; Menzies & Allen, 1974; Quick, 1981a, 1981b; Dick & Bullen, 1984). There is a consensus, however, based on its distinctive mineral chemistry and texture, that most plagioclase represents impregnation by trapped or transient MORB-like melts (Bonatti, 1992; Cannat *et al.*, 1992; Cannat & Casey, 1995; Dick, 1989; Girardeau & Mercier, 1992; Hékinian *et al.*, 1993; Tartarotti *et al.*, 1995b, 2002; Rampone *et al.*, 1997). In our sample suite, we believe most plagioclase has this origin.

Whereas plagioclase typically occurs in very small amounts <2% (Fig. 8), most studies focus on exceptional cases, such as the Romanche FZ, where large amounts of plagioclase (up to 18%) occur. Kane Megamullion peridotites are more typical, with small volumes of plagioclase locally abundant at the Adam and Eve Magmatic Center and a few other sites. This provides evidence for local-scale migration of MORB-like melts through the shallow mantle. At Kane Megamullion the chemical effects are variable, but often large; for example, the shift in spinel composition to high Cr-number and coexisting pyroxene to lower alumina, and higher silica, titanium, and sodium. This probably represents the reaction



Alumina loss as a result of solid-state re-equilibration to lower pressures and temperatures, by contrast, should be accompanied by a decrease in sodium and titanium, opposite to what we observed and to what has been observed also in other melt-impregnated plagioclase peridotites (e.g. Kaczmarek & Müntener, 2008). There is no simple correlation, however, between mineral chemistry and plagioclase volume, indicating that chemical effects depend on total melt flux through the peridotite or proximity to a gabbro vein, as much as per cent trapped melt. The opposite occurs in the Romanche peridotites, where chemistry can correlate with plagioclase volume (Dick & Bullen, 1984).

In general, plagioclase peridotites tend to have iron-rich olivine and pyroxene compared with spinel peridotites (Figs 11–16). Although some of this variation can be attributed to equilibration with trapped MORB-like melt, with <2% plagioclase in the rock, this cannot account for Fo_{78-6} olivine. The normative plagioclase to mafic silicate

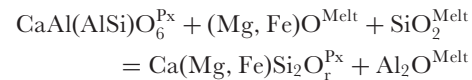
ratio varies little in MORB, and generally lies between 55 and 60. Thus 1–2% plagioclase corresponds to ~2–3% trapped melt. As seen in Fig. 12, linear addition of a primitive MORB to a residual peridotite implausibly requires equilibration with up to 75% melt to reach the olivine composition in some plagioclase peridotites. The alternative requires reaction of a large volume of transient melt with vanishingly small amounts of plagioclase precipitation, while reaching low olivine forsterite content without equilibrating it to low Ni contents (Fig. 12). In this case a high olivine nickel content could be a chromatographic effect caused by the contrasting nickel and iron partition coefficients (~7–11 vs ~1; Hart & Davis, 1978), with nickel abundance lagging Mg-number (e.g. Navon & Stolper, 1987). Most low-Mg olivine in the Kane peridotites, however, occurs within 2 cm of visible gabbroic veins, and re-equilibration with MORB intruded along such veins probably accounts for the high-Ni olivine to the left of the main mantle array in Fig. 12.

Mantle metasomatism (melt and fluid)

Late-stage melt–rock interaction in the lithosphere includes reaction with partially or fully aggregated MORB and ambient melts representing the last small increments of melting in an open-system quasi-fractional melting environment. Whereas the influence of the former is relatively easy to detect because of the contrast in composition between depleted mantle peridotite and MORB, together with crystallization of interstitial plagioclase, the influence of the latter is more difficult to identify. A vanishingly small melt increment produced at the top of the melting column, back crystallized with the peridotite from which it was generated, is effectively undetectable. Other fractional melt increments, however, will have migrated into the shallow mantle and may produce detectable signals; for instance, the late interstitial clinopyroxene identified by Seyler *et al.* (2001) in some eastern SWIR peridotites.

Pyroxenes in the Kane spinel peridotites are often zoned with rims variably depleted in alumina (Fig. 13a and c). This is commonly observed in other mantle suites and generally attributed to re-equilibration following emplacement from depth, with the loss of Ca-Tschermak's or jadeite molecule at lower pressures and temperatures (e.g. Medaris, 1972; Herzberg, 1978). For example, the high-Al transform pyroxenes (Figs 14 and 16) probably represent deeper cooling and an end to melting as a result of the transform edge effect. In these samples, alumina correlates positively with sodium and titanium, consistent with a pressure effect (Fig. 16). However, in the remaining samples, it is difficult to explain why a suite of peridotites, all with the same emplacement and *P–T* history, would have such highly variable alumina contents and zoning simply because of solid-state re-equilibration, particularly where

sodium increases with decreasing alumina (Fig. 13e and f). We suggest then that much of the pyroxene alumina zoning in plagioclase-free peridotites reflects cryptic metasomatism by small volumes of late transient melts meandering their way through the shallow mantle, causing variable but incomplete replacement of alumina by silica where plagioclase is not on the liquidus. This represents the chemical reaction



Alumina substitutes for silica in pyroxenes at low silica activity, and this suggests that most melts in equilibrium with residual abyssal peridotites were silica-poor in comparison with late impregnating melts. This is reasonably understood if the main melting phase occurs at relatively high pressures. In an open-system or near fractional melting environment, however, the last melts forming at the top of the melting column are probably silica-rich (e.g. Kushiro, 1973) and highly depleted in incompatible elements. This is also indicated, as discussed below, by the occurrence of late orthopyroxene sweat veins in the peridotites.

Although Al-poor pyroxene rims are characteristic of both spinel and plagioclase peridotites, the former do not share the systematic enrichment in iron, titanium and, for the most part, sodium found in the latter. This enrichment is also found in Cpx in the poikilitic dunite, troctolites, and olivine gabbros. This suggests impregnation of plagioclase peridotites by a melt or fluid considerably richer in incompatible elements than that in equilibrium with depleted mantle at the end of melting, and thus arguably a partially or fully aggregated MORB. Based on textural evidence, this represents local impregnation of melt in the shallow mantle near the base of the crust, consistent with the abundance of plagioclase peridotite around the Adam and Eve Magmatic Center. It is also the case that rare plagioclase-free spinel peridotites show the same geochemical features as plagioclase-peridotites; that is, enrichment in incompatible elements in addition to pyroxene alumina depletion relative to the main spinel peridotite trend. This suggests cryptic metasomatism by melt passing through peridotite where plagioclase was not yet on the liquidus.

Clinopyroxene titanium and sodium, however, correlate poorly with each other, and many plagioclase and spinel peridotites that show sodium enrichment do not have similar enrichment in titanium or depletion in alumina (Fig. 16). Whereas a MORB-like melt would produce metasomatic enrichment in both sodium and titanium, hydrous fluids have very low titanium partition coefficients (Eggler, 1987), which is the main difference between melt and hydrous fluid-related metasomatism (Menzies *et al.*, 1987). This suggests that the anomalous Na-enrichment is due to a later unrelated hydrous fluid.

Thus, we see three separate metasomatic events in the Kane peridotites: (1) a late event as a result of the last ultra-depleted melt increments produced by fractional melting; (2) local intragranular pooling of partially or fully aggregate MORB near the base of the crust; (3) a late hydrous event—perhaps of seawater or deuteritic origin.

Ultramafic veins

In addition to various mafic veins, olivine websterites and orthopyroxenites occur in abyssal peridotite suites. Whereas the former turn up with fair regularity, the latter are relatively rare. This should not be surprising, and is consistent with their relative abundance in ophiolites. Although orthopyroxenites are commonly found in ophiolite mantle sections, they constitute a tiny fraction of one per cent of the actual outcrop. Blind dredging of talus in an ophiolite, as at ocean ridges, would recover few, if any such veins. Thus, one cannot conclude that these are rarer in the abyssal mantle than in ophiolites. The abyssal olivine websterites and orthopyroxenites match those seen in ophiolitic peridotites, and illustrate that the processes occurring in both melting environments share similarities, even if the latter occur largely in the mantle wedge above a subduction zone.

Orthopyroxenites are often the last thing to form in ophiolite mantle sections, such as the Josephine Peridotite (e.g. Dick, 1977), where they have sharp boundaries with the wall-rock, and often occur in parallel sets that appear to have intruded along joints. They generally crosscut dunites and are only rarely crosscut by them. Thus, many orthopyroxenites are interpreted as late 'sweat veins' formed at the end of melting by back-reaction of the last melt increments in fractures with wall-rock olivine to form enstatite (Dick, 1977; Suzuki *et al.*, 2009). The melt required to do this would be a siliceous trace element-depleted low-alumina melt with a composition similar to high-magnesian andesite or boninite—exactly what would form by low-pressure melting of a highly depleted harzburgite residue at the end of fractional melting. Orthopyroxenites generally make up $\ll 1\%$ of the outcrop where they occur, and are irregularly distributed in many ophiolites, often absent over large areas, indicating that even the last melt fractions are irregularly distributed across the mantle at the end of melting.

Olivine websterites are generally the earliest identifiable structures in ophiolites and abyssal peridotites, and are crosscut by dunites. Possible origins include basaltic dikes (e.g. Mukasa & Shervais, 1999), layering formed by metamorphic differentiation in the presence of melt (Dick & Sinton, 1979), or stretched oceanic crust (Allègre & Turcotte, 1986). The latter origin seems improbable in view of the numerous parallel olivine websterite layers in ophiolite mantle sections, and it is unlikely, at best, that a 'basaltic' websterite would survive mantle melting beneath a

ridge. Many olivine websterites have similar mineral compositions to the wall-rock peridotites, and thus equilibrated with them at high temperature. Abyssal olivine websterites share this characteristic and probably formed *in situ* during mantle upwelling and melting as a result of either melt segregation (Dantas *et al.*, 2007) or metamorphic differentiation in the presence of melt (Dick & Sinton, 1979).

Origin of the Cain and Abel mafic veins

The Cain and Abel gabbroic veins could be rootless veins like those in the Oman Ophiolite (Ceuleneer *et al.*, 1996; Python & Ceuleneer, 2003); however, the Oman veins rarely constitute more than a few per cent of the outcrop. The high percentage at Cain and Abel Domes (10%), given their generally evolved compositions and lack of penetrative deformation, suggests that they are net veins related to small (<1 km) local intrusions in the shallow mantle, perhaps related to the intrusion postulated by Canales *et al.* (2008) beneath Cain Dome, or differentiated melts intruded from magmatic centers to the north or south (Dick *et al.*, 2008).

Crust–mantle transition zone and the Adam Dome Magmatic Complex

The close association of dunite, poikilitic dunite and associated olivine-rich troctolite with mantle peridotite at the Adam Dome Magmatic complex is convincing evidence that these rocks represent the crust–mantle transition. The Adam and Eve Dome dunites may initially have formed as cumulates, crystallized from olivine-saturated melts (Coleman, 1977) or by melt–rock reaction from mantle peridotite (Dick, 1977; Kelemen *et al.*, 1997; Quick, 1981*b*). In either case this could have occurred at depth within a mantle conduit or immediately beneath the crust where melts may pool as a result of dilation during mantle corner flow beneath the ridge axis (Rabinowicz *et al.*, 1987). However, as the dunites are now typically a mass of serpentine and clay with accessory relict spinel and their composition was probably subsequently modified by impregnating melts, there is little basis to discriminate between these origins; in any case both processes are probably involved in forming transition zone dunites (Nicolas & Prinzhofer, 1983). More to the point, spinels in a plagioclase-bearing dunite, poikilitic dunite, and related troctolite and olivine gabbro from Adam and Eve Domes plot to the right of the mantle array in Fig. 19 with decreasing forsterite content; this is consistent with crystallization from a fractionating melt, or reaction between a mantle-derived dunite and a fractionating melt. This defines the beginning of a crustal differentiation series progressing from dunite to troctolite, olivine gabbro, gabbro-norite, and oxide gabbro.

The olivine-rich troctolites and olivine gabbro veins mimic the calculated MORB olivine array in Fig. 12, and

could be explained as simple cumulates. The three col-linear troctolites at intermediate NiO in Fig. 12, however, are all from Dredge 21, and align orthogonal to the general trend of the MORB array. It is difficult, then, to relate them to each other through cumulate fractionation. They range in plagioclase content, however, from ~20 to 50 vol. %, with the most plagioclase corresponding to the lowest olivine NiO. This is consistent with textural interpretation that they are impregnated dunites with varying proportions of cumulus plagioclase and pyroxene from a fractionated MORB melt. This would result in the troctolite with the highest plagioclase proportion having the least and most reacted residual olivine with the lowest retained NiO. Such a spread in olivine NiO, and similar textures, has also been related to formation of Hole U1309D olivine-rich troctolite from dunite by melt–rock reaction from peridotite at the mantle transition zone (Drouin *et al.* 2007a, b, 2009; Suhr *et al.*, 2008).

As noted above, the Adam and Eve dunites, troctolites and associated peridotites are similar to the Oman crust–mantle transition zone rocks described by Boudier & Nicolas (1995) and we interpret our samples similarly. In Oman, mapping shows that mantle flow structures change abruptly from vertical upward flow to horizontal off-axis flow (Ceuleneer *et al.*, 1988), and numerical models indicate that this kink may correspond to a viscosity drop of at least two orders of magnitude, causing a zone of dilation and melt impregnation (Rabinowicz *et al.*, 1987). Thus, such a zone would create a region of rapid melt delivery to the base of the crust and underlying mantle, consistent with the associations at Adam and Eve Domes.

As we envisage it, as the mantle diverges beneath the crust at the ridge axis it creates a zone of dilation into which a volume of melt is flushed from the ascending mantle. Adiabatically decompressing, this melt is initially undersaturated with respect to pyroxene. Thus, it reacts with and strips the mantle of pyroxene by incongruent dissolution, precipitating additional olivine and spinel to form dunite (Boudier & Nicolas, 1995). Because of the mechanical effect of melt in a zone of dilation, the dunite periodically fractures and disaggregates as the melt becomes saturated in plagioclase, impregnating the dunite and cementing it to form troctolites (e.g. Boudier & Nicolas, 1995). This process is thermally limited, however, and compaction and buoyancy forces upwards intrusion of the melt into the overlying gabbro complex.

A characteristic feature of the poikilitic dunites and troctolites is high-Mg Cpx (Mg-number 87.3–92.0), which occurs as undeformed oikocrysts and small granular crystals. Clinopyroxene normally does not appear on the liquidus of a primitive MORB until 30–40% crystallization at a fairly low Mg-number (~80) and a relatively low temperature, ~1190°C (Grove & Bryan, 1983), so its appearance

in the transition zone cannot reflect simple fractional crystallization. A likely explanation is that because of the curvature of the low-pressure Ol–Cpx cotectic (e.g. Walker *et al.*, 1979), melt–rock reaction and the dissolution of enstatite and precipitation of olivine during dunite formation near the base of the crust bring the melt locally into the Cpx phase field.

Olivine-rich troctolites and dunites in association with mantle peridotites and gabbros have been previously sampled in various tectonic settings at slow- and ultraslow-spreading ocean ridges, most notably at the Cayman Trough (Ballard *et al.*, 1979; Elthon, 1987), where the occurrence of high-Mg clinopyroxene was attributed to high-pressure crystallization. Given the lack of penetrative deformation in these rocks, however, and the extensive evidence for melt–rock reaction in their formation (Lissenberg & Dick, 2008; Suhr *et al.*, 2008; Drouin *et al.*, 2009), we suggest that a better explanation is low-pressure crystallization at or near the base of the crust. Similar rocks drilled at Hess Deep ODP Site 895 in an EPR shallow mantle melt transport conduit may be closely related in origin. Crystallization of the Site 895 rocks, however, was heavily buffered by the mantle wall-rocks, and they are interpreted as the products of *in situ* solidification of stagnated melt trapped in the conduit by wall rock reaction (Arai & Matsukage, 1996; Arai *et al.*, 1996; Dick & Natland, 1996).

The thickness of the main gabbro body is hard to decipher, and whereas geometric reconstruction shows that the west face of Adam Dome exposes an ~1 km section below the detachment fault surface (Dick *et al.*, 2008), Dredge 27 evidently sampled the crust–mantle transition zone below the gabbro <2 km to the north. This suggests that the main gabbro body is unlikely to be more than a few kilometers thick, and it is clear that it is absent a few kilometers further east at Eve Dome. Noting the abundance of primitive gabbros and troctolites at Adam Dome, in comparison with the abundant oxide gabbros drilled on the detachment surface at the inside-corner high of the MARK area, and the similar abundance at Hole 735B, this probably does not represent the full section. Rather, we suggest that magmatism may have already waned or stopped entirely here before emplacement of the block to the surface. As a consequence, the detachment fault plunged downward from a stable position at the dike–gabbro transition, to progressively exhume deeper portions of the section, passing them through the zone of active diking until the crust–mantle transition zone was pulled to the surface at Eve Dome.

A scarcity of wehrlites and the ophiolite analogy

The crust–mantle transition zone in many ophiolites includes substantial thicknesses (>100 m) of interlayered

plagioclase-free wehrlite and dunite, an association that is very rare in mid-ocean ridge rock suites if it exists at all (Dick, 1989). In ophiolites the proportion of dunite diminishes up-section from the transition zone into the overlying gabbroic crust, and interlayered plagioclase wehrlite may appear (e.g. Casey *et al.*, 1981; Elthon *et al.*, 1982; Furnes *et al.*, 1988; Reuber, 1988; Boudier & Nicolas, 1995). Plagioclase wehrlites can be abundant, and constitute between 20 and 40% of the Oman gabbro section (Juteau *et al.*, 1988; Boudier & Nicolas, 1995), whereas they are rare in abyssal gabbro suites. The plagioclase-free wehrlites consist of either granular to idiomorphic Cpx with interstitial olivine, or Cpx oikocrysts enclosing rounded olivine chadocrysts, and form prominent banded outcrops with dunite defined by variably clinopyroxene-rich centimeter- to meter-thick layers. Many of these rocks may have formed by melt–rock reaction (e.g. Bédard *et al.*, 2000) similar to what is proposed for the Adam Dome poikilitic wehrlites and olivine-rich troctolites. Abyssal wehrlites have been reported in harzburgite tectonite sections as a small centimeter-scale patch of Cpx in a Hess Deep ODP Site 895 dunite (Arai & Takemoto, 2007) and as elongated Cpx segregations in ODP Site 920 dunitites. In addition, Girardeau & Francheteau (1993) have reported three plagioclase wehrlites associated with a large suite of harzburgites from Hess Deep that appear mineralogically and genetically equivalent to the Oman plagioclase wehrlites. Although these samples demonstrate that wehrlitic rocks may form by melt–rock reaction with peridotite or dunite in the lower crust and shallow mantle at ocean ridges (Girardeau, 1979; Casey, 1997; Arai & Takemoto, 2007), they are not equivalent to the massive banded plagioclase-free wehrlites in ophiolite crust–mantle transition zones. The Adam Dome poikilitic dunitites, in particular, are transitional to troctolite, representing ‘gabbroic’ rather than ‘wehrlitic’ impregnations (Fig. 10c and d).

The scarcity of wehrlite in abyssal peridotite–gabbro suites is a problem for using Oman and other ophiolites as direct analogues for modern ocean ridges. Whereas many workers have attributed wehrlites to subduction-related magmatism (e.g. Ceuleneer & Le Sueur, 2008), Juteau *et al.* (1988) have suggested they may represent the last stages of magmatism at an abandoned ridge axis. Although wehrlites may be subduction-related, at a dying spreading center the last melts out of the mantle are probably also highly refractory and dominated by melt–rock reaction with a no longer ascending refractory mantle. As noted above, enstatite dissolution may then bring melts into Cpx saturation, explaining the abundant wehrlites. The Adam Dome magmatic center may have been dying out, but mantle upwelling was not, and magmatism merely shifted to another location beneath the paleo-ridge axis—hence the absence of wehrlite.

Melt transport and accumulation beneath transforms

Plagioclase-peridotites are generally abundant in transform fault zones (Fig. 3), and at a few localities, such as the Romanche FZ, contain large volumes of plagioclase (2–18 vol. %) (Dick, 1989; Seyler & Bonatti, 1997; Tartarotti *et al.*, 2002). Where they occur, it is often hard to find a sample not impregnated by plagioclase. This mirrors the situation in ophiolites, where most peridotite is plagioclase-free harzburgite, but more rarely plagioclase lherzolite is abundant, as at the Trinity Ophiolite in California (e.g. Quick, 1980, 1981a; Ceuleneer & Le Sueur, 2008), the Lanzo Massif in Italy (e.g. Boudier & Nicolas, 1972; Piccardo *et al.*, 2006), and the Othris Peridotite in Greece (e.g. Menzies, 1973; Dijkstra *et al.*, 2001). At Othris it has been proposed that melt is locally trapped as a result of the influence of a transform (Dijkstra *et al.*, 2001).

Until now, there have been few data to directly compare *in situ* transform and sub-axial mantle environments. Based on the scarcity of plagioclase peridotite in the main Kane core complex, compared with transforms in general, plagioclase peridotites appear to be significantly more abundant in the latter. Dunitites indicative of focused shallow melt flow are also rare at transforms. Thus, it would seem that melt transport through the mantle at transforms is inefficient and that, not infrequently, what little melt is produced there finally back-impregnates the surrounding mantle. This local interstitial pooling of aggregate MORB at the asthenosphere–lithosphere boundary and the formation of plagioclase peridotite is probably due to dilation of the mantle during corner flow at the plate boundary (Rabinowicz *et al.*, 1987).

A scarcity of dunite near transforms argues that they do not generally predate the ridge-melting event. Moreover, the abundance of plagioclase peridotite and scarcity of dunite in transforms raises the possibility that dunite formation beneath ocean ridges is largely a shallow phenomenon, and that aggregation of MORB may not require deep dunite channels. Instead, this may occur, in part, in local zones of depleted harzburgite transitional to dunite (Dick, 1989).

ACKNOWLEDGEMENTS

The authors would like to acknowledge Margaret Sulanowska, who assisted in curation and data processing, and Dr. Neel Chatterjee of MIT, who conducted the microprobe analyses using sample documentation prepared by Sulanowska. Conversations with Glen Gaetani, Greg Hirth, Brian Tucholke, Pablo Canales, Min Xu and Maurice Tivey greatly enhanced our understanding and interpretation of the tectonics and petrology of the Kane Megamullion. Our work also builds upon that of previous investigators in the region, particularly that of Jean Marie Auzende, Mathilde Cannat and Indraneel Ghose, whose

work provided an invaluable resource on the transform wall and its petrology. The paper was greatly improved by insightful reviews by Georges Ceuleneer, Martin Menzies and Tomo Moroshita.

FUNDING

This work was supported by the United States National Science Foundation [Grants OCE-0526905, OCE-0524408, and OCE-0827825].

SUPPLEMENTARY DATA

Supplementary data for this paper are available at *Journal of Petrology* online.

REFERENCES

- Albee, A. L. & Ray, L. (1970). Correction factors for electron microprobe analysis of silicates, oxides, carbonates, phosphates and sulphates. *Analytical Chemistry* **42**, 1408–1414.
- Allègre, C. J. & Turcotte, D. L. (1986). Implications of a two component marble-cake mantle. *Nature* **323**, 123–127.
- Arai, S. & Matsukage, K. (1996). Petrology of gabbro–troctolite–peridotite complex from Hess Deep, equatorial Pacific: implications for mantle–melt interaction within the oceanic lithosphere. In: Mevel, C., Gillis, K. M., Allan, J. F. & Meyer, P. S. (eds) *Proceedings of the Ocean Drilling Program, Scientific Results, V. 147*, p. 157–172, College Station, TX: Ocean Drilling Program.
- Arai, S. & Takemoto, Y. (2007). Mantle wehrlite from Hess Deep as a crystal cumulate from an ultra-depleted primary melt in East Pacific Rise. *Geophysical Research Letters* **34**, article number L08302.
- Arai, S., Matsukage, K. & Isobe, E. (1996). *Concentration of incompatible elements in oceanic mantle: Effect of melt/wall interaction in stagnant or failed melt conduits within peridotite*. Kakuma: Kanazawa University.
- Asimow, P. D. & Langmuir, C. H. (2003). The importance of water to oceanic melting regimes. *Nature* **421**, 815–820.
- Auzende, J.-M., Cannat, M., Gente, P., Henriot, J.-P., Juteau, T., Karson, J. A., Lagabrielle, Y. & Tivey, M. A. (1992). Rapport de la Campagne Kanaut du Nautille sur le N/O Nadir, 15 November–16 December 1992, Ifremer, Brest, 426 pp.
- Auzende, J.-M., Cannat, M., Gente, P., Henriot, J.-P., Juteau, T., Karson, J., Lagabrielle, Y., Mével, C. & Tivey, M. (1993). Affleurements des roches profondes de la croûte océanique et du manteau sur le mur sud de la fracture Kane (Atlantique central): observations par submersible. *Comptes Rendus de l'Académie des Sciences* **317**, 1641–1648.
- Auzende, J.-M., Cannat, M., Gente, P., Henriot, J.-P., Juteau, T., Karson, J., Lagabrielle, Y., Mével, C. & Tivey, M. (1994). Observation of sections of oceanic crust and mantle cropping out on the southern wall of Kane FZ (N. Atlantic). *Terra Nova* **6**, 143–148.
- Ballard, R., Bryan, W., Dick, H., Emery, K. O., Thompson, G., Uchupi, E., Davis, K. E., Boer, J., DeLong, S., Fox, P., Malcolm, F., Spydell, R., Stroup, J., Melson, W. & Wright, R. (1979). Geological and geophysical investigation of the Midcayman Rise Spreading Center: Initial results and observations. In: Talwani, M., Harrison, C. G. & Hayes, D. E. (eds) *Deep Drilling Results in the Atlantic Ocean: Ocean Crust*. Washington, DC: American Geophysical Union, pp. 66–93.
- Bédard, J., Hébert, R., Berclaz, A. & Varfalvy, V. (2000). Suyntexis and the genesis of lower ocean crust. *Geological Society of America Special Paper 349. Ophiolites and the Ocean Crust: New Insights from Field Studies and the Ocean drilling Program*, Dilek, Y., Moores, E., Elthon, D. and Nicolas, A. (eds), Boulder, CO: Geological Society of America, 105–119.
- Bence, A. E. & Albee, A. L. (1968). Empirical correction factors for electron microprobe analysis of silicates and oxides. *Journal of Geology* **76**, 382–403.
- Bonatti, E., Peyve, A., Kepezhinskas, P., Kurentsova, N., Seyler, M., Skolotnev, S. & Udintsev, G. (1992). Upper mantle heterogeneity below the Mid-Atlantic Ridge, 0°–15°N. *Journal of Geophysical Research* **97**, 4461–4476.
- Bonatti, E., Ligi, M., Brunelli, D., Cipriani, A., Fabretti, P., Ferrante, V., Gasperini, L. & Ottolini, L. (2003). Mantle thermal pulses below the Mid-Atlantic Ridge and temporal variations in the formation of oceanic lithosphere. *Nature* **423**, 499–505.
- Boudier, F. (1991). Olivine xenocrysts in picritic magmas. An experimental and microstructural approach. *Contributions to Mineralogy and Petrology* **109**, 114–123.
- Boudier, F. & Nicolas, A. (1972). Fusion partielle gabbroïque dans la lherzolite de Lanzo. *Bulletin Suisse de Minéralogie et Pétrographie* **52**, 39–56.
- Boudier, F. & Nicolas, A. (1985). Harzburgite and lherzolite subtypes in ophiolitic and oceanic environments. *Earth and Planetary Science Letters* **76**, 84–92.
- Boudier, F. & Nicolas, A. (1995). The nature of the Moho transition zone in the Oman ophiolite. *Journal of Petrology* **36**, 777–796.
- Brunelli, D., Seyler, M., Cipriani, A., Ottolini, L. & Bonatti, E. (2006). Discontinuous melt extraction and weak refertilization of mantle peridotites at the Vema lithospheric section (Mid-Atlantic Ridge). *Journal of Petrology* **47**, 745–771.
- Bryan, W. B., Thompson, G. & Ludden, J. N. (1981). Compositional variation in normal MORB from 22°–25°N: Mid-Atlantic Ridge and Kane Fracture Zone. *Journal of Geophysical Research* **86**, 11815–11836.
- Burgath, K., Marchig, V. & Mussallam, K. (1997). Mineralogical, structural, and chemical variability of mantle sections from Holes 920B and 920D. In: Karson, J. A., Cannat, M., Miller, D. J. & Elthon, D. (eds) *Proceedings of the Ocean Drilling Program, Scientific Results, 153*. College Station, TX: Ocean Drilling Program, pp. 505–519.
- Canales, J. P., Tüchölke, B. E., Xu, M., Collins, J. A. & DuBois, D. L. (2008). Seismic evidence for large-scale compositional heterogeneity of oceanic core complexes. *Geochemistry, Geophysics, Geosystems* **9**, doi:10.1029/2008GC002009.
- Cannat, M. (1993). Emplacement of mantle rocks in the seafloor at mid-ocean ridges. *Journal of Geophysical Research* **98**, 4163–4172.
- Cannat, M. & Casey, J. F. (1995). An ultramafic lift at the Mid-Atlantic Ridge: successive stages of magmatism in serpentinized peridotites from the 15 degree N region. In: Vissers, R. L. M. & Nicolas, A. (eds) *Mantle and Lower Crust Exposed in Oceanic Ridges and in Ophiolites*. Dordrecht: Kluwer Academic, pp. 5–34.
- Cannat, M., Bideau, D. & Herbert, R. (1990). Plastic deformation and magmatic impregnation in serpentinized ultramafic rocks from the Garret transform fault East Pacific Rise. *Earth and Planetary Science Letters* **101**, 216–232.
- Cannat, M., Bideau, D. & Bougault, H. (1992). Serpentinized peridotites and gabbros in the Mid-Atlantic Ridge axial valley at 15°37'N and 16°52'N. *Earth and Planetary Science Letters* **109**, 87–106.
- Cannat, M., Mével, C., Maia, M., Deplus, C., Durand, C., Gente, P., Agrinier, P., Belarouchi, A., Dubuisson, G., Humler, E. & Reynolds, J. (1995). Thin crust, ultramafic exposures, and rugged

- faulting patterns at the Mid-Atlantic Ridge (22°–24°N). *Geology* **23**, 49–52.
- Cannat, M., Chatin, F., Whitechurch, H. & Ceuleneer, G. (1997). Gabbroic rocks trapped in the upper mantle at the Mid-Atlantic Ridge. In: Karson, J. A., Cannat, M., Miller, D. J. & Elthon, D. (eds) *Ocean Drilling Program, Scientific Results, 153*. College Station, TX: Ocean Drilling Program.
- Cannat, M., Sauter, D., Mendel, V., Ruellan, E., Okino, K., Escartin, J., Combier, V. & Baala, M. (2006). Modes of seafloor generation at a melt-poor ultraslow-spreading ridge. *Geology* **34**, 605–608.
- Casey, J. F. (1997). Comparison of major- and trace-element geochemistry of abyssal peridotites and mafic plutonic rocks with basalts from the MARK region of the Mid-Atlantic Ridge. In: Karson, J. A., Cannat, M., Miller, D. J. & Elthon, D. (eds) *Proceedings of the Ocean Drilling Program, Scientific Results, 153*. College Station, TX: Ocean Drilling Program, pp. 181–241.
- Casey, J. F., Dewey, J. F., Fox, P. J., Karson, J. A. & Rosencrantz, E. (1981). Heterogeneous nature of oceanic crust and upper mantle: a perspective from the Bay of Islands Ophiolite Complex. In: Emiliani, C. (ed.) *The Sea*. New York: Wiley, pp. 305–338.
- Ceuleneer, G. & Cannat, M. (1997). High-temperature ductile deformation of Site 920 peridotites. In: Karson, J. A., Cannat, M., Miller, D. J. & Elthon, D. (eds) *Proceedings of the Ocean Drilling Program, Scientific Results*. **153**, College Station, TX: Ocean Drilling Program, 23–34.
- Ceuleneer, G. & Le Sueur, E. (2008). The Trinity ophiolite (California): the strange association of fertile mantle peridotite with ultra-depleted crustal cumulates. *Bulletin de la Société Géologique de France* **179**, 503–518.
- Ceuleneer, G., Nicolas, A. & Boudier, F. (1988). Mantle flow patterns at an oceanic spreading centre: the Oman peridotites record. *Tectonophysics* **151**, 1–26.
- Ceuleneer, G., Monnereau, M. & Amri, I. (1996). Thermal structure of a fossil mantle diapir inferred from the distribution of mafic cumulates. *Nature* **379**, 149–153.
- Church, W. R. & Stevens, R. K. (1971). Early Paleozoic ophiolite complexes of the Newfoundland Appalachians as mantle–oceanic crust sequences. *Journal of Geophysical Research* **76**, 1460–1466.
- Coleman, R. G. (1977). *Ophiolites: Ancient Oceanic Lithosphere*. New York: Springer.
- Constantin, M., Hékinian, R., Ackermann, D. & Stoffers, P. (1995). Mafic and ultramafic intrusions into upper mantle peridotites from fast spreading centers of the Easter Microplate (South East Pacific). In: Vissers, R. L. M. & Nicolas, A. (eds) *Mantle and Lower Crust Exposed in Oceanic Ridges and in Ophiolites*. Dordrecht: Kluwer Academic, pp. 71–120.
- Dantas, C., Ceuleneer, G., Gregoire, M., Python, M., Freydier, R., Warren, J. & Dick, H. J. B. (2007). Pyroxenites from the Southwest Indian Ridge, 9–16°E; cumulates from incremental melt fractions produced at the top of a cold melting regime. *Journal of Petrology* **48**, 647–660.
- Detrick, R. S., Jr, Purdy, G. & M. (1980). The crustal structure of the Kane Fracture Zone from seismic refraction studies. *Journal of Geophysical Research* **85**, 3759–3777.
- Detrick, R. S., Mutter, J. C., Buhl, P. & Kim, I. I. (1990). No evidence from multichannel reflection data for a crustal magma chamber in the MARK area on the Mid-Atlantic Ridge. *Nature* **347**, 61–64.
- Detrick, R. S., White, R. S. & Purdy, G. M. (1993). Crustal structure of North Atlantic fracture zones. *Reviews of Geophysics* **31**, 439–458.
- Dick, H. J., Tivey, M. A., Tucholke, B. E. & Cheadle, M. J. (2005). The plutonic foundation of a MAR ridge spreading segment: The Kane Oceanic Core Complex. *EOS Transactions, American Geophysical Union* **86**, Abstract T33G-02.
- Dick, H. J. B. (1977). Evidence of partial melting in the Josephine Peridotite. In: Dick, H. J. B. (ed.) *Magma Genesis*. Portland, OR: Oregon Department of Geology and Mineral Industries, pp. 59–62.
- Dick, H. J. B. (1989). Abyssal peridotites, very slow spreading ridges and ocean ridge magmatism. In: Saunders, A. D. & Norry, M. J. (eds) *Magmatism in the Ocean Basins*. Geological Society, London, *Special Publications* **42**, 71–105.
- Dick, H. J. B. & Bryan, W. B. (1978). Variation of basalt phenocryst mineralogy and rock compositions in DSDP Hole 396B. In: Dmitriev, L. & Heirtzler, J. (eds) *Initial Reports of the Deep Sea Drilling Project, XLVI*. Washington, DC: US Government Printing Office, pp. 215–225.
- Dick, H. J. B. & Bullen, T. (1984). Chromian spinel as a petrogenetic indicator in abyssal and alpine-type peridotites and spatially associated lavas. *Contributions to Mineralogy and Petrology* **86**, 54–76.
- Dick, H. J. B. & Fisher, R. L. (1984). Mineralogic studies of the residues of mantle melting: Abyssal and alpine-type peridotites. In: Kornprobst, J. (ed.) *Kimberlites II. The Mantle and Crust–Mantle Relationships*. Amsterdam: Elsevier, pp. 295–308.
- Dick, H. J. B. & Natland, J. H. (1994). Melt transport and evolution in the shallow mantle beneath the East Pacific Rise: preliminary results from ODP site 895. *Mineralogical Magazine* **58A**, 229–228.
- Dick, H. J. B. & Natland, J. H. (1996). Late stage melt evolution and transport in the shallow mantle beneath the East Pacific Rise. In: Gillis, K., Mevel, C. & Allan, J. (eds) *Ocean Drilling Program, Scientific Results*. **147**, College Station, TX: Ocean Drilling Program, 103–134.
- Dick, H. J. B. & Sinton, J. (1979). Compositional layering in alpine peridotites: evidence for pressure solution creep in the mantle. *Journal of Geology* **87**, 403–416.
- Dick, H. J. B., Fisher, R. L. & Bryan, W. B. (1984). Mineralogic variability of the uppermost mantle along mid-ocean ridges. *Earth and Planetary Science Letters* **69**, 88–106.
- Dick, H. J. B., Natland, J. H., Alt, J. C. *et al.* (2000). A long in-situ section of the lower ocean crust: results of ODP Leg 176 drilling at the Southwest Indian Ridge. *Earth and Planetary Sciences* **179**, 31–51.
- Dick, H. J. B., Arai, S., Hirth, G. & John, B. J. (2001). KROO-06 Scientific PartyA subhorizontal cross-section through the crust–mantle boundary at the SW Indian Ridge. *Geophysical Research Abstracts* **3**, 794.
- Dick, H. J. B., Ozawa, K., Meyer, P. S., Niu, Y., Robinson, P. T., Constantin, M., Hebert, R., Maeda, J., Natland, J. H., Hirth, G. & Mackie, S. (2002). Primary silicate mineral chemistry of a 1.5-km section of very slow spreading lower ocean crust: ODP Hole 735B, Southwest Indian Ridge. In: Natland, J. H., Dick, H. J. B., Miller, D. J. & Von Herzen, R. (eds) *Proceedings of the Ocean Drilling Program, Scientific Results* **176**, College Station, TX: Ocean Drilling Program, 1–60, [CD-ROM].
- Dick, H. J. B., Tivey, M. A. & Tucholke, B. E. (2008). Plutonic foundation of a slow-spreading ridge segment: Oceanic core complex at Kane Megamullion, 23°30'N, 45°20'W. *Geochemistry, Geophysics, Geosystems* **9**, 44.
- Dickey, J. S., Jr (1976). A hypothesis for the origin of podiform chromite deposits. *Geochimica et Cosmochimica Acta* **39**, 1061–1074.
- Dijkstra, A. H., Drury, M. R. & Vissers, R. L. M. (2001). Structural petrology of plagioclase peridotites in the West Othris Mountains (Greece): Melt impregnation in mantle lithosphere. *Journal of Petrology* **42**, 5–24.
- Drouin, M., Godard, M. & Ildefonse, B. (2007a). Origin of olivine-rich gabbroic rocks from the Atlantis Massif (MAR 30°N, IODP

- Hole U1309D): petrostructural and geochemical study. *Geophysical Research Abstracts* **9**, 06550.
- Drouin, M., Godard, M. & Ildefonse, B. (2007b). Origin of olivine-rich troctolites from IODP Hole U1209D in the Atlantis Massif (Mid-Atlantic Ridge): Petrostructural and geochemical study. *Eos Trans. AGU* **88**(52), Abstract T53B-1300.
- Drouin, M., Godard, M., Ildefonse, B., Bruguier, O. & Garrido, C. J. (2009). Geochemical and petrographic evidence for magmatic impregnation in the oceanic lithosphere at Atlantis Massif, Mid-Atlantic Ridge (IODP Hole U1309D, 30°N). *Chemical Geology* **264**, 71–88.
- Eggler, D. H. (1987). Solubility of major and trace elements in mantle metasomatic fluids: experimental constraints. In: Menzies, M. A. & Hawkesworth, C. J. (eds) *Mantle Metasomatism*. London: Academic Press, pp. 21–41.
- Elthon, D. (1987). Petrology of gabbroic rocks from the Mid-Cayman Rise Spreading Center. *Journal of Geophysical Research* **92**, 658–682.
- Elthon, D., Casey, J. F. & Komor, S. (1982). Mineral chemistry of ultramafic cumulates from the North Arm Massif of the Bay of Islands ophiolite: evidence for high-pressure crystal fractionation of oceanic basalts. *Journal of Geophysical Research* **87**, 8717–8734.
- Engel, A. E. J. & Engel, C. G. (1964a). Composition of basalts from the Mid-Atlantic Ridge. *Science* **144**, 1330–1333.
- Engel, A. E. J. & Engel, C. G. (1964b). Igneous rocks of the East Pacific Rise. *Science* **146**, 477–485.
- Engel, A. E. J., Engel, C. G. & Havens, R. G. (1965). Chemical characteristics of oceanic basalts and the upper mantle. *Geological Society of America Bulletin* **76**, 719–734.
- Francheteau, J., Choukroune, P., Hékinian, R., Le Pichon, X. & Needham, H. D. (1976). Oceanic fracture zones do not provide deep sections in the crust. *Canadian Journal of Earth Sciences* **13**, 1223–1235.
- Furnes, H., Pedersen, R. B. & Stillman, C. J. (1988). The Leka Ophiolite Complex, central Norwegian Caledonides: field characteristics and geotectonic significance. *Journal of the Geological Society, London* **145**, 401–412.
- Gaetani, G. A. & Grove, T. L. (1998). The influence of water on the melting of mantle peridotite. *Contributions to Mineralogy and Petrology* **131**, 323–346.
- Gaetani, G. A. & Watson, E. B. (2000). Open system behavior of olivine-hosted melt inclusions. *Earth and Planetary Science Letters* **183**, 27–41.
- Ghose, I. (1997). Fusion du manteau et cristallisation des roches gabbroïques près de faille transformante Kane, (Océan Atlantique). Université de Paris VII, 226 pp.
- Ghose, I., Cannat, M. & Seyler, M. (1996). Transform fault effect on mantle melting in the MARK area (Mid-Atlantic Ridge south of the Kane Transform). *Geology* **24**, 1139–1142.
- Girardeau, J. (1979). Structure des ophiolites de l'ouest de terre neuve et modèle de croûte océanique, Institut des Sciences de la Nature de l'Université de Nantes.
- Girardeau, J. & Francheteau, J. (1993). Plagioclase-wehrlites and peridotites on the East Pacific Rise (Hess Deep) and the Mid-Atlantic Ridge (DSDP Site 339) evidence for magma percolation in the oceanic upper mantle. *Earth and Planetary Science Letters* **115**, 137–149.
- Girardeau, J. & Mercier, J. C. C. (1992). Evidence for plagioclase-lherzolites intrusion in the Mid-Atlantic ridge. In: Parsons, L. M., Murton, B. J. & Browning, P. (eds.) Geological Society Special Publication: *Ophiolites and Their Modern Analogues*, The Geological Society, London, 241–250.
- Girardeau, J. & Nicolas, A. (1981). The structures of two ophiolite massifs, Bay-of-Islands, Newfoundland: A model for the oceanic crust and upper mantle. *Tectonophysics* **77**, 1–34.
- Godard, M., Jousset, M. D. & Bodinier, J.-L. (2000). Relationships between geochemistry and structure beneath a paleo-spreading centre: A study of the mantle section in the Oman ophiolite. *Earth and Planetary Science Letters* **180**, 133–148.
- Godard, M., Lagabrielle, Y., Alard, O. & Harvey, J. (2008). Geochemistry of the highly depleted peridotites drilled at ODP Sites 1272 and 1274 (Fifteen–Twenty Fracture Zone, Mid-Atlantic Ridge): Implications for mantle dynamics beneath a slow spreading ridge. *Earth and Planetary Science Letters* **267**, 410–425.
- Graham, A. L., Symes, R. F., Bevan, J. C. & Din, V. K. (1979). Chromium-bearing spinels in some rocks of Leg 45: Phase chemistry, zoning and relation to host basalt chemistry. In: Melson, W. G. & Rabinowitz, P. D. (eds) *Initial Reports of the Deep Sea Drilling Project*. **45**, Washington, DC: US Government Printing Office, 145, 581–586.
- Green, D. H. & Hibberson, W. (1970). The instability of plagioclase in peridotite at high pressure. *Lithos* **3**, 209–221.
- Grove, T. L. & Bryan, W. B. (1983). Fractionation of pyroxene-phyric MORB at low pressure: An experimental study. *Contributions to Mineralogy and Petrology* **84**, 293–309.
- Hamlyn, P. R. & Bonatti, E. (1980). Petrology of mantle-derived ultramafics from the Owen Fracture Zone, northwest Indian Ocean: implications for the nature of the oceanic upper mantle. *Earth and Planetary Science Letters* **48**, 65–79.
- Hart, S. R. & Davis, K. E. (1978). Nickel partitioning between olivine and silicate melt. *Earth and Planetary Science Letters* **40**, 203–219.
- Hékinian, R., Bideau, D., Francheteau, J., Cheminee, J. L., Armijo, R., Lonsdale, P. & Blum, N. (1993). Petrology of the East Pacific Rise crust and upper mantle exposed in Hess Deep (Eastern Equatorial Pacific). *Journal of Geophysical Research* **98**, 8069–8094.
- Hellebrand, E., Snow, J. E., Dick, H. J. B. & Hofmann, H. (2001). Coupled major and trace-element indicators in mid-ocean ridge peridotites. *Nature* **410**, 677–681.
- Herzberg, C. (1978). Pyroxene geothermometry and geobarometry: experimental and thermodynamic evaluation of some subsolidus phase relations involving pyroxenes in the system CaO–MgO–Al₂O₃–SiO₂. *Geochimica et Cosmochimica Acta* **42**, 945–957.
- Ildefonse, B., Blackman, D. K., John, B. E., Ohara, Y., Miller, D. J., MacLeod, C. J. & Party, IODPES (2007). Oceanic core complexes and crustal accretion at slow spreading ridges. *Geology* **35**, 623–626.
- Irvine, T. N. (1965). Chromian spinel as a petrogenetic indicator. Part 1. Theory. *Canadian Journal of Earth Sciences* **2**, 648–672.
- Irvine, T. N. (1967). Chromian spinel as a petrogenetic indicator. Part 2. Petrologic applications. *Canadian Journal of Earth Sciences* **4**, 72–103.
- Jaroslow, G. E., Hirth, G. & Dick, H. J. B. (1996). Abyssal peridotite mylonites: implications for grain-size sensitive flow and strain localization in the oceanic lithosphere. *Tectonophysics* **256**, 17–37.
- Johnson, K. T. M. & Dick, H. J. B. (1992). Open system melting and the temporal and spatial variation of peridotite and basalt compositions at the Atlantis II Fracture Zone. *Journal of Geophysical Research* **97**, 9219–9241.
- Juteau, T., Ernewein, M., Reuber, I., Whitechurch, H. & Dahl, R. (1988). Duality of magmatism in the plutonic sequence of the Sumail Nappe, Oman. *Tectonophysics* **151**, 107–135.
- Kaczmarek, M.-A. & Müntener, O. (2008). Juxtaposition of melt impregnation and high-temperature shear zones in the upper mantle; field and petrological constraints from the Lanzo Peridotite (Northern Italy). *Journal of Petrology* **49**, 2187–2220.

- Kempton, P. D. & Stephens, C. J. (1997). Petrology and geochemistry of nodular websterite inclusions in harzburgite, Hole 920D, ODP Leg 153. In: Karson, J. A., Cannat, M., Miller, D. J. & Elthon, D. (eds) *Proceedings of the Ocean Drilling Program, Scientific Results*. College Station, TX: Ocean Drilling Program, 321–322.
- Kelemen, P. B., Shimizu, N. & Salters, V. J. M. (1995). Extraction of mid-ocean-ridge basalt from the upwelling mantle by focused flow of melt in dunite channels. *Nature* **375**, 747–753.
- Kelemen, P. B., Hirth, G., Shimizu, N., Speigelman, M. & Dick, H. (1997). A review of melt migration processes in the adiabatically upwelling mantle beneath oceanic spreading ridges. *Philosophical Transactions of the Royal Society of London, Series A* **355**, 283–318.
- Kelemen, P. B., Kikawa, E. & Miller, D. J. *et al.* (eds) (2004). *Proceedings of the Ocean Drilling Program, Part A: Initial Reports*, 209. College Station, TX: Ocean Drilling Program.
- Klein, E. M. & Langmuir, C. H. (1987). Global correlations of ocean ridge basalt chemistry with axial depth and crustal thickness. *Journal of Geophysical Research* **92**, 8089–8115.
- Komor, S. C., Grove, T. L. & Hébert, R. (1990). Abyssal peridotites from ODP Hole 670A (218100N, 458020W): Residues of mantle melting exposed by non-constructive axial divergence. In Detrick, R., Honnorez, J., Bryan, W.B., Juteau, T. (eds) *Proceedings of the Ocean Drilling Program, Scientific Results, 106/109*, College Station, TX: Ocean Drilling Program, pp. 85–101.
- Kuo, B.-Y. & Forsyth, D. W. (1988). Gravity anomalies of the ridge–transform system in the South Atlantic between 31 and 34°S: Upwelling centers and variations in crustal thickness. *Marine Geophysical Researches* **10**, 205–232.
- Kushiro, I. (1973). Origin of some magmas in oceanic and circum-oceanic regions. *Tectonophysics* **17**, 211–222.
- Lagabrielle, Y. & Cannat, M. (1990). Alpine Jurassic ophiolites resemble the modern central Atlantic Basement. *Geology* **18**, 319–322.
- Lin, J., Purdy, G. M., Schouten, H., Sempere, J.-C. & Zervas, C. (1990). Evidence from gravity data for focused magmatic accretion along the Mid-Atlantic Ridge. *Nature* **344**, 627–632.
- Lippard, S. J., Shelton, A. W. & Gass, I. G. (1986). *The Ophiolite of Northern Oman*. Malden, MA: Blackwell Science.
- Lissenberg, C. J. & Dick, H. J. B. (2008). Melt–rock reaction in the lower ocean crust and its implications for the genesis of mid-ocean ridge basalt. *Earth and Planetary Science Letters* **271**, 311–325.
- Lissenberg, J. & Dick, H. (2006). Melt–rock reaction in oceanic gabbros and its implications for the genesis of mid-ocean ridge basalt. *EOS Transactions, American Geophysical Union, Fall Meeting Supplement* **87**, Abstract V23E-0695.
- Medaris, L. G., Jr (1972). High-pressure peridotites in southwestern Oregon. *Geological Society of America Bulletin* **83**, 41–58.
- Melson, W. G., Hart, S. R. & Thompson, G. (1972). St. Paul's Rocks, equatorial Atlantic: Petrogenesis, radiometric ages, and implications on sea-floor spreading. In: Shagam, R., Hargraves, R. B., Morgan, W. J., Van Houten, F. B., Burk, C. A., Holland, H. D. & Hollister, L. C. (eds) *Studies in Earth and Space Sciences*. Denver, CO: Geological Society of America, pp. 241–272.
- Menzies, M. (1973). Mineralogy and partial melt textures within an ultramafic–mafic body, Greece. *Contributions to Mineralogy and Petrology* **42**, 273–285.
- Menzies, M. & Allen, C. (1974). Plagioclase lherzolite–residual mantle relationships within two eastern Mediterranean ophiolites. *Contributions to Mineralogy and Petrology* **45**, 197–213.
- Menzies, M. A., Rogers, N., Tindle, A. & Hawkesworth, C. J. (1987). Metasomatic and enrichment processes in lithospheric peridotites, an effect of asthenosphere–lithosphere interaction. In: Menzies, M. A. & Hawkesworth, C. J. (eds) *Mantle Metasomatism*. London: Academic Press, 313–361.
- Mével, C., Cannat, M., Gente, P., Marion, E., Auzende, J. M. & Karson, J. A. (1991). Emplacement of deep crustal and mantle rocks on the west wall of the MARK area (Mid-Atlantic Ridge, 23°N). *Tectonophysics* **190**, 31–53.
- Meyer, P. S., Dick, H. J. B. & Thompson, G. (1989). Cumulate gabbros from the Southwest Indian Ridge, 54°S–7°16'E: implications for magmatic processes at a slow spreading ridge. *Contributions to Mineralogy and Petrology* **103**, 44–63.
- Michael, P. J. & Bonatti, E. (1985). Petrology of ultramafic rocks from Sites 556, 558, and 560 in the North Atlantic. In: Bougault, H. & Cande, S. (eds) *Initial Reports of the Deep Sea Drilling Project*. Washington, D.C.: US Government Printing Office, 523–528.
- Morishita, T., Maeda, J., Miyashita, S., Matsumoto, T. & Dick, H. J. B. (2004). Magmatic srilankite (Ti₂ZrO₆) in gabbroic vein cutting oceanic peridotites: An unusual product of peridotite–melt interactions beneath slow-spreading ridges. *American Mineralogist* **89**, 759–766.
- Morris, E. & Detrick, R. S. (1991). Three-dimensional analysis of gravity anomalies in the MARK area, Mid-Atlantic Ridge 23°N. *Journal of Geophysical Research* **96**, 4355–4366.
- Mukasa, S. B. & Shervais, J. W. (1999). Growth of subcontinental lithosphere: evidence from repeated dike injections in the Balmuccia lherzolite massif, Italian Alps. *Lithos* **48**, 287–316.
- Navon, O. & Stolper, E. (1987). Geochemical consequences of melt percolation: the upper mantle as a chromatographic column. *Journal of Geology* **95**, 285–307.
- Nicolas, A. (1986). Structure and petrology of peridotites: clues to their geodynamic environment. *Reviews of Geophysics* **24**, 875–895.
- Nicolas, A. (1989). *Structures of Ophiolites and Dynamics of Oceanic Lithosphere*. Dordrecht: Kluwer Academic.
- Nicolas, A. & Prinzhofer, A. (1983). Cumulative or residual origin for the transition zone in ophiolites: structural evidence. *Journal of Petrology* **24**, 188–206.
- Niida, K. (1997). Mineralogy of MARK peridotites: Replacement through magma channeling examined from Hole 920D, MARK area. In: Karson, J. A., Cannat, M., Miller, D. J. & Elthon, D. (eds) *Proceedings of the Ocean Drilling Program, Scientific Results, 153*. College Station, TX: Ocean Drilling Program, pp. 265–275.
- Niu, Y. & O'Hara, M. J. (2008). Global correlations of ocean ridge basalt chemistry with axial depth: a new perspective. *Journal of Petrology* **49**, 633–664.
- Niu, Y., Langmuir, C.H. & Kinzler, R. J. (1997). The origin of abyssal peridotites: A new perspective. *Earth and Planetary Science Letters* **152**, 251–265.
- Ohara, Y., Yoshida, T. & Kasuga, S. (2001). Giant megamullion in the Parece Vela Backarc basin. *Marine Geophysical Researches* **22**, 47–61.
- Okino, K., Matsuda, K., Christie, D. M., Nogi, Y. & Koizumi, K. (2004). Development of oceanic detachment and asymmetric spreading at the Australian–Antarctic Discordance. *Geochemistry, Geosystems* **5**, 22, doi:10.1029/2004GC000793.
- Piccardo, G. B., Zanetti, A., Poggi, E., Spagnolo, G. & Müntener, O. (2006). Melt/peridotite interaction in the Southern Lanzo peridotite: Field, textural and geochemical evidence. *Lithos* **94**, 181–209.
- Purdy, G. M. & Detrick, R. S. (1986). Crustal structure of the Mid-Atlantic Ridge at 23°N from seismic refraction studies. *Journal of Geophysical Research* **91**, 3739–3762.
- Python, M. & Ceuleneer, G. (2003). Nature and distribution of dykes and related melt migration structures in the mantle section of the Oman Ophiolite. *Geochemistry, Geophysics, Geosystems* **4**, doi:10.1029/2002GC000354.
- Quick, J. E. (1980). *Part I: Petrology and petrogenesis of the Trinity Peridotite, Northern California. Part II: Petrogenesis of Lunar Breccia 12013*. Pasadena, CA: California Institute of Technology.

- Quick, J. E. (1981a). Petrology and petrogenesis of the Trinity Peridotite, an upper mantle diapir in the Eastern Klamath Mountains, Northern California. *Journal of Geophysical Research* **86**, 11837–11863.
- Quick, J. E. (1981b). The origin and significance of large, tabular dunite bodies in the Trinity Peridotite, Northern California. *Contributions to Mineralogy and Petrology* **78**, 413–422.
- Rabinowicz, M., Ceuleneer, G. & Nicolas, A. (1987). Melt segregation and flow in mantle diapirs below spreading centers: evidence from the Oman Ophiolite. *Journal of Geophysical Research* **92**, 3475–3486.
- Rampone, E., Piccardo, G. B., Vannucci, R. & Bottazzi, P. (1997). Chemistry and origin of trapped melts in ophiolitic peridotites. *Geochimica et Cosmochimica Acta* **41**, 4557–4569.
- Reid, I. & Jackson, H. R. (1981). Oceanic spreading rate and crustal thickness. *Marine Geophysical Researches* **5**, 165–172.
- Reuber, I. (1988). Complexity of the crustal sequence in the northern Oman ophiolite (Fizh and southern Aswad blocks): The effect of early slicing? *Tectonophysics* **151**, 137–165.
- Reynolds, J. R. & Langmuir, C. H. (1997). Petrological systematics of the Mid-Atlantic Ridge south of Kane: Implications for ocean crust formation. *Journal of Geophysical Research* **102**, 14915–14946.
- Robinson, C. J., Bickle, M. J., Minshull, T. A., White, R. S. & Nichols, A. R. L. (2001). Low degree melting under the Southwest Indian Ridge: the roles of mantle temperature, conductive cooling and wet melting. *Earth and Planetary Science Letters* **188**, 383–398.
- Roeder, P. L. & Emslie, R. F. (1970). Olivine–liquid equilibrium. *Contributions to Mineralogy and Petrology* **29**, 277–302.
- Ross, K. & Elthon, D. (1997). Extreme incompatible trace-element depletion of diopside in residual mantle from south of the Kane Fracture Zone. In: Karson, J. A., Cannat, M., Miller, D. J. & Elthon, D. (eds) *Proceedings of the Ocean Drilling Program, Scientific Results, 153*. College Station, TX: Ocean Drilling Program, pp. 277–284.
- Schilling, J.-G., Zajac, M., Evans, R., Johnston, T., White, W., Devine, J. D. & Kingsley, R. (1983). Petrologic and geochemical variations along the Mid-Atlantic Ridge from 29°N to 73°N. *American Journal of Science* **283**, 510–586.
- Searle, R. C., Cannat, M., Fujioka, K., Mével, C., Fujimoto, H., Bralec, A. & Parsons, L. M. (2003). FUJI Dome: A large detachment fault near 64°E on the very-slow spreading southwest Indian Ridge. *Geochemistry, Geophysics, Geosystems* **4**, 25, doi:10.1029/2009GC002497.
- Seyler, M. & Bonatti, E. (1997). Regional-scale melt–rock interaction in lherzolitic mantle in the Romanche fracture zone (Atlantic Ocean). *Earth and Planetary Science Letters* **146**, 273–287.
- Seyler, M., Toplis, M. J., Lorand, J.-P., Luguét, A. & Cannat, M. (2001). Clinopyroxene microtextures reveal incompletely extracted melts in abyssal peridotites. *Geology* **29**, 155–158.
- Sigurdsson, H. & Schilling, J. G. (1976). Spinel in Mid-Atlantic Ridge basalts: Chemistry and occurrence. *29* 7–20.
- Standish, J. J., Dick, H. J. B., Michael, P. J., Melson, W. G. & O’Hearn, T. (2008). MORB generation beneath the ultraslow-spreading Southwest Indian Ridge (9°–25°E): Major element chemistry and the importance of process versus source. *Geochemistry, Geophysics, Geosystems* **9**, 39, doi:10.1029/2008GC001959.
- Stevens, R. E. (1944). Composition of some chromites of the western hemisphere. *American Mineralogist* **29**, 1–34.
- Suen, C. J., Frey, F. A. & Malpas, J. (1979). Bay of Islands ophiolite suite, Newfoundland: Petrologic and geochemical characteristics with emphasis on rare earth element geochemistry. *Earth and Planetary Science Letters* **45**, 337–348.
- Suhr, G. (1999). Melt migration under ocean ridges: Inferences from reactive transport modelling of upper mantle hosted dunites. *Journal of Petrology* **40**, 575–599.
- Suhr, G. & Batanova, V. (1998). Basal lherzolites in the Bay of Islands Ophiolite: Origin by detachment-related telescoping of a ridge-parallel melting gradient. *Terra Nova* **10**, 1–5.
- Suhr, G., Hellebrand, E., Johnson, K. & Brunelli, D. (2008). Stacked gabbro units and intervening mantle: A detailed look at a section of IODP Leg 305, Hole U1309D. *Geochemistry, Geophysics, Geosystems* **9**, 31, doi:10.1029/2008GC002012.
- Suzuki, T., Morishita, T. & Zanetti, A. (2009). Metasomatic silica-enrichment recorded in the Finero phlogopite peridotites. In: Montanini, A., Piccardo, G. B. & Tribuzio, R. (eds) *Alpine Ophiolites and Modern and Modern Analogues*. Parma: University of Parma, pp. 70–71.
- Takazawa, E., Okayasu, T. & Satoh, K. (2003). Geochemistry and origin of the basal lherzolites from the northern Oman ophiolite (northern Fizh block). *Geochemistry, Geophysics, Geosystems* **4**, 31, doi:10.1029/2001GC000232.
- Tartarotti, P., Cannat, M. & Mevel, C. (1995). Gabbroic dikelets in serpentinized peridotites from the Mid-Atlantic Ridge at 23°20’N. In: Vissers, R. L. M. & Nicolas, A. (eds) *Mantle and Lower Crust Exposed in Oceanic Ridges and in Ophiolites*. Dordrecht: Kluwer Academic, pp. 35–70.
- Tartarotti, P., Susini, S., Nimis, P. & Ottolini, L. (2002). Melt migration in the upper mantle along the Romanche Fracture Zone (Equatorial Atlantic). *Lithos* **63**, 125–149.
- Tucholke, B. E., Lin, J. & Kleinrock, M. C. (1998). Megamullions and mullion structure defining oceanic metamorphic core complexes on the Mid-Atlantic Ridge. *Journal of Geophysical Research* **103**, 9857–9866.
- Tucholke, B. E., Behn, M. D., Buck, R. & Lin, J. (2008). The role of melt supply in oceanic detachment faulting and formation of megamullions. *Geology* **36**, 455–458.
- Van Den Bleeken, G., Müntener, O. & Ulmer, P. (2010). Reaction process between tholeiitic melt and residual peridotite in the uppermost mantle: an experimental study. *Journal of Petrology*, (in press).
- Walker, D., Shibata, T. & DeLong, S. E. (1979). Abyssal tholeiites from the Oceanographer Fracture Zone. *Contributions to Mineralogy and Petrology* **70**, 111–125.
- Warren, J. M. & Hirth, G. (2006). Grain size sensitive deformation mechanisms in naturally deformed peridotites. *Earth and Planetary Science Letters* **248**, 438–450.
- White, R. S., McKenzie, D. & O’Nions, R. K. (1992). Oceanic crustal thickness from seismic measurements and rare earth element inversions. *Journal of Geophysical Research* **97**, 19683–19715.
- Whitehead, J. A., Jr, Dick, H. J. B., Schouten, & H., (1984). A mechanism for magmatic accretion under spreading centres. *Nature* **312**, 146–148.
- Williams, C. M. (2007). *Oceanic Lithosphere Magnetization: Marine Magnetic Investigations of Crustal Accretion and Tectonic Processes in Mid-Ocean Ridge Environments*, Cambridge, MA: Massachusetts Institute of Technology; Woods Hole, MA: Woods Hole Oceanographic Institution, 285 pp.
- Williams, C. M., Tivey, M. A. & Behn, M. D. (2006). The magnetic structure of Kane Megamullion: Results from marine magnetic anomalies, paleomagnetic data and thermal modeling. *EOS Transactions, American Geophysical Union, Fall Meeting Supplement* **87**, Abstract T24A-03.
- Workman, R. K. & Hart, S. R. (2004). Major and trace element composition of the depleted MORB mantle (DMM). *Earth and Planetary Science Letters* **231**, 53–72.